Università degli Studi di Padova

Department of Industrial Engineering
Master degree course in Electrical Engineering

DESIGN BY NUMERICAL METHODS OF A PATCH ANTENNA ARRAY FOR MICROWAVE HYPERTHERMIA

Supervisor:
Prof. Fabrizio Dughiero

Assistant Supervisor:
Eng. Fernando Bressan

Graduate Student:
Christian Bianchi

Session 2013/2014

Ai miei nonni
Nerina, Agostino,
Odilla, Ruggero

Contents

Ringraziamenti

Vorrei ringraziare il Professor Dughiero per avermi aiutato in questo lavoro di tesi, e per avermi dato la possibilità di lavorare in questo interessantissimo campo di ricerca. Ringrazio l'ingegner Bressan per avermi assistito con il suo prezioso aiuto nello sviluppo dei modelli numerici e per tutti i consigli dati. Grazie a tutti i ragazzi del LEP, tesisti, dottorandi e ricercatori, per la piacevole compagnia in laboratorio e davanti a innumerevoli caffé. Al Professor Di Barba un sentito ringraziamento per avermi fatto conoscere un argomento di ricerca estremamente affascinante. Grazie alla cara amica Nancy per avermi aiutato con l'inglese e a Luca per i suoi consigli di impaginazione.

Voglio inoltre ringraziare Chiara per essermi stata sempre vicina in tutti questi anni e per avermi dato sempre ispirazione ed ottimismo per il futuro. Un calorosissimo ringraziamento alla famiglia Raveri (allargata!) per avermi fatto sentire come un figlio e fratello, oltreché amico. Un grazie speciale a mia mamma e mio papà per aver reso possibile il raggiungimento di questo traguardo, ed inoltre, un forte abbraccio a Erika, Lele, e al piccolo Thomas. Infine, voglio ringraziare di cuore tutti quegli amici dell'infanzia, degli anni del liceo, e degli anni universitari che continuano tuttora ad esser compagni di mille avventure.

Padova, 4 Aprile 2014

Sommario

In questa tesi è stato analizzato il comportamento elettromagnetico di una schiera di antenna patch per un'applicazione di ipertemia alle microonde. L'ipertermia è una tecnica clinica che permette di ridurre masse tumorali tramite un innalzamento localizzato della temperatura nei tessuti malati. La propagazione di campi elettromagnetici ad alta frequenza (banda delle microonde) all'interno di tessuti organici induce, per polarizzazione dielettrica, delle sorgenti di calore. Innalzando la temperatura oltre i 43°C viene indotto il fenomeno dell'apoptosi, ovvero la morte spontanea delle cellule. In questa tesi è stata studiata una schiera, costituita da due elementi radianti, tramite modelli numerici agli elementi finiti (COMSOL Multiphysics) e alle differenze finite (Matlab). Il Capitolo 1 è un'introduzione generale del modello fisico tramite una trattazione analitica dei principali fenomeni coinvolti. Sono state descritte le equazioni di Maxwell, e da queste sono state ricavate le espressioni tipiche della propagazione ondulatoria; inoltre, sono state trattati gli aspetti termici del sistema organico tramite l'equazione di Pennes. Il modello fornito da Pennes permette di studiare lo scambio termico che avviene all'interno di tessuti umani, tenendo conto degli effetti dei capillari sanguigni. Nel Capitolo 2 sono state considerati gli aspetti modellistici agli elementi finiti, definendo i materiali utilizzati (ricavati dalla letteratura scientifica), la geometria impostata, il dominio di calcolo (compresa l'ottimizzazione ed il bilanciamento tra precisione e tempo computazionale), le impostazioni della fisica, ed infine l'algoritmo risolutore. Sono stati indicati i principali parametri di interesse clinico, ed illustrati alcuni esempi di visualizzazione dei risultati. Nel Capitolo 3 abbiamo impostato lo sviluppo del dispositivo radiante tramite simulazioni numeriche, grazie alle quali si è ricavato il valore delle principali dimensioni progettuali della patch antenna. Il dispositivo è stato progettato affinchè sia in risonanza alla frequenza di 2.45 GHz, e che verifichi la condizione di adattamento alla linea di alimentazione, caratterizzata da un impedenza di 50Ω. Dopo la definizione del dimensionamento abbiamo studiato analiticamente il comportamento della schiera e valutato l'impatto che i principali parametri elettrici e geometrici possono avere sul diagramma di

radiazione. Abbiamo valutato l'importanza dell'ampiezza del lobo principale e la sua dipendenza dal numero degli elementi N della schiera. Inoltre, di particolare interesse è la dimensione elettromagnetica d/λ per quanto riguarda la variazione del lobo. Nel Capitolo 4 è stato sviluppato un modello 1D, tempo-variante alle differenze finite per poter valutare la risposta termica del sistema. Tre principali casi sono stati tenuti in considerazione: 1) modello a potenza costante per l'intero trattamento, 2) modello a potenza variabile in due livelli (studio della riduzione dei transitori termici), 3) modello a potenza pulsata con più livelli di regolazione. Nel Capitolo 5 abbiamo presentato alcune analisi parametriche alla condizione di regime termico per individuare una configurazione ottimale del dispositvo durante la terapia. I parametri principali dell'analisi sono la distanza tra il paziente e le antenne d, la distanza tra le antenne p, lo sfasamento tra le alimentazioni $\Delta\phi$, e la potenza di alimentazione di ciascuna antenna P. Definiti questi parametri abbiamo osservato il tempo necesssario per raggiungere il regime stazionario, e data l'eccessiva durata del periodo è stata effettuata un'ulteriore analisi parametrica per individuare l'ottimale potenza solo per i primi 60 secondi. Definita quest'ultima, abbiamo comparato l'evoluzione delle temperature all'interno della massa tumorale tra il caso con potenza di alimentazione a due livelli, ed il caso con la potenza ad un livello solo. Infine, sono state riassunte le principali caratteristiche del dispositvo per ottenere un riscaldamento il più possibile confinato nella regione soggetta al trattamento.

List of Symbols

$\mathbf{H}$	magnetic field $[A/m]$
$\mathbf{E}$	electric field $[V/m]$
$\mathbf{B}$	magnetic flux density $[Wb/m^2]$
$\mathbf{D}$	electric flux density $[C/m^2]$
$\mathbf{J}$	electric current density $[A/m^2]$
$\mathbf{A}$	magnetic vector potential $[Wb/m]$
V	electric scalar potential $[V]$
σ	electrical conductivity $[H/m]$
μ	magnetic permeability $[H/m]$
ϵ	dielectric permittivity $[F/m]$
$\dot{\epsilon}$	complex dielectric permittivity $[F/m]$
ρ	electric charge density $[C]$
μ	magnetic permeability $[H/m]$
$\mathbf{P}$	Poynting vector $[W/m^2]$
λ	wavelength $[m]$
ω	angular frequency $[rd/s]$
f	frequency $[Hz]$
$\dot{\lambda}$	wave propagation constant $[1/m]$
α	wave attenuation constant $[1/m]$
β	wave phase constant $[1/m]$
ρ_r	reflection coefficient $[1]$
η	radiation efficiency $[\%]$
SAR	Specific Absorption Rate $[W/kg]$
δ_m	mass density $[kg/m^3]$
c	specific heat capacity $[J/(kgK)]$
k	thermal conductivity $[W/(mK)]$
h	convective heat exchange coefficient $[W/(m^2K)]$
q_m	metabolism heat $[W/m^3]$
ω_b	blood perfusion rate $[1/s]$
T	Temperature $[K]$
MES	Mesh Element Size $[m]$

Z_c characteristic impedance $[\Omega]$
P feeding power $[W]$
ϕ feeder phase $[rd]$
$\vec{M}$ equivalent array moment $[Am]$
$\vec{F}$ array factor [1]
t time $[s]$

Chapter 1

Introduction to Hyperthermia

The purpose of this thesis is the development and the analysis of a prototype of a phased array antenna which can be applied for Hyperthermia Cancer Treatment. Hyperthermia is a novel therapy that induces the apoptosis of tumor cells ("spontaneous"death of cells that differs from necrosis for absence of inflammation) by heating localized organic mass regions in an appropriate range of temperature. The most used technique to heat the damaged tissues utilizes electromagnetic fields in the microwave range or radiofrequency range.

1.1 General Overview

Hyperthermia can be applied as an only treatment or in addition to traditional chemo-therapy and radio-therapy. In scientific literature there is evidence that shows the effectiveness of HCT as a stand-alone treatment modality, as well for combined therapy [8]. There are four types of HCT: 1) whole-body modality (which is provided with temperature up to 41.8° for safety reason) 2) regional modality 3) superficial modality 4) intra-cavity or intraluminal modality (large temperature range is available).

If heat is transfered to a tumor cell, the DNA reparation process is dramatically compromised by thermal-shock, and also the capability of the cell to receive chemo-drugs is improved due to an internal tumor pressure reduction. Among different methods providing heating of tissues, the EM heating is widely used. The electromagnetic energy propagates throughout the body, and it is converted into thermal energy by a phenomenon similar to friction at molecular level. An interesting characteristic of this treatment is the good selectivity during the heating process, therefore the overheating of healthy tissues is limited. The selectivity can be obtained by taking advantage of the

difference of the physical parameters between tumors and healthy tissues. If we want to assess the biological effects that are induced by heating the tumor we can adopt $CEM43°$ units. $CEM43°$ means Cumulative Equivalent Minutes, and it represents the period that would be required, if we would heat the tumor at 43°, to obtain the same biological damage of the observed treatment. This method is based upon the observation that the rate of cell killing, which arises by a factor 4 when the temperature is increased by one celsius degree, only doubles when the temperature is over 43° [8].

During the treatment, a water-bolus can be used both to reduce the reflected power from the device and to reduce superficial hot-spots at skin level. Therefore, an important issue is the optimal design of the geometry (distance between patient and applicator) and the appropriate temperature of the cooling water (regulation of convection heat exchange). A fundamental issue is related to thermometric measurements. It's possible to use an infrared camera and sensors for superficial measures, but not for internal evaluations. Since we want to measure the temperature inside the body, to get feedbacks related to the tumor temperature, we need to use a catheter which unfortunately can be very invasive and painful for the patient. An other interesting method is the MRI technique, but it is not always electromagnetic compatible with the applicator. Also, MRI requires very expensive devices which define obstacles for developments in the future.

HCT can be applied both for shallow as well as for deep tumors, so the generated electromagnetic waves are selected considering their penetration depth, therefore considering their frequency. In this thesis, the behavior of a 2.45 GHz microwave phased array antenna is studied. The array is formed by microstrip patch elements and it controlled by a current phase shifter (steerer). This operating frequency is suitable for superficial tumors like skin lesions, melanoma, or shallow breast cancer.

The device can operates only in a appropriate band defined by ITU (International Telecommunication Union). This band is called ISM (Industrial, Scientific and Medical) and it covers only a small part of electromagnetic spectrum. This band is developed for not-commercial applications, but only for industry, scientific or medical purposes. A device can work in this band but with a few limitations regarding the place (only indoor use: like a laboratory for research or industrial applications) where the device irradiates the electromagnetic fields. This limitation is necessary to avoid interference between telecommunication systems and other electromagnetic field sources, and also for safety reason for operators. The ISM band is formed by the following portions of frequency spectrum by international regulation:

- 900 MHz band (902-928 MHz)

- 2.4 GHz band (2.4-2.4835 GHz)
- 5.8 GHz band (5.725-5.875 GHz)

The first comprehensive document to summarize all available techniques and measurement data that are required for HCT validation is the task force report of the European Society for Hyperthermic Oncology (ESHO) and the Committee for Concerted Action in Biomedical Engineering (COMAC-BME). These Institutions have drawn the guidelines for the development of the Hyperthermia Treatment.

Since the treated part of human body has to be posed in the near field region of the electromagnetic field, a numerical simulation is needed to obtain reliable results of the electric field magnitude and temperature distribution. The model implemented with an appropriate software help us during the design phase for the development of the device, and also, to implement the treatment planning which consists in the optimization of the temperature distribution. The model is actually defined by the coupling between an electromagnetic high frequency problem, that is solved by Maxwell equations (full Maxwell waves), and a thermal problem, that is solved by Pennes equation (bioheat exchange).

Hyperthermia is an innovative therapy that involves many disciplines from different scientific sectors, and therefore a strong collaboration between many scientists is required to obtain outstanding results. The main disciplines involved are the following:

- Radiofrquency and Microwave Engineering to develop the applicator, the feeding circuit, and the control devices.
- Thermal Engineering to analyze the temperature of the body from measures and phisical models.
- Numerical and Software Engineering to develop the algorithms and the simulation tools.
- Medicine to drive the entire therapy, and to assess the most effective technique, from a biological standpoint.

In a few hospitals around the world, HCT is already adopted in an experimental way, but the research in this field has to strive toward better controlled treatments, more reliable results, and painless therapies for the patients.

1.2 Electromagnetic Model

The physical model is implemented using COMSOL Multiphysics that is a software based on the Finite Element Method. This simulation software offers an interface to MATLAB that allow us to apply an optimization algorithm to achieve the required temperature distribution. The analysis can be divided in several steps:

- Segmentation of the model of human body by Magnetic Resonance Imaging.
- Electromagnetic simulation and irradiation pattern by solving the full Maxwell equations.
- Heat transfer simulation and temperature distribution by the Fourier law and the Pennes equation.
- Optimization of the thermal pattern by changing the phases of the feeding currents.

In the thesis, excepted for the the MRI step, each issue will be treated both with theoretical and numerical approach.

1.2.1 Microwave Propagation

In classical physics, electromagnetic phenomena are described by a system of four partial differential equations, synthesized by James Clerk Maxwell. Maxwell unifies the Ampere law (1.1), the Faraday-Lenz law (1.2) and the Gauss laws of electric (1.3) and magnetic fields (1.4). These equations are topological relations that impose the geometry of the fields and their evolution over time. Therefore, starting from the following relations, we can obtain a general expression of the radiated fields[1]:

$$\nabla \times \mathbf{H} = \mathbf{J} + \frac{\partial \mathbf{D}}{\partial t} \tag{1.1}$$

$$\nabla \times \mathbf{E} = -\frac{\partial \mathbf{B}}{\partial t} \tag{1.2}$$

$$\nabla \cdot \mathbf{D} = \rho \tag{1.3}$$

[1] In general the fields are dependent on space and time, but to simplify the notation, the term ($\mathbf{r}$,t) is not explicit.

$$\nabla \cdot \mathbf{B} = 0 \tag{1.4}$$

In these equations, $\mathbf{E}$ is the electric field $[Vm^{-}1]$, $\mathbf{D}$ is the electric flux density $[Cm^{-}2]$, $\mathbf{B}$ is the magnetic flux density $[Wbm^{-}2]$, $\mathbf{H}$ is the magnetic field $[Am^{-}1]$, ρ is the electric charge density $[Cm^{-}3]$ and $\mathbf{J}$ is the electric current density $[Am^{-}2]$. We need other equations that link the "forcing" fields to the "induced" fields into the materials. The equations are given by the constitutive relations:

$$\mathbf{D} = \epsilon \, \mathbf{E} \tag{1.5}$$

$$\mathbf{B} = \mu \, \mathbf{H} \tag{1.6}$$

$$\mathbf{J} = \sigma \, \mathbf{E} \tag{1.7}$$

$$\nabla \cdot \mathbf{J} = -\frac{\partial \rho}{\partial t} \tag{1.8}$$

where ϵ is the dielectric permittivity $[Fm^{-}1]$ and μ is the magnetic permeability $[Hm^{-}1]$. Let us assume that the *material properties are homogeneous and isotropic* (this assumption is valid only to obtain a general expression of propagation, but we will have to make into account the inhomogeneity for the propagation into the tissues). Since the magnetic induction has the property (1.4), we can write

$$\mathbf{B} = \nabla \times \mathbf{A} \tag{1.9}$$

where $\mathbf{A}$ is called *magnetic vector potential*. If we insert (1.9) in (1.2) we obtain:

$$\nabla \times \mathbf{E} = -\frac{\partial (\nabla \times \mathbf{A})}{\partial t} \tag{1.10}$$

$$\nabla \times \mathbf{E} = \nabla \times \left(-\frac{\partial \, \mathbf{A}}{\partial t} \right) \tag{1.11}$$

$$\left(\nabla \times \mathbf{E} + \frac{\partial \, \mathbf{A}}{\partial t} \right) = 0 \tag{1.12}$$

if we consider a generic scalar function f, the following relation holds

$$\nabla \times \nabla \, f = 0 \tag{1.13}$$

therefore (1.12) has the same structure of (1.13). We can find a scalar function V that is called *scalar electric potential*:

$$\mathbf{E} = -\frac{\partial \mathbf{A}}{\partial t} - \nabla \mathrm{V} \tag{1.14}$$

We can use the expression (1.14) into (1.3) to obtain

$$\nabla^2 \mathrm{V} + \frac{\partial (\nabla \cdot \mathbf{A})}{\partial t} = -\frac{\rho}{\epsilon} \tag{1.15}$$

This is a relation between the magnetic vector potential and the scalar electric potential. Now let's consider (1.9), (1.1) and the following mathematical identity for a generic vector function $\mathbf{G}$:

$$\nabla \times \nabla \times \mathbf{G} = \nabla \nabla \cdot \mathbf{G} - \nabla^2 \mathbf{G} \tag{1.16}$$

and we obtain

$$\nabla \nabla \cdot \mathbf{A} - \nabla^2 \mathbf{A} = \mu \mathbf{J} + \mu\epsilon \frac{\partial \mathbf{E}}{\partial t} \tag{1.17}$$

$$\mu \mathbf{J} - \mu\epsilon \frac{\partial^2 \mathbf{A}}{\partial t^2} - \mu\epsilon \frac{\partial \nabla \mathrm{V}}{\partial t} = \nabla (\nabla \cdot \mathbf{A}) - \nabla^2 \mathbf{A} \tag{1.18}$$

Equations (1.15) and (1.18) allow us to obtain a complete description of the electromagnetic model using the potentials $\mathbf{A}$ and V. So far we have not defined uniquely $\mathbf{A}$ because we haven not set its divergence. A possible choice is the Lorentz condition (the most used condition for not stationary problem):

$$\nabla \cdot \mathbf{A} = -\mu\epsilon \frac{\partial \mathrm{V}}{\partial t} \tag{1.19}$$

Assuming (1.19) we can separate the unknown potentials between (1.15) and (1.18)

$$\nabla^2 \mathrm{V} - \mu\epsilon \frac{\partial^2 \mathrm{V}}{\partial t^2} = -\frac{\rho}{\epsilon} \tag{1.20}$$

$$\nabla^2 \mathbf{A} - \mu\epsilon \frac{\partial^2 \mathbf{A}}{\partial t^2} = -\mu \mathbf{J} \tag{1.21}$$

therefore we can derive all the fields only solving one of the two last differential equations. Their solutions are as follows [3]

$$\mathrm{V} = \int_{\tau} \frac{\rho(\mathbf{p}, t - \frac{d_{rp}}{v})}{4\pi\epsilon d_{rp}} d\tau \tag{1.22}$$

$$\mathbf{A} = \int_{\gamma} \frac{\mu J(\mathbf{p}, t - \frac{d_{rp}}{v})}{4\pi d_{rp}} d\gamma \tag{1.23}$$

where τ is the region which contains free charge, and γ is the region which contains current density. When we know the distribution of the current density we can calculate $\mathbf{A}$, and V using the Gauge condition. Also, using (1.9) and (1.14) we can derive the magnetic and the electric fields all over the propagation domain. The term $\frac{d_{rp}}{v}$ appears in (1.22) and (1.23), and it represents the delay of the fields with respect to the observation point. In fact, since the velocity of propagation v (speed of light) is finite, we have that the greater is the distance from the source and the bigger is the delay. For this reason $\mathbf{A}$, and V are called *retarded potentials*. Therefore, it's possible to determine $\mathbf{A}$, $\mathbf{B}$ and $\mathbf{E}$, if the current density $\mathbf{J}$ is known, using (1.23). This problem can be solved analytically just for a few cases, which require high-symmetrical geometry and harmonic feeding. Otherwise, for all the remaining cases, we can derive a solution only by using numerical techniques that are implemented in appropriate softwares.

1.2.2 Conservation of Electromagnetic Power

Let us consider a finite volumetric region V which is passed through by a flow of electromagnetic energy. If the region is conductive, then, part of the energy is dissipated inside V, while an other part can be accumulated as magnetic or dielectric energy. Starting from Maxwell equations, we can find a relation that is the balance between different forms of power. From (1.1), (1.7), (1.5) we can obtain [2]:

$$\nabla \times \mathbf{H} = \sigma\mathbf{E} + \epsilon\frac{\partial \mathbf{E}}{\partial t} \tag{1.24}$$

while combining (1.2) and (1.6)

$$\nabla \times \mathbf{E} = -\mu\frac{\partial \mathbf{H}}{\partial t} \tag{1.25}$$

[2] from here on the $\mathbf{r}$ and t dependence is not explicit.

if we apply the dot product of $\mathbf{E}$ into the curl of $\mathbf{H}$, and also the dot product of $\mathbf{H}$ into the curl of $\mathbf{E}$, we derive

$$\mathbf{E} \cdot (\nabla \times \mathbf{H}) = \mathbf{E} \cdot \mathbf{J} + \mathbf{E} \cdot \epsilon \frac{\partial \mathbf{E}}{\partial t} = \mathbf{J} \cdot \mathbf{E} + \frac{1}{2}\epsilon \frac{\partial E^2}{\partial t} \tag{1.26}$$

$$\mathbf{H} \cdot (\nabla \times \mathbf{E}) = -\mathbf{H} \cdot \mu \frac{\partial \mathbf{H}}{\partial t} = -\frac{1}{2}\mu \frac{\partial H^2}{\partial t} \tag{1.27}$$

now we can subtract (1.27) to (1.26), that yields

$$\mathbf{E} \cdot (\nabla \times \mathbf{H}) - \mathbf{H} \cdot (\nabla \times \mathbf{E}) = \mathbf{J} \cdot \mathbf{E} + \frac{1}{2}\epsilon \frac{\partial E^2}{\partial t} + \frac{1}{2}\mu \frac{\partial H^2}{\partial t} \tag{1.28}$$

now we have to consider the following mathematical identity

$$\nabla \cdot (\mathbf{Y} \times \mathbf{W}) = \mathbf{W} \cdot (\nabla \times \mathbf{Y}) - \mathbf{Y} \cdot (\nabla \times \mathbf{W}) \tag{1.29}$$

so we can obtain

$$\nabla \cdot (\mathbf{E} \times \mathbf{H}) = -\mathbf{J} \cdot \mathbf{E} - \frac{1}{2}\epsilon \frac{\partial E^2}{\partial t} - \frac{1}{2}\mu \frac{\partial H^2}{\partial t} \tag{1.30}$$

integrating over the volume V, and applying the Gauss theorem :

$$\int_V \nabla \cdot (\mathbf{E} \times \mathbf{H}) dV = \oint_S (\mathbf{E} \times \mathbf{H}) \cdot \hat{n} dS \tag{1.31}$$

where $S = \partial V$ is the surface boundary of the domain V. The term $\mathbf{P} = \mathbf{E} \times \mathbf{H}$ is the *Poynting vector* that represents the electromagnetic power per surface $[Wm^{-}2]$, and it propagates along the direction that is orthogonal to $\mathbf{E}$ and $\mathbf{H}$. This power flows through the boundary S from the volume V toward the external space [4].

$$\oint_S \mathbf{P} \cdot \hat{n} dS = -\int_V \mathbf{J} \cdot \mathbf{E} dV - \int_V \frac{1}{2}\epsilon \frac{\partial E^2}{\partial t} dV - \int_V \frac{1}{2}\mu \frac{\partial H^2}{\partial t} dV \tag{1.32}$$

The last equation is the balance between different kinds of electromagnetic energy. The right-hand side of (1.32) is formed by three terms which represent the power dissipated by the joule effect, the accumulated electric energy and the accumulated magnetic energy.

1.2.3 Frequency Domain

If all the quantities vary over time in sinusoidal steady state, we can apply the phasorial representation to simplify all the calculations.

$$\sqrt{2}A\sin(\omega t+\alpha)\rightarrow Ae^{j\omega t+\alpha}=Ae^{j\omega t}Ae^{j\alpha}\rightarrow Ae^{j\alpha} \tag{1.33}$$

and neglecting the rotation factor. If we consider the property of the exponentials we can substitute also

$$\frac{\partial A}{\partial t}=j\omega\dot{A} \tag{1.34}$$

Since the transformation is related to a derivation over time, while the divergence and the curl operate over space, the differential operators do not change in the frequency domain. Using the last equivalences we can transform the Maxwell equations in the following way:

$$\nabla\times\dot{\mathbf{H}}=\dot{\mathbf{J}}+j\omega\dot{\mathbf{D}} \tag{1.35}$$

$$\nabla\times\dot{\mathbf{E}}=-j\omega\dot{\mathbf{B}} \tag{1.36}$$

$$\nabla\cdot\dot{\mathbf{D}}=\dot{\rho} \tag{1.37}$$

$$\nabla\cdot\dot{\mathbf{B}}=0 \tag{1.38}$$

$$\nabla\cdot\dot{\mathbf{J}}=-j\omega\dot{\rho} \tag{1.39}$$

It has to be noted that the fields $\mathbf{E},\mathbf{D},\mathbf{H},\mathbf{B},\mathbf{J}$ are complex vectors that do not depend on the time variable but only on the space variable.

1.2.4 Propagation in Dissipative Media

We can obtain a simple expression for the propagation of electromagnetic fields inside a dissipative medium. The analysis is done with the assumption that the material is linear, homogeneous and isotropic. Let us consider (1.36) and (1.35), and if we apply the curl to the first one and we substitute it in (1.35), and applying (1.16) we derive:

$$\nabla^2\mathbf{E}=-\nabla\times\nabla\times\mathbf{E}=-\omega^2\mu\epsilon\mathbf{E}+j\omega\mu\sigma\mathbf{E} \tag{1.40}$$

and putting together some terms we obtain the Helmotz equation:

$$\nabla^2\mathbf{E} + \omega^2\mu\epsilon\left[1 - j\frac{\sigma}{\omega\epsilon}\right] = 0 \tag{1.41}$$

We can define the new quantity "complex permittivity" that contains the dissipation of the medium.

$$\dot{\epsilon} = \epsilon\left(1 - j\frac{\sigma}{\omega\epsilon}\right) = \epsilon' - j\epsilon'' \tag{1.42}$$

The imaginary part is related to the power losses. Also, we introduce the parameter $tan\delta$ that is characteristic for each material:

$$tan\delta = \frac{\epsilon''}{\epsilon'} \tag{1.43}$$

The solution of (1.41) can be obtained easily if we assume that the field is radiating as a plane wave (xy plane) along a certain direction of propagation (z axis) [3].

$$\frac{d^2E}{dz^2} - s^2E = 0 \tag{1.44}$$

where s is defined as follows:

$$s^2 = -\omega^2\mu\epsilon + j\omega\mu\sigma = \dot{\gamma}^2 \tag{1.45}$$

$$s_{12} = \pm\dot{\gamma} \tag{1.46}$$

$$\dot{\gamma} = \alpha + j\beta = \sqrt{-\omega^2\mu\epsilon + j\omega\mu\sigma} \tag{1.47}$$

where γ is the propagation constant, α is the attenuation costant, and β is the phase constant. If we want to define these constants by the material properties, we have to separate the imaginary part from the real one, then we derive as follows

$$\alpha = \omega\sqrt{\mu\epsilon}\sqrt{\frac{1}{2}\left(\sqrt{1 + \left(\frac{\sigma}{\omega\epsilon}\right)^2} - 1\right)} \tag{1.48}$$

$$\beta = \omega\sqrt{\mu\epsilon}\sqrt{\frac{1}{2}\left(\sqrt{1 + \left(\frac{\sigma}{\omega\epsilon}\right)^2} + 1\right)} \tag{1.49}$$

[3] the subscript related to component of the field is neglected $E_x, E_y \to E$.

The solution of (1.41) can be written as the sum of two terms, the forward traveling wave and the backward traveling wave. All these considerations can be done also for the magnetic field, and therefore even H can be described in the same way of (1.51). Since we have assumed that the fields propagate as plane waves we can introduce the intrinsic impedance of the medium $\dot{\eta}$ as the ratio between the norm of $\mathbf{E}$ and $\mathbf{H}$.

$$\dot{\eta} = \sqrt{\frac{\mu}{\dot{\epsilon}}} \tag{1.50}$$

$$\mathbf{E}(z) = \mathbf{E}^{+}(z)e^{-\alpha z}e^{-j\beta z} + \mathbf{E}^{-}(z)e^{-\alpha z}e^{-j\beta z} \tag{1.51}$$

and making into account that E and H are perpendicular in plane propagation:

$$\mathbf{H}(z) = \frac{1}{\eta}\left[\hat{z} \times \left(\mathbf{E}^{+} - \mathbf{E}^{-}\right)\right] \tag{1.52}$$

$$\mathbf{H}(z) = \mathbf{H}^{+}(z)e^{-\alpha z}e^{-j\beta z} + \mathbf{H}^{-}(z)e^{-\alpha z}e^{-j\beta z} \tag{1.53}$$

and therefore both the electric and magnetic fields propagate inside the dissipative material as a sum of exponential functions. The forward wave is generated exclusively by the source, while the backward wave is due to the reflection of the dissipative load. In Figure 1.1 the travelling waves have been depicted.

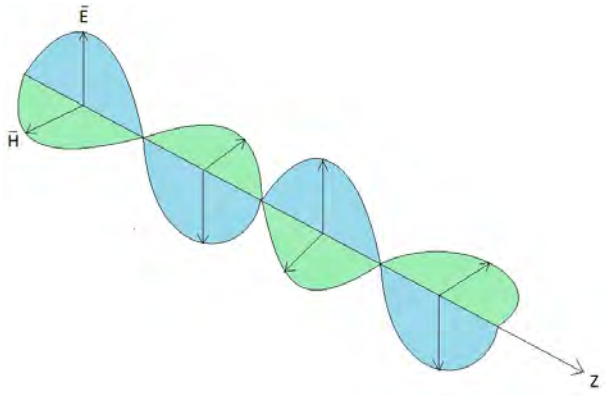

Figure 1.1: Example of a linearly polarized electromagnetic travelling wave.

1.2.5 Reflection and Absorption

When traveling electromagnetic waves enter into new materials, or when the fields are confined by a guide that changes its shape, a fraction of the electromagnetic power comes back as reflected power. In this case the transmission of energy can be limited, or even worse, completely compromised. During a transmission process, it is important to know the amount of power that cannot be transmitted to the load. We can introduce a parameter that represents the ratio between the norm of the incident field and the reflected field:

$$\rho_r = \frac{E^-}{E^+} = \frac{H^-}{H^+} = \sqrt{\frac{P^-}{P^+}} \tag{1.54}$$

This parameter is called "reflection coefficient" and its value is in the range between 0 (total transmission) and 1 (total reflection). The reflection is a common phenomenon that occurs at the interface between different transmission lines or when the geometry of the field changes dramatically. If we design a device that has some electromagnetic ports, we have to know the reflection at each port to be sure that the device operates effectively. In the case of antennas, the connection between the feeding line and the radiant component represents the port. The device operates correctly when the antenna is working at the resonance condition. Another important parameter to assess the absorption of the radiated power by the matter, is SAR (Specific Absorption Rate).

$$SAR = \int_V \frac{\sigma |\mathbf{E}|^2}{\delta_m} dv \tag{1.55}$$

where δ_m is the mass density of absorbing matter $[kg^-1]$. This value is the rate of power per unit of mass $[W/kg]$. Using these two last parameters we can evaluate the performances of the device because we can know both the power transmitted and the power that is actually absorbed.

1.3 Thermal Model

From a thermodynamic standpoint, the human body can be considered as a sophisticated self-regulated heat-exchange machine. The body is able to change its thermal state whenever external conditions are having an effect on it. The thermal-regulation acts through the metabolism and the blood circulation. These phenomena allow the human body to produce heat by chemical energy, and to propagate it all over the body. Also, the sweat production induces a more efficient heat-dispersal toward the environment.

1.3.1 Pennes Equations

The most used model of heat exchange between organic tissues is described by the Pennes equation (1.56), which is a second order partial differential equation with the temperature T as unknown function. Let's assume that the heat exchange occurs between an organic mass defined by a volume V and its confining tissues, then we can consider the heat transfer equation as follows [11]:

$$\rho c \frac{\partial T}{\partial t} = \nabla \cdot (k \nabla T) + q_m + \omega \rho_b c_b (T_a - T) \tag{1.56}$$

where ρ is the density of the tissue $[kgm^{-3}]$, c is the specific heat capacity of the tissue $[Jkg^{-1}K^{-1}]$, k is the thermal conductivity of the tissue $[Wm^{-1}K^{-1}]$, q_m is the heat produced by the metabolism $[W/m^3]$, ω_b is the blood perfusion rate $[1/s]$, ρ_b is the density of blood $[kgm^{-3}]$, c_b is the specific heat capacity of blood $[Jkg^{-1}K^{-1}]$, and T_a $[K]$ is the arterial blood temperature.

The equation (1.56) includes the heat conduction term, that usually is expressed by the Fourier Law. The new terms that appear represent the metabolism and the effect of blood that tends to maintain the temperature of the tissue at the same temperature of the arterial blood. The exchange occurs through the spread into the capillaries. The behavior of blood is actually similar to a convective mass that takes out heat from the confined tissue. This model has a few limitations, e.g. the direction of the blood flow is not considered, as well as the diameter of the artery, but anyway the model is in accordance with many experimental data. Also, this model is appropriate to be implemented by simulation softwares for its simplicity and for the limited number of physical parameters required.

1.3.2 Analytical 1D Model in Steady State

If we describe analytically a simple model governed by (1.56), and we implement it into Matlab, we can evaluate the influence of the parameters on the temperature. We consider a tissue made by two homogeneous layers (muscle and fat), and it has the temperature impressed on one side as boundary condition (tumor heated at the desired temperature) and a convective heat exchange on the other side (air or water flow on the skin). The representation of the model has been reported in Figure 1.2. Let's assume that the model is mono dimensional and that is in stationary steady state. Then we can write

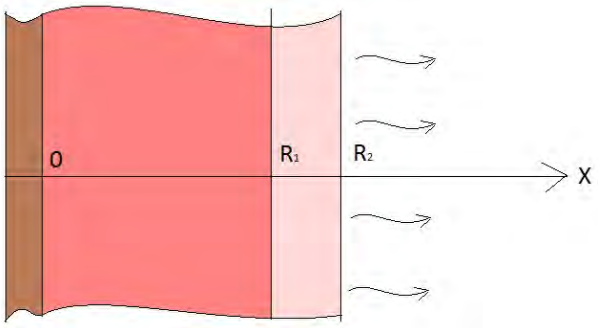

Figure 1.2: Two layers model of organic tissues in steady state regime.

the Pennes equation as follows:

$$\frac{dT^2}{dx^2} + \frac{\dot{q_m} + \omega\rho_b c_b(T_a - T)}{k} = 0 \tag{1.57}$$

The mathematical solution of (1.57) can be easily computed by substitution of variables:

$$m^2 = \frac{\omega\rho_b c_b}{k} \tag{1.58}$$

$$\theta = T - \left(T_a + \frac{\dot{q_m}}{\omega_b\rho_b c_b}\right) \tag{1.59}$$

$$\frac{d^2\theta}{dx^2} - m^2\theta = 0 \tag{1.60}$$

then we can calculate the characteristic polynomial and we derive its roots. We obtain:

$$\theta(x) = C_1 e^{mx} + C_2 e^{-mx} \tag{1.61}$$

since we have two layers, we derive a piece-wise expression for θ:

$$\begin{cases} \theta_1(x) = Ae^{m_1 x} + Be^{-m_1 x} & 0 \leq x < R_1 \\ \theta_2(x) = Ce^{m_2 x} + De^{-m_2 x} & R_1 \leq x < R_2 \end{cases} \tag{1.62}$$

$$m_1^2 = \frac{\omega_1\rho_b c_b}{k_1} \qquad m_2^2 = \frac{\omega\rho_b c_b}{k_2} \tag{1.63}$$

let us impose the boundary conditions: The temperature of the tumor is imposed by external heating at T_{tum}

$$T(0) = T_{tum} \tag{1.64}$$

At the interface between the muscle layer and the fat layer we impose the continuity of the temperature

$$T_1(R_1) = T_2(R_1) \tag{1.65}$$

and at the same time we have to impose the continuity of the first order derivative

$$\frac{dT_1}{dx}(R_1) = \frac{dT_2}{dx}(R_1) \tag{1.66}$$

also, we can impose the convection condition using the Newton law

$$h\left(T(R_2) - T_\infty\right) = -k_2 \frac{dT}{dx}(R_2) \tag{1.67}$$

Now we can use (1.59) to get explicit the equations above with regard to θ

$$\begin{aligned}
&A + B = T_{tum} - \left(T_a + \frac{\dot{q_{m1}}}{\omega_1 \rho_b c_b}\right) \qquad (1.68)\\
&Ae^{m_1 R_1} + Be^{-m_1 R_1} - Ce^{m_2 R_1} - De^{-m_2 R_1} = \frac{1}{\rho_b c_b}\left(\frac{\dot{q_{m2}}}{\omega_2} - \frac{\dot{q_{m2}}}{\omega_1}\right)\\
&Am_1 e^{m_1 R_1} - Bm_1 e^{-m_1 R_1} - Cm_2 e^{m_2 R_1} + Dm_2 e^{-m_2 R_1} = 0\\
&C\left[e^{m_2 R_2}\left(h + k_2 m_2\right)\right] + D\left[e^{-m_2 R_2}\left(h - k_2 m_2\right)\right] = h\left[T_\infty - \left(T_a + \frac{\dot{q_{m1}}}{\omega_1 \rho_b c_b}\right)\right]
\end{aligned}$$

The equations above allow us to derive the coefficients A, B, C, D, and to manage better the calculation we can use the matricial form:

$$\left[M\right]\mathbf{x} = \mathbf{v} \tag{1.69}$$

$$\mathbf{x} = \begin{bmatrix} A \\ B \\ C \\ D \end{bmatrix} \qquad \mathbf{v} = \begin{bmatrix} T_{tum} - \left(T_a + \frac{\dot{q_{m1}}}{\omega_1 \rho_b c_b}\right) \\ \frac{1}{\rho_b c_b}\left(\frac{\dot{q_{m2}}}{\omega_2} - \frac{\dot{q_{m2}}}{\omega_1}\right) \\ 0 \\ h\left[T_\infty - \left(T_a + \frac{\dot{q_{m1}}}{\omega_1 \rho_b c_b}\right)\right] \end{bmatrix} \tag{1.70}$$

$$\left[M\right] = \begin{bmatrix} 1 & 1 & 0 & 0 \\ e^{m_1 R_1} & e^{-m_1 R_1} & -e^{m_2 R_1} & -e^{-m_2 R_1} \\ m_1 e^{m_1 R_1} & -m_1 e^{-m_1 R_1} & -m_2 e^{m_2 R_1} & m_2 e^{-m_2 R_1} \\ 0 & 0 & e^{m_2 R_2}\left(h + k_2 m_2\right) & e^{-m_2 R_2}\left(h - k_2 m_2\right) \end{bmatrix} \tag{1.71}$$

We can obtain easily the vector of coefficients $\mathbf{x}$ if we get the inverse matrix of $|M|$. The size of the matrix is 4x4 therefore there is not any computational problem.

$$\mathbf{x} = \left[M\right]^{-1} \mathbf{v} \tag{1.72}$$

If we implement the problem in Matlab we can evaluate the influence of some parameters on the distribution of temperature. We have set the model with $h = 5W/(m^2K), k_1 = 0,5W/(mK), k_2 = 0,3W/(mK), R_1 = 0,027m, R_2 = 0,030m, q_{m1} = 3000W/m^3, q_{m2} = 3000W/m^3, \omega_1 = 0,002s^{-1}, \omega_2 = 0,005s^{-1}, \rho_b = 1000kg/m^3, c_b = 3639J/(kgK), T_\infty = 20°$ Important parameters are $\omega_1, \omega_2, h, T_\infty$. The first two quantities are determined by the reaction of the body to external events. Instead, h and T_∞ can be controlled by a person due to the introduction of the water bolus. The water bolus can be used to cool the skin, and also if there is a forced recycle of the water, the convection coefficient of the heat exchange can be modified. We can evaluate the thermal impact of water or air at the skin level, comparing the obtained results. The influence of the different thermal parameters are reported in Figure 1.3.

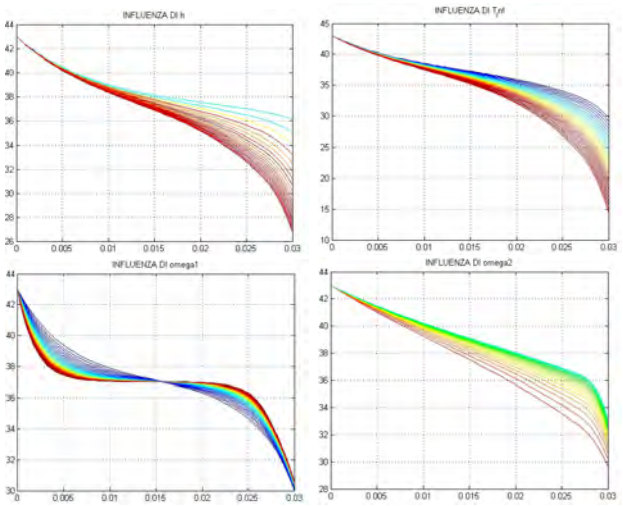

Figure 1.3: Temperature distribution parameterized by $h, T_\infty, \omega_1, \omega_2$.

Chapter 2

FE Modeling of Applicator and Tissues

In this chapter, the projected model will be described in each step of implementation in COMSOL Multiphysics. The values used for the definition of the geometry will be motivated in the next chapters. The description doesn't respect the chronology but it follows the main categories of FE modeling.

2.1 Basics of Finite Element Analysis

Finite Element Analysis is a method used for the resolution of generic systems of partial differential equations (PDE), which is expressed in a discrete and approximated form. This method allows us to solve field problems that are defined by complex geometries and constraints. Therefore it's possible to define more governing equations, allowing us to deal with coupled physical problems, e.g. fluid dynamics, mechanics , thermodynamics, electromagnetics, etc. The analysis can be divided in three parts

- Pre-processing: development of the model (geometry, mesh, material, solver).
- Solver: Linear or not linear system solution.
- Post-processing: elaboration and management of results.

This analysis can be performed in different ways for the same model, depending on the particular phenomenon that is studied. For instance, the solution can be found over the frequency domain for cyclic problems, over the time domain for transient problems, or only at the final values for steady state cases, and so on. It's very important the definition of the boundary

and initial conditions as well as the definition of the constraints and sources of the model. If all these conditions are not correctly imposed, the solving algorithm does not converge to the solution, or the results can be wrong. The models can be 0D, 1D, 2D, 3D, and these domains are discretized by nodes. At each node is applied a computation by the solver, therefore the density of nodes is a crucial issue for the validation of the results. The connection of two adjacent nodes is called edge, and the surface defined by a loop of edges is called element. Every element is defined by a specific material and other physical properties, also they have to be realized following precise topological conditions:

- Every edge cannot intersect any other edge.
- Vertexes of a certain elements cannot lay on the edge of an other element.
- The entire domain has to be covered by elements.

When all the elements of the domain are defined, we can also decide the order of interpolation of the shape functions (piece-wise functions that have 1 on a chosen central node and go to 0 moving toward the adjacent nodes). In case of a second order interpolation or, in general, higher order interpolation, the computational complexity arises dramatically. Therefore, a sophisticated trade-off between approximation and time performance has to be done.

The core of the method consists in the assembly of a matrix that minimizes the energy state of the system (variational method) or a weighted residual that can be considered as the error of computation. This matrix (it is called stiffness matrix because it was used at first for mechanical problems) has to be inverted using mathematical techniques that can be classified as direct or iterative. Depending on the specific algorithm used, the necessary hardware resource can be very different (especially for RAM and CPU). The boundary conditions and the sources became the known terms vector. When the unknown values are found (usually scalar and vector potentials), it is possible to obtain the field functions applying approximated differential operators (curl, gradient, divergence).

An important issue is the management of the hardware resources that are required to solve engineering and physical problems with acceptable computation time. A lot of RAM capacity is required to storage rapidly all the data that are necessary for the inversion of a big size matrix. Also, the processors have to be powerful to compute a big amount of elementary operations in a little time. Furthermore, more processors can be used in parallel to optimize the computation. Some of the most important FEM softwares for

electromagnetic and thermal problems are FLUX, ANSYS, and COMSOL Multiphysics. The simulations developed in the next sections are performed using COMSOL 4.3b.

2.2 General Schema of the System

The system that has to be studied for the Hyperthermia Treatment Planning is composed of two identical patch antennas, which produce an alternating electromagnetic field, in order to generate heat sources inside an organic tissue. The patch antennas are fed by coaxial cables with characteristic impedance $Z_c = 50\Omega$. The operating frequency is 2.45 GHz, and the array is spatially defined by a linear pattern. The organic tissue is assumed to be cylindrical, and the tumor is modeled as a truncated cylinder in the skin layer. The environment is characterized by atmospheric pressure and by 25°C of temperature. The heat exchange between the body and the environment is due to the thermal convection. Thermal radiation can be neglected since the temperature of the heated organic tissues is low, as well as the thermal conduction in air can be neglected. The external box that includes the entire system is a parallelepiped that is perfectly electromagnetic isolated from outside, and it absorbs totally the radiation from inside. A scheme of the overall system is reported in the Figure 2.1. The geometry of the patch

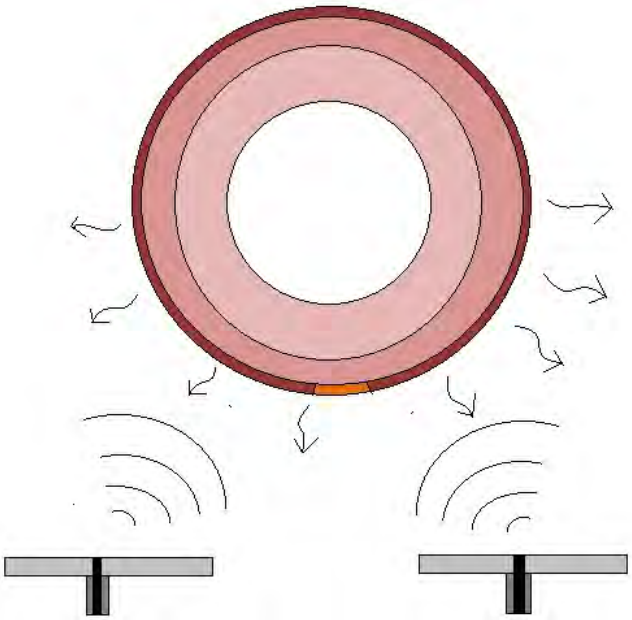

Figure 2.1: Schema of the overall system.

antenna is characterized by the dimensions of the metallic resonant cavity and by the dimensions of the dielectric slab. Also, the position of the coaxial feeder is fundamental to obtain an efficient radiation, because we need to match the electromagnetic device with the power supply line. The main sizes of the radiating patch antenna element are presented in the Figure 2.2. The purpose of developing a FEM model of the patch antenna and of the

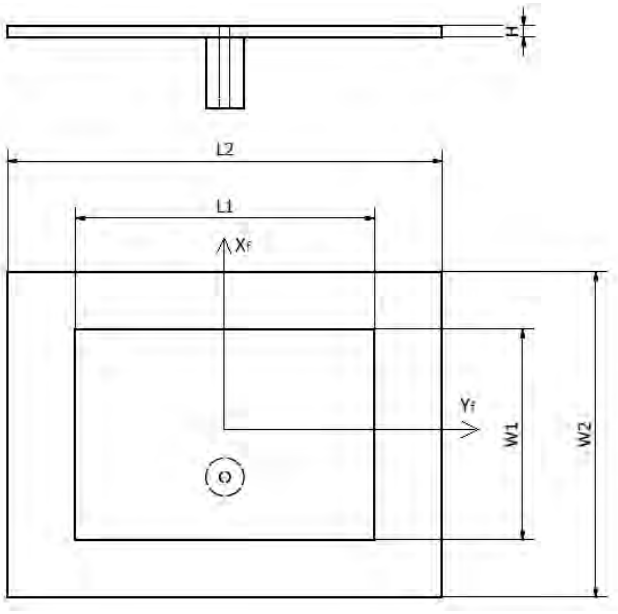

Figure 2.2: Main dimensions that characterize the patch antenna.

organic tissues can be synthesized by two fundamental points:

- Project of the electromagnetic prototype.
- Analysis of the thermal behavior of the system.

All the considerations regarding the optimal dimensions of the antenna are presented in Chapter 3, and the analysis of the thermal response is developed in Chapter 5. In the following section the building of the model is presented in each pahse of the model construction.

2.3 Model Implementation in COMSOL

The model implemented for the Hyperthermia study is 3D, and it is characterized both by electromagnetic propagation and biological heat transfer. The simulation modules that are used deal with the Maxwell and Pennes

PDE (equations considered in Chapter 1). The analysis is performed over the frequency domain for the electromagnetic problem, and the time domain for the thermal problem. The entire model is developed through parametric quantities.

2.3.1 Geometry Definition

The geometry of the model is constituted in three parts: the box that contains the system, the array that is formed by two (identical) elements, and the thermal load. The box defines the zone of computation, and its boundary is the surface where the boundary conditions of the PDEs are imposed. The patch element is defined as a parallelepiped $L_{xslab} \times L_{yslab} \times h_{slab}$ (dielectric slab) with inside an other parallelepiped $L_{xpatch} \times L_{ypatch} \times h_{patch}$ that is defined by the size of the metallic resonant cavity. The thickness of the metal is neglected (the real value is 0.0035 mm), so the metallic patch is only 2D. The feeder is a coaxial cable that can be implemented by two coaxial solid cylinders r_{in}, r_{out}. The inner cylinder is directly connected to the upper face of the parallelepiped instead the outer cylinder is connected to the lower face. The thermal load is defined by four coaxial cylinders with radii $r_{bone}, r_{bone} + h_{muscle}, r_{bone} + h_{muscle} + h_{fat}, r_{bone} + h_{muscle} + h_{fat} + h_{skin}$ (perpendicular to the feeder axis), forming the different layers of the tissues. The volume of the tumor is defined by a series of boolean operations: first a cone with the base in middle position of the load is created, then the intersection between the most external cylinder and the cone is applied. The created form is a truncated cylinder with the same thickness of the skin layer. This geometry defines all the interfaces between different materials, but also other volumes in the domain can be created only to obtain more mesh control. These volumes are removed after that the mesh is created. The geometry of the entire system is presented in Figures 2.3 and 2.4.

2.3.2 Material Parameters

The materials that are used to define the antennas are: PTFE for the dielectric insulation of the coaxial feeder and FR4 (common material for PCB) for the dielectric slab. The metallic components are assumed to be as perfect electric conductors (PEC), since this condition is acceptable in the frequency range of microwaves. The thermal load is modeled by different layers: bone, muscle, fat, skin and the tumor. The material properties of all these elements are presented in Table 2.1. [5], [6]

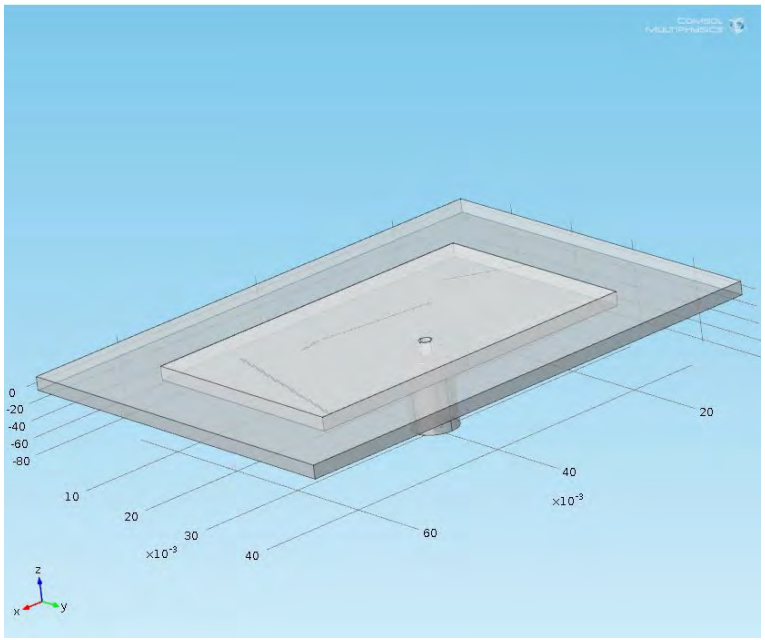

Figure 2.3: Geometry of the patch antenna.

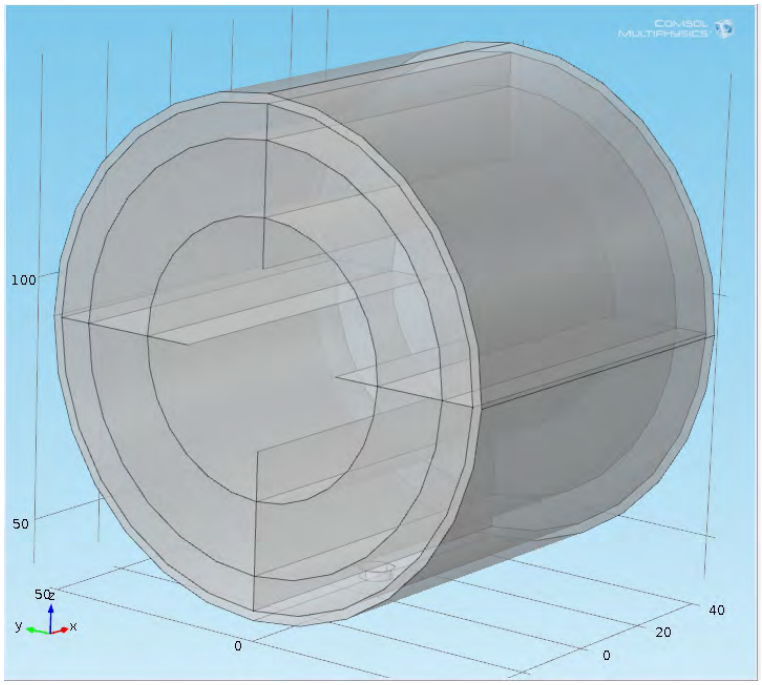

Figure 2.4: Geometry of the organic tissue.

Material	μ_r [1]	ϵ_r [1]	σ $[S/m]$	k $[W/(mK)]$	ρ_m $[kg/m^3]$	c $[J/(kgK)]$
Air	1	1	0	-	-	-
FR4	1	4.7	0.006403	-	-	-
PTFE	1	2.3	0	-	-	-
Skin	1	37	0.70	0.30	1100	3400
Fat	1	14.6	0.33	0.25	920	2500
Muscle	1	61	1.31	0.50	1041	3500
Bone	1	22.5	0.17	0.40	1500	1300
Tumor	1	59	0.65	0.50	1050	3639

Table 2.1: Electromagnetic and thermal properties of the materials used in the model.

2.3.3 Mesh Optimization

The phase of mesh defining is one of the most critical part of implementation, because we need to assure accuracy but also considering the computation time. Let us start with the mesh defining of the patch antenna. If we use two simulation softwares (COMSOL and CST) that use different algorithmic formulations (FEM and FDTD), we have to increase the mesh density until we obtain the same numerical results from the solutions, as represented in Figure 2.5, making a comparison of the scattering parameter S_{11}. An extremely fine mesh is set in every regions of the domain. The plot 2.5 shows the good match between the two initial meshes. Since the results are similar,

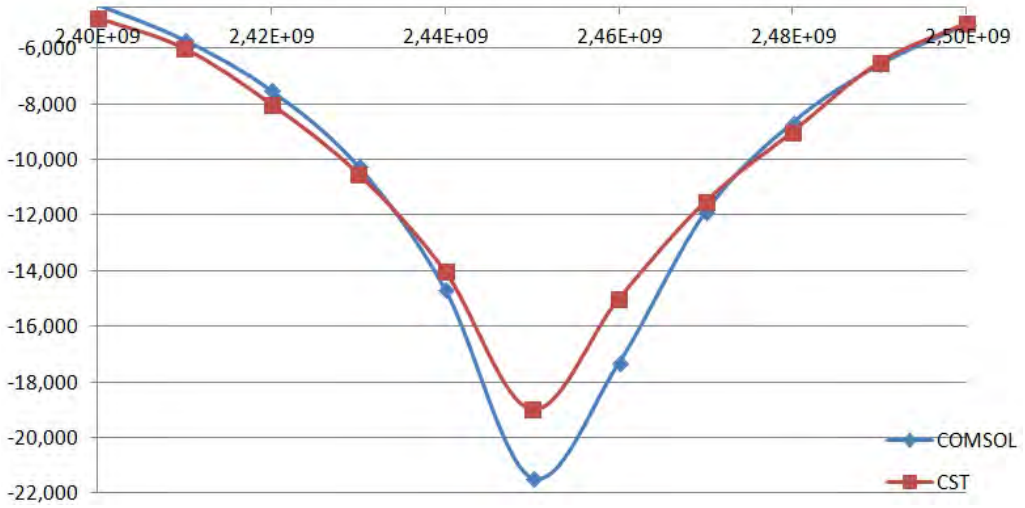

Figure 2.5: Comparison between COMSOL and CST results.

we can assume that the mesh of the problem is enough refined[1]. Next, it's important to reduce the mesh in specific regions to reduce useless over accuracy. We need to define some key-areas and key-volumes that are involved by high magnitude of field gradients. These regions are:

- Coaxial cable (solid cylinders).
- Dielectric slab (solid parallelepiped).
- External boundary of the slab (surface).
- Patch (solid parallelepiped that is a sub-domain of the dielectric slab).
- External boundary of the patch antenna (surface).
- Air (remaining volumes).

Since we are implementing an electromagnetic and thermal problem, an interesting parameter can be the efficiency of radiation from the device. So, we can consider the reflection coefficient S_{11} of the patch antenna and the corresponding η.

$$\eta = 100\left(1 - 10^{\frac{S_{11}}{10}}\right) \tag{2.1}$$

We can accept an error about 2-3% (considering η) with respect to the starting solution. We should note that there are regions that do not influence the electromagnetic behavior, but their mesh is however crucial for the geometry and position. For instance, the inner cylinder of the feeding coaxial cable is placed in a position close to the electromagnetic port, and also the field out of the cable is really intense. Anyway, the region defined by this cylinder is completely not involved by the propagation because the constitutive material is PEC. The mesh in this region is necessarily extremely fine, but it is excluded from the electromagnetic domain.

The development of the mesh was done considering the specific regions listed above. In order to assess correctly the variation between the solutions, we have evaluated S_{11} and η at the central value of the ISM band (2.45 GHz) and at the border values of the band (2.4 GHz- 2.5 GHz). An example of the mesh reduction process is depicted in Table 2.2. The underlined value is the definitive Mesh Size (MS) selected for the model. The final mesh for the patch antenna is represented in the Figure 2.6. The total time for one simulation

[1]the geometry that was defined for the comparison is not actually important, we have to assess only the matching between the results.

	Freq. [GHz]	MS=0.25 mm	MS=0.55 mm	MS=0.85 mm
$S_{11}[dB]$	2.4	-4.416	-4.95	-0.412
	2.45	-21.42	-20.82	-15.70
	2.5	-5.319	-4.55	-0.594
η [%]	2.4	63.82	68.07	9.06
	2.45	92.28	99.17	97.31
	2.5	70.62	64.97	12.79

Table 2.2: Dependence of the radiation efficiency by the mesh size in the patch antenna border.

is about 1 minute using a direct solver with 48 GB RAM and two processors 2.4 GHz Quad Core CPU. Since the array is composed of two elements, the second patch has actually the same mesh of the antenna described above. Now we have to complete the mesh of the model considering the thermal load. First, we observe that a tetrahedral mesh is much more dense than the mapped mesh when we impose the maximum size element of tetrahedrons equal to the distance between two swept layers. We prefer the mapped mesh since its numerical errors are more limited. Two topological observations have to be done: the central region of the cylindrical thermal load has to be tetrahedral otherwise we obtain a geometrical singularity along the axis; the external layer (skin) has to be tetrahedral because it keeps an other volume inside (tumor) that is not radially defined (we could create intersections between different edges). If we analyze the electric field that is inside the load, we observe that the lateral part is actually not interested by the field. Instead the central and especially the lower part is the region with the highest magnitude of E. This observation implies that if we calculate the solution with a less dense mesh in the lateral volumes we should save computational time, without a reduction of accuracy. Unfortunately the model built with this new mesh cannot converge to a solution using the direct solver, so the former mesh has to be applied to get convergence. Now that we have chosen the form of the elements in the domains, we have to impose the correct size of the elements in the different layers. In the tumor region it's convenient to set an extremely fine mesh to have more control in the most crucial domain. The mesh size in the tumor is tetrahedral and its maximum element size is 0,5 mm. We can assess the wavelength in the materials and therefore we evaluate the optimal mesh size as a part of $\lambda_{material}$. The value n that appears in Table 2.3 is the number of divisions that is considered per wavelength. Also, we have to consider the thickness of the layers h_{skin}, h_{fat}, h_{muscle}, h_{bone}, r_{bone} (the first and the last domains are tetrahedral and the remaining domains

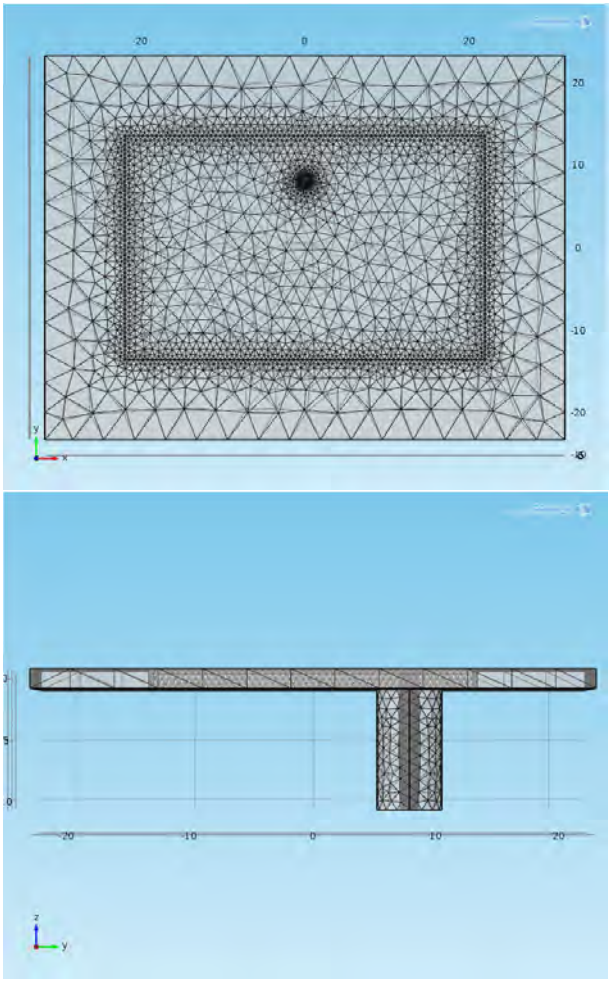

Figure 2.6: Definitive mesh of the patch.

are mapped). The Max Element Size (MES) of tetrahedrons is defined as follows:

$$MES = \frac{\lambda_j}{n} \qquad j = 1, 5 \tag{2.2}$$

where j=1 is referred to the skin layer and j=5 is referred to the central region of the bone. For the mapped mesh, the number of swept planes is:

$$n_j = n\frac{h_j}{\lambda_j} \qquad j = 2, 3, 4 \tag{2.3}$$

where j=2 is referred to the fat layer, j=3 is referred to the muscle layer, and j=4 is referred to external region of the bone.

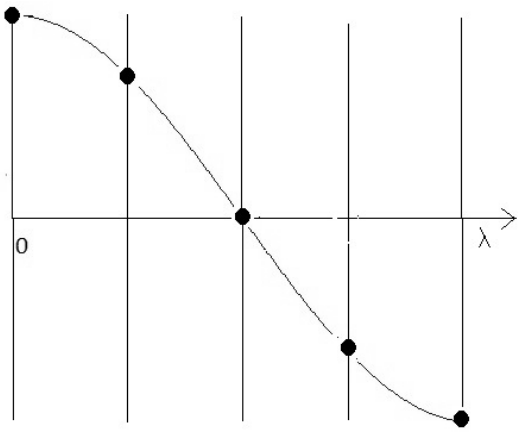

Figure 2.7: Example: division of the domain by 9 nodes and 8 elements per λ (in the figure, only $\lambda/2$ is represented).

	Material	n=4	n=5	n=6	n=7	n=8	n=9	n=10
MES	Skin	5.0	4.0	3.4	2.9	2.5	2.2	2.0
	Fat	8.0	6.4	5.3	4.6	4.0	3.6	3.2
	Muscle	3.9	3.1	2.6	2.2	2.0	1.7	1.6
	Bone	6.5	5.2	4.3	3.7	3.2	2.9	2.6
	Tumor	4.0	3.2	2.7	2.3	2.0	1.8	1.6

Table 2.3: Example of computation of the Maximum Element Size (MES) for different domains.

We should point out that the computational time for n=4 is about 8 minutes, while for n=10 it is about 17 minutes. Finally, the appropriate value is considered n=7 that implies the simulation time about 10 minutes. A further improvement can be obtained applying the option "mesh control faces", and creating a virtual volume that contains the tumor region. This zone can be characterized by a tetrahedral refined mesh (same maximum size of tumor). In this way we have created the definitive mesh of the entire system considering the trade-off between accuracy of results and computational time. The definitive mesh of the load is shown in Figures 2.8 and 2.9.

2.3.4 Physics Setting

The physics implementation has been done by two software modules "electromagnetic waves (emw)" and "bioheat transfer" (ht).

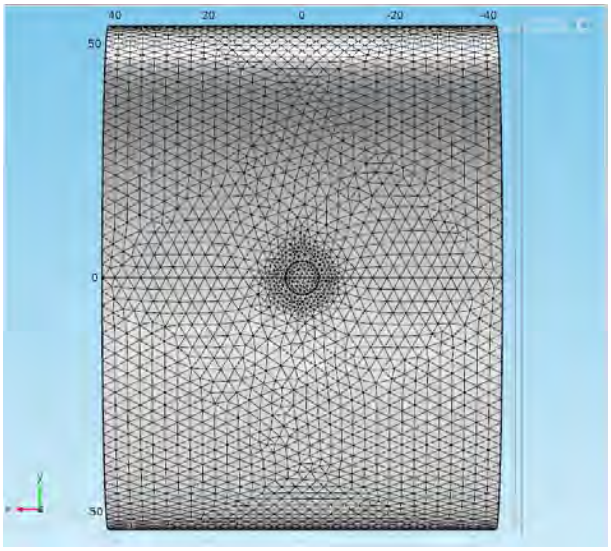

Figure 2.8: Definitive mesh of the load.

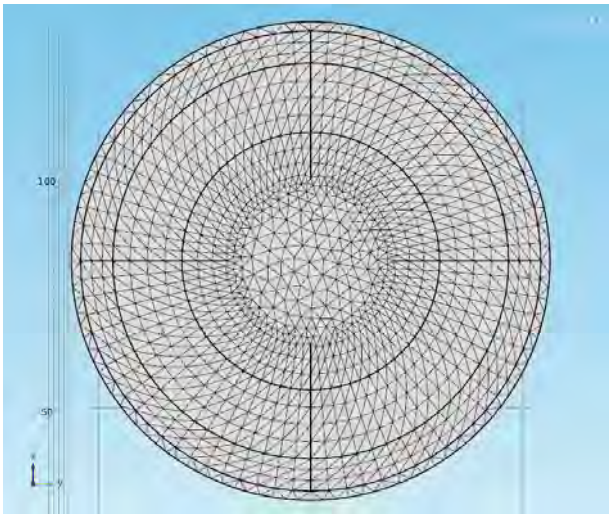

Figure 2.9: Definitive mesh of the load.

Electromagnetic Waves

The governing equation of the electric field in the frequency domain has been defined by the simulator as follows:

$$\nabla\times \mu_r{}^{-1} (\nabla\times \mathbf{E}) - k_0^2 \left(\epsilon_r - \frac{j\sigma}{\omega\epsilon_0}\right)\mathbf{E} = 0 \tag{2.4}$$

where k_0 is the propagation constant $[m^{-1}]$. The other parameters are the same which were already presented in the Chapter 1. The initial conditions for the entire domain are $\mathbf{E} = 0$. The boundary conditions that are defined on the external box represent the perfect scattering conditions. The equation that is actually solved is:

$$\mathbf{n}\times(\nabla\times\mathbf{E}) - jk\mathbf{n}\times(\mathbf{E}\times\mathbf{n}) = -\mathbf{n}\times(\mathbf{E_0}\times(jk(\mathbf{n}-\mathbf{K_{dir}})))e^{-j\mathbf{k_{dir}}\cdot\mathbf{r}} \tag{2.5}$$

where $\mathbf{k_{dir}}$ is the direction of the incident wave in every position on the external border. The energy inputs of the system are defined by two coaxial waveguide ports. At each port the following equation holds for the scattering parameter:

$$S_{jj} = \frac{\int_{\Omega_j}(\mathbf{E}-\mathbf{E_j})\cdot\mathbf{E_j}}{\int_{\Omega_j}\mathbf{E_j}\cdot\mathbf{E_j}} \qquad j = 1,2 \tag{2.6}$$

where Ω_1 and Ω_2 are the areas of the two ports, instead $\mathbf{E_1}$ and $\mathbf{E_2}$ are the incident electric fields. The amplitudes and the phases of the feeding power inputs are defined by P_1, P_2, ϕ_1, ϕ_2. The metallic components are characterized as perfect electric conductors (PEC), so the condition of perfectly perpendicular electric field on the surface is considered as follows:

$$\mathbf{n}\times\mathbf{E} = 0 \tag{2.7}$$

If this law is valid on the domain boundary, it is also known as Neumann boundary condition.

Bioheat transfer

The bioheat transfer model is based on the Pennes equation

$$\rho c_p \mathbf{u}\cdot\nabla T = \nabla\cdot(k\nabla T) + Q + Q_{bio} \tag{2.8}$$

where the biological heat is produced as follows:

$$Q_{bio} = \rho_b c_b \omega_b (T_b - T) + Q_{met} \tag{2.9}$$

and T_b (blood temperature that comes from an artery) is set to $309,15K$ (36°C). The specific heat of blood is $c_b = 3770[J/(kgK)]$[6] The perfusion values[2] that have been assumed in the model have been derived from scientific literature[7], [5].

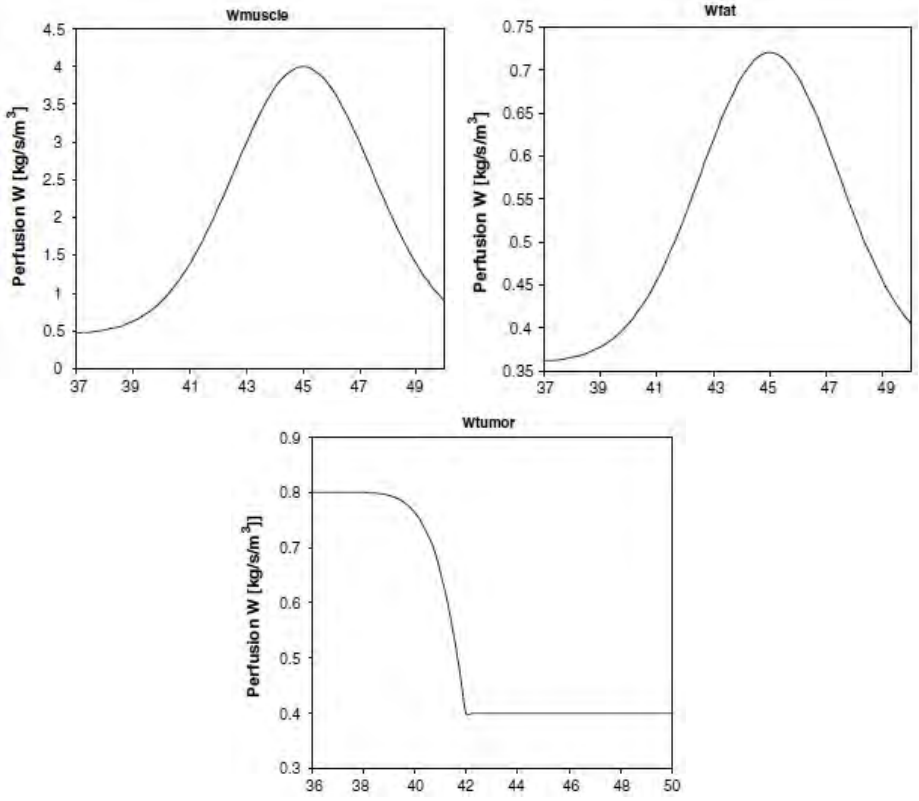

Figure 2.10: Blood perfusion in different tissues

$$W_{muscle} = 0,5 + 3,5exp\left[-\frac{(T-45)^2}{12}\right] \tag{2.10}$$

$$W_{skin/fat} = 0,36 + 0,36exp\left[-\frac{(T-45)^2}{12}\right] \tag{2.11}$$

$$W_{tum} = \begin{cases} 0,8 & T < 37 \\ 0,8 - (T-37)^{4,8}/5400 & 37 \leq T \leq 42 \\ 0,38 & T > 42 \end{cases} \tag{2.12}$$

[2]The values presented in the model are defined by the product $W_{tissue} = \omega_b \rho_b [kg/(m^3 s)]$.

The bone is set with $W_{bone} = 0$ $[m^3/(kgs)]$. The circular faces of the cylinder have been set by the condition of thermal insulation:

$$-\mathbf{n} \cdot (-k\nabla T) = 0 \tag{2.13}$$

The initial temperature is assumed at $293,15K$ (environmental temperature 20°C). The thermal sources are caused by the electromagnetic dissipation of energy into the conductive materials. The heat exchange through the lateral surface is implemented by the Newton's law of convection:

$$-\mathbf{n} \cdot (-k\nabla T) = h(T_{ext} - T) \tag{2.14}$$

where the value of the effective heat exchange coefficient is $h = 5[W/(m^2K)]$ and the external temperature is $T_{ext} = 293,15K$

2.3.5 Computational Solver

The electromagnetic problem is defined in a high dense domain, therefore it is too complex to be analyzed by a direct solver. The iterative solver that was applied in the model is BicGstab, which is a variation (faster and more stable to get convergence) of the bi-conjugate gradient method. Instead, the thermal problem is solved for a smaller domain, so we can use a direct solver. The direct solver that was utilized is PARDISO. PARDISO allows us to invert sparse, symmetrical (also not symmetrical) matrices, through an exploitation of shared-memory and also distributed-memory multiprocessors.

The velocity of evolution of the thermal problem is lower than the velocity of the electromagnetic problem, so we can assume that the electric and magnetic fields can be computed considering the temperature (and also the material properties) as constant quantities (thermal properties at the beginning state). On the other hand the simulation results of the thermal problem can be computed when the electric and magnetic fields are in steady state. Since the phenomena evolve with different time constant, we can actually separate the computation of the physics modules. Proceeding in this way, we can obtain a big advantage because we can save computational time.

2.4 Post Processing Elaboration

When the computation is completed we can derive and elaborate all the information from the model. In particular, we are interested on the field distribution both for temperatures and for EM fields. It's important to evaluate global parameters that give the user some information about the physical

behavior of the system. In the studied problem we have to assess for each simulation (at least) the following:

- Electric field in the dielectric material of the patch applicators.
- Superficial temperature of the organic tissue.
- Isothermal surfaces.
- Temperature distribution on a vertical slice (in the middle of the tissue).

and also the numerical paramters:

- Electrical transmission efficiency (S_{11} or η).
- Local dissipated heat (tumor).
- Total dissipated heat (entire tissue).

With these data it's possible to evaluate exactly if the device is operating effectively. Also these parameters can be used to control the system and to obtain a focused heating. The next figures show a few examples of computed results in COMSOL. All these models will be analyzed in Chapter 4 through a series of parametric analyses, changing the main characteristics of the applicator. A few examples of the main field distributions of the model are presented from Figure 2.11 to 2.17.

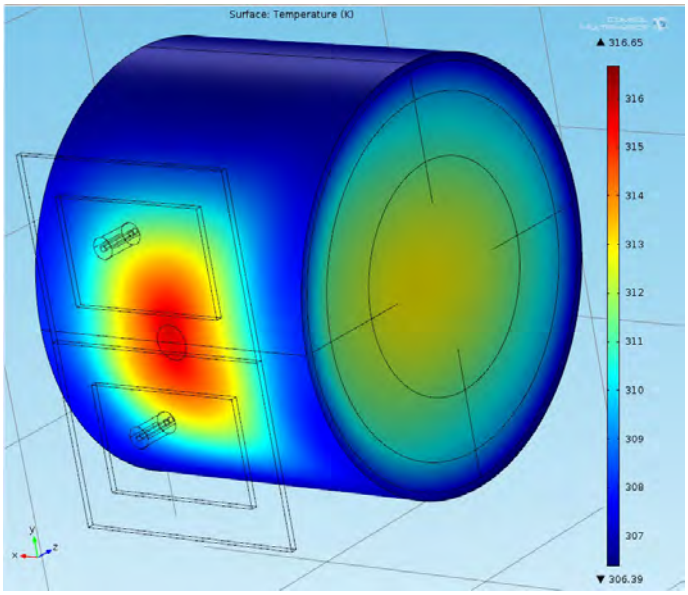

Figure 2.11: Superficial temperature [K] on the external surface of the thermal load (skin).

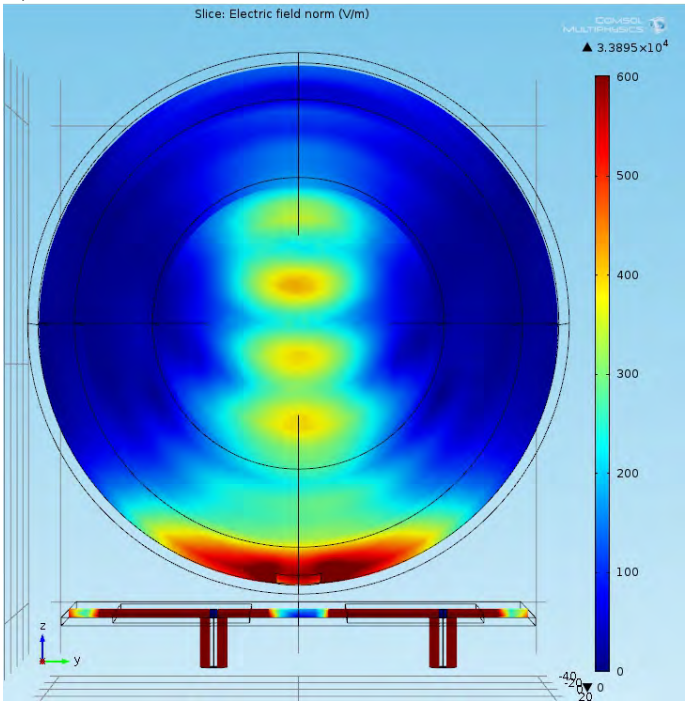

Figure 2.12: Electric field [V/m] on a plane that is vertically positioned, at the center of the tissue. Let us remind the schematic Figure 2.1.

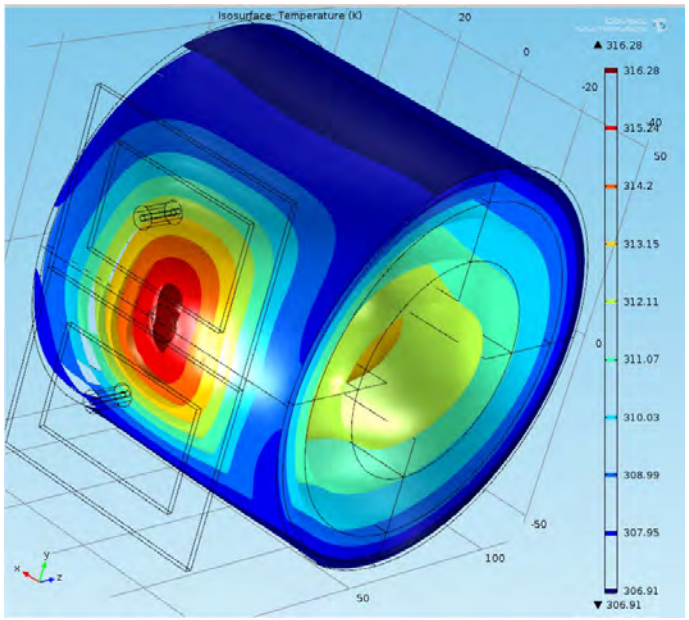

Figure 2.13: Isotemperature surfaces [K] inside the tissue.

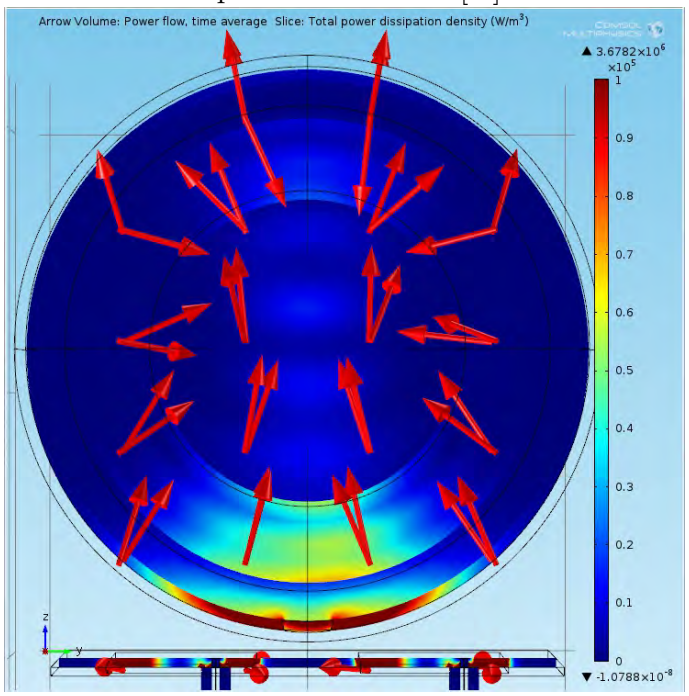

Figure 2.14: Direction of the heat flow [W/m^3] and dissipated power density.

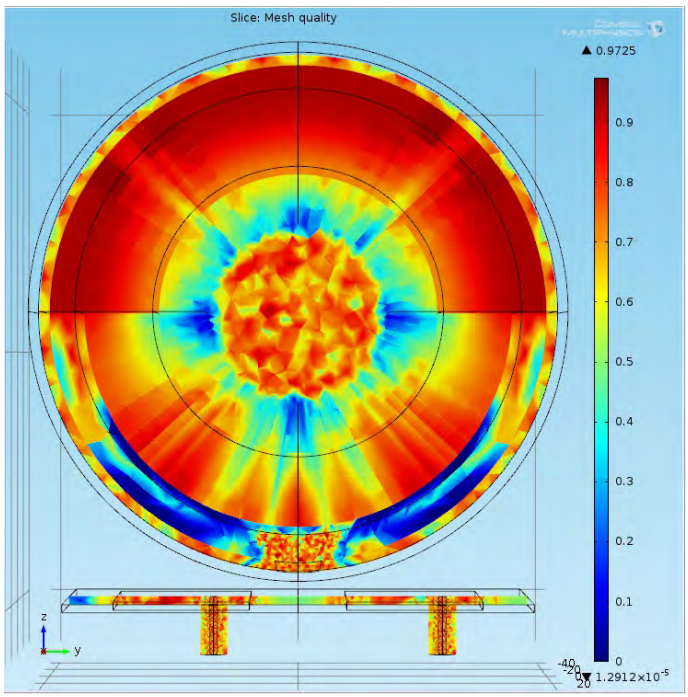

Figure 2.15: Representation of the mesh quality [1] of the system.

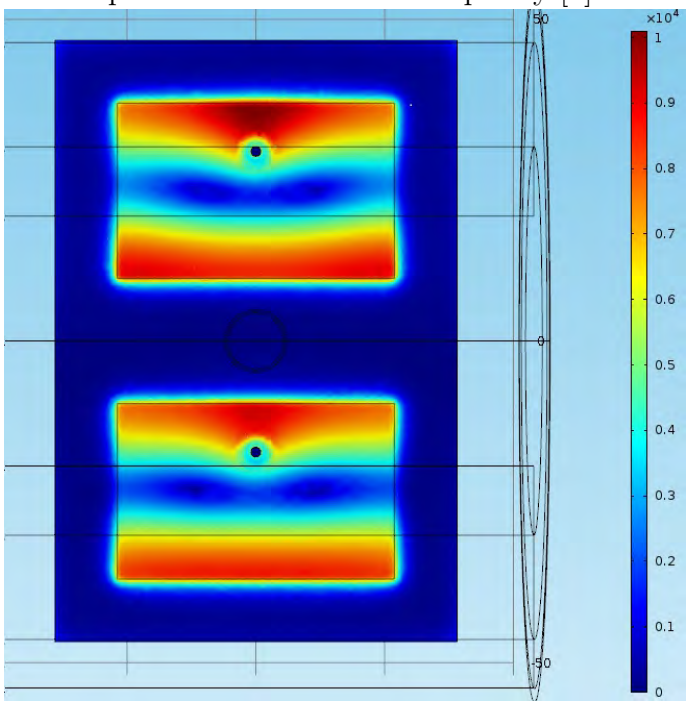

Figure 2.16: Magnitude of the electric field [V/m] on the plane XY that passes in the middle of the dielectric material.

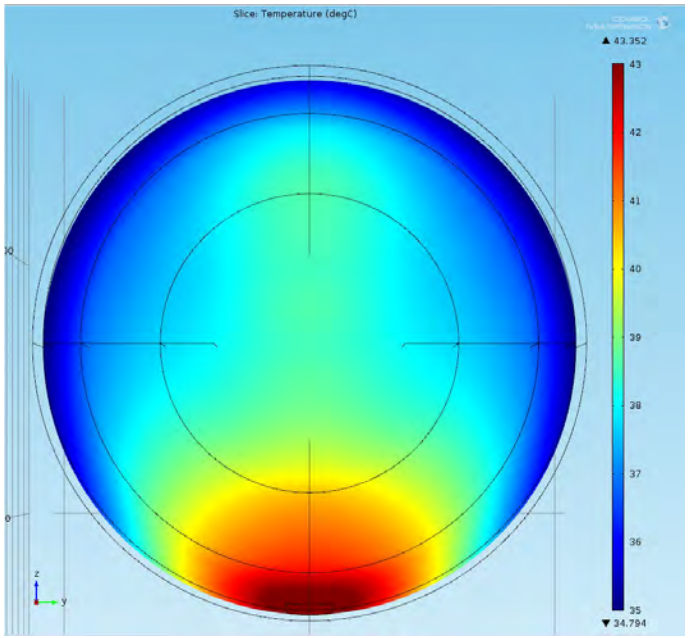

Figure 2.17: Temperature distributions [°C] on the YZ cross section.

Chapter 3

Antenna and Array Design

3.1 Fundamentals of Patch Antennas

Patch Antenna is a dielectric slab (PCB) which has an upper metallic rectangle and a lower ground plate layer. The upper rectangle is the resonant cavity where the electromagnetic field radiates, and it is the "high" voltage component. The antenna can be fed in different ways: microstrip line, capacitive coupling, and coaxial feeder[1]. The internal conductor of the coaxial cable works as coupler of the electromagnetic field between the cable and the slab. The main dimensions are designed in such a way that the patch operates at the resonance frequency. So it's necessary to impose that the length of the metallic rectangle cavity is equal to $\lambda_0/\sqrt{\epsilon_r}$ (necessary condition to have stationary waves). If we consider the distribution of the fields, we can observe that the electric field has a positive peak on one side of the patch, and on the other side we have a negative peak. At the border, the electric fields don't decrease sharply but they extend the field lines into the dielectric material. Over a certain length the field lines change their direction turning by 180° (fringing fields). The fundamental mode of propagation is ${TM_{10}}^2$ with the nonzero components $E_z, H_x H_y$. We can evaluate the scalar quantities voltage and current on the patch. Let's consider the axis defined by the shortest side of the rectangle (length). Along the border, the current is zero because there is the discontinuity of the conducting material, instead at the center we have the peak of current. On the other hand, if we consider the voltage, we have the same trend of the magnitude of the electric field, so a maximum positive peak on one side and a negative peak on the other side.

[1] from here on we consider only the case of coaxial feeder.

[2] since the cavity is 3D we should use 3 subscripts, but along the z-axis the changes are negligible $TM_{100} \rightarrow TM_{10}$.

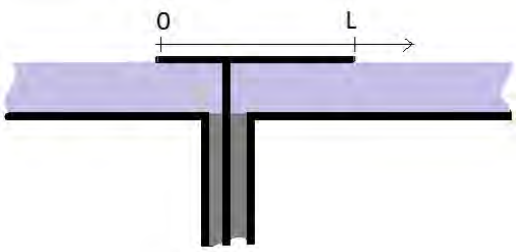

Figure 3.1: Patch antenna fed by coaxial line

This behavior is understandable since the length of the patch is $\lambda/2$, so two points that are separated by this distance are polarized with a phase-shift of π. At the center of the patch the voltage is circa zero. Since the impedance is defined by a ratio between voltage and current we can roughly evaluate that the impedance has a minimum at the center, and it arises moving to the sides. In Figure 2.2 the magnitudes of the current, voltage and impedance have been plotted referring to a middle axis.

The coaxial cable has to be placed in an appropriate way to get the matching of the device. The correct position is somewhere in the middle between the center ($|Z| = 0$) and the borders ($|Z| = Z_{max}$) to obtain the 50Ω value. The typical radiation pattern of a patch antenna is defined by a directivity in the range 8-9 dB. The main factors that influence the directivity are the ground plane and the fringing fields (two lateral slots). The patch antenna, if it is fed by the fundamental mode, has its maximum directivity along the the axis perpendicular to the plane containing the slab. This is the typical behavior of broadside antennas.

An other characteristic that is usually considered is the polarization of the radiated electric field. A common patch, that is fed by mode TM_{10} is characterized by linear polarization, since the electric field varies only along one direction. The polarization plane depends on the position of the plane where the current flows. If the patch is vertically oriented or horizontally oriented the polarization can be controlled. In our case, for heating purpose, we can neglect the polarization because we are interested only on the magnitude of the electric field.

The bandwidth is usually pretty small, in fact its typical value is about 3% of the resonance frequency. This is the main disadvantage of this kind of antenna. Anyway, we can obtain a good performance if we choose properly certain dimensions. These dimensions are the height of the dielectric slab, the width of the metallic patch, and also the $tan\delta$ of the materials. In general, patch antennas are good radiant elements that are suitable for

many applications thanks to their simplicity and cheapness. By choosing the convenient size and the materials, the patch elements can be adopted at very different frequency and also at different power. Since they have a planar structure, they can be easily integrated in an array configuration both in 2D pattern or also in 3D pattern (usually in the radio-frequency range).

In the next section, a patch antenna, operating at 2.45 GHz, is designed using COMSOL Multiphysics. The section later deals with the composition of a linear array and the resulting electromagnetic radiation pattern in the farfield region[3]. The considerations of the thermal load are not considered in this chapter.

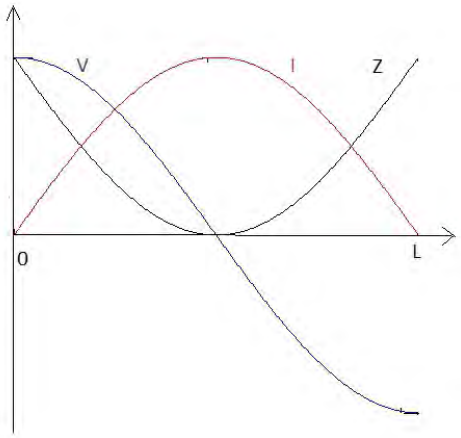

Figure 3.2: Magnitude of current, voltage and impedance along the X-axis

3.2 Geometry and Materials

The elements which form the array are 2 independent rectangular patch antennas. The elements are placed on a plane and they are fed by two independent coaxial transmission lines. Therefore we have to define the appropriate dimensions and configurations of the following components for each element of the array:

- Dielectric board.
- Feeding coaxial lines.

[3]the farfield region is defined as the zone external to the Fraunhoffer radium

- Resonant cavity.

We have to design all these elements for the operating frequency of 2.45 GHz, and we need to minimize the reflected power by matching the device with a 50 Ohm feeder.

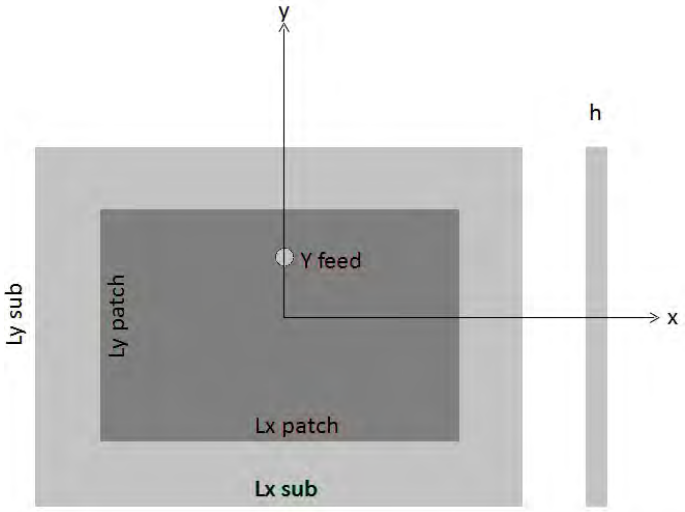

Figure 3.3: Representation of the patch antenna.

3.2.1 Dielectric Board

Since we want develop a device that irradiates electromagnetic field, the best solution is to choose a material with the dielectric permettivity as low as possible. At the same time we have to take care of the thermal losses, caused by the less effective isolation. Typical values of relative permittivity for antennas are between 2.2 and 12. In this project FR-4 dielectric is used, that is a typical composite material for printed circuit boards. At 2.45 GHz its relative permittivity is $\epsilon_r = 4.7$. The thickness of the board is another important parameter that influences the radiated power, in fact the bigger the dielectric height, the greater the radiated power from the antenna. Also, the bandwidth can be increased if we use a thicker board. Even if we operate with monochromatic waves, in case of distortion of the waveform for thermal load, we actually desire a good behavior over the frequency domain. The height is usually $h \ll \frac{1}{10}\lambda_0$ [9].

$$\lambda_0 = \frac{c_0}{f} = \frac{3 \cdot 10^8 m/s}{2.45 \cdot 10^9 Hz} \approx 12.2cm \tag{3.1}$$

In the project we consider $h = 1.6$ mm. The inhomogeneity of the materials induces us to evaluate a new dielectric constant that makes into account the fringing of the field. This new parameter is called *effective dielectric constant* ϵ_{re}, and it satisfies the relation $1 < \epsilon_{re} < \epsilon_r$. If we want to assess an approximated value of ϵ_{re} [1]:

$$\epsilon_{re} = \frac{\epsilon_r + 1}{2} + \frac{\epsilon_r - 1}{2} \frac{1}{\sqrt{1 + 12h/W_0}} \approx 4.34 \tag{3.2}$$

3.2.2 Coaxial Line

The coaxial cable is actually a transmission line, with a certain characteristic impedance Z_0 which is defined by the geometry and by the properties of the dielectric layer. The electromagnetic field, considering the fundamental mode of propagation is a Transverse Electric and Magnetic (TEM). Let's assume that the dielectric material is not dissipative, then we can assess the ratio between the internal and external radium using the following equation: [1]:

$$Z_0 = \frac{60}{\sqrt{\epsilon_r}} ln\left(\frac{R_{out}}{R_{in}}\right) \tag{3.3}$$

$$\frac{R_{out}}{R_{in}} = e^{\frac{2Z_0\pi}{\eta}} \tag{3.4}$$

where η is the intrinsic impedance defined as $\eta = \sqrt{\mu/\epsilon}$ and substituting the values $Z_0 = 50\Omega$, $\epsilon = \epsilon_r\epsilon_0 = 2.3\epsilon_0$ (teflon) we obtain $R_{out}/R_{in} = 3.538$. The commercial size of the coaxial cable (SMA 141-7SM+) is $R_{out} = 2.7mm$ and $R_{in} = 0.76mm$.

3.2.3 Metallic Patch

Since we have derived ϵ_{re}, we can calculate the electromagnetic length of the patch element Ł$_e$ if we impose the resonance condition:

$$Ł_e = \frac{\lambda}{2} = \frac{c}{2f\sqrt{\epsilon_{re}}} \approx 29.37mm \tag{3.5}$$

This value is greater than the actual geometrical dimension of the resonant cavity because the field lines of the electric field tends to continue over the metallic rectangle. The field lines begin to curve into the dielectric layer after the distance ΔL_e [2]:

$$\Delta L_e = 0.412 \frac{(\epsilon_{re} + 0.3)\left(\frac{W_0}{h} + 0.264\right)h}{(\epsilon_{re} - 0.258)\left(\frac{W_0}{h} + 0.8\right)h} \tag{3.6}$$

that yields to $\Delta L_e = 0.73$ mm. Therefore the actual geometrical length is:

$$L = L_e - 2\Delta L_e \approx 27.9mm \tag{3.7}$$

Also, we can derive the width of the cavity as follows:

$$W = \frac{c}{2f}\sqrt{\frac{2}{1+\epsilon_r}} \approx 36.3mm \tag{3.8}$$

The initial position of the feeding line can be assumed circa at 6/10 of $L/2$. The exact value will be evaluated in the next section during the optimization process. We need to determine the dimensions of the ground plane that, in ideal case, is considered as an infinite plane. Actually, the ground plane is slightly bigger than the rectangular patch, causing a reduction of the performance of the antenna. We can assume that the ground plane has the sides greater than the cavity at least by 6 times the dielectric height [10]. Also we have to take into account that the patch element is not a stand alone antenna. The exact dimensions of the ground plane and the board can be decided only evaluating the behavior of the entire array, defining the pitch which is based on the radiation pattern.
At this point, we have calculated all the main parameters for a preliminary design of the patch antenna. The next step is to determine the definitive dimensions using the simulation software COMSOL to adjust the resonance frequency, and to improve the reflection coefficient at least below -18 dB (98,41 % efficiency).

3.3 Results from Numerical Simulations

Since we have already computed the main parameters of the patch antenna, we can numerically assess the behavior of this model. We are interested to evaluate the frequency response in the 2.45 GHz ISM band (2.4 GHz - 2.485 GHz). The results are presented by the scattering parameter S_{11} (it corresponds to the reflection coefficient ρ in the case of only one element) and the equivalent efficiency of transmission η.

3.3.1 Influence of the Patch Dimensions

From Figure 3.4 and 3.5 we can observe that the resonant frequency is shifted from 2.45 GHz by almost 60 MHz, and also the amplitude of the resonance is not below -14 dB. Now we have to determine the appropriate dimensions of the metallic patch to obtain better performance. First, we can change the

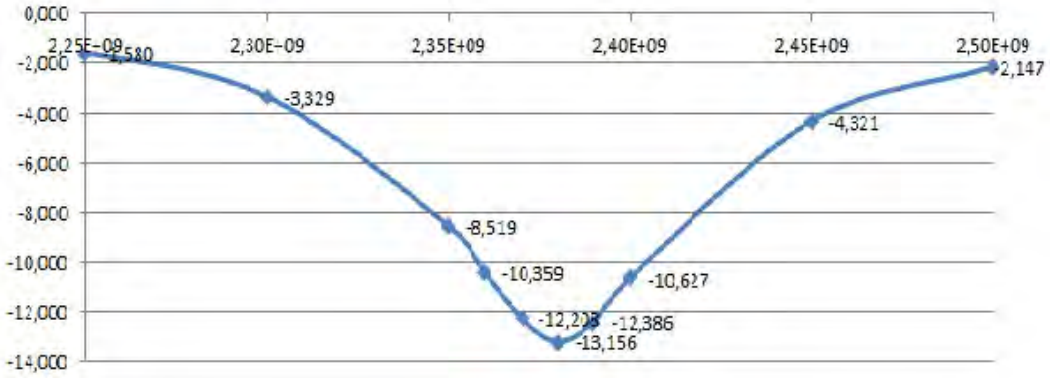

Figure 3.4: frequency response of the patch antenna: S_{11}

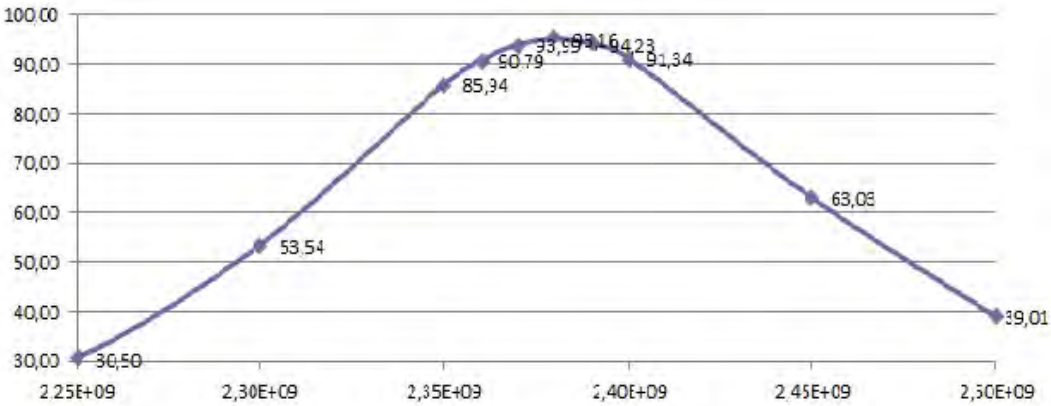

Figure 3.5: frequency response of the patch antenna: η

L_y size using a parametric analysis. In this analysis, five curves are depicted in a plot over the frequency domain, and each curve represents a specific L_y. In the current study, the following values are assumed: $L_y = 26.9mm$, $L_y = 27.0mm$, $L_y = 27.1mm$, $L_y = 27.2mm$ and $L_y = 27.3mm$. It should be noted that the main effect of the L_y variation is the shifting of the resonance frequency, while the peak value is not actually changed. The sensitivity of the variation can be estimated from the Figure 3.6, and we observe that there are $\Delta f \approx 5MHz$ and $\Delta S_{11} \approx 0$ dB) when $\Delta L_y = 0,1mm$.

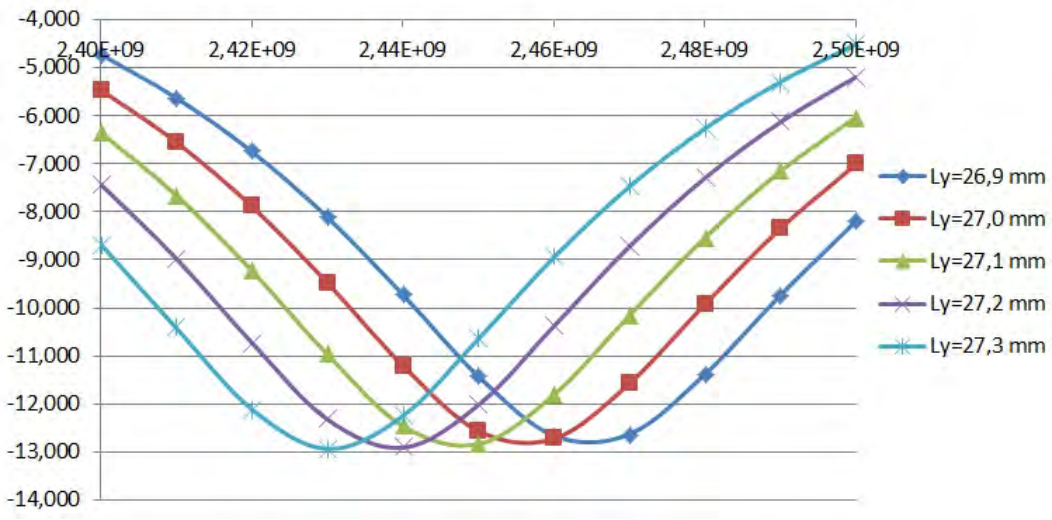

Figure 3.6: Variable parameter L_y with $L_x = 36.3mm$.

The same parametric analysis is done considering the L_x size. Again five parametric curves are plotted over the frequency domain. The values of L_x assumed are: $L_x = 34.3mm$, $L_x = 35.3mm$, $L_x = 36.3mm$, $L_x = 37.3mm$ and $L_x = 38.3mm$. In this case we obtain both the variation of the amplitude and the resonance frequency shifting. As we have done before, the sensitivity can be estimated by Figure 3.7, and we can state that there are $\Delta f \approx 1.5MHz$ and $\Delta S_{11} \approx 1$ dB) when $\Delta L_y = 1mm$. The sensitivities to the variation of L_y or L_x are different; in fact the step of the L_y parametrization is 0.1 mm, instead for the L_x parametrization the step was 1 mm. Therefore, there is actually one order of magnitude of difference between the size variation along the X and Y axes. This effect has to be considered during the construction phase because the required precision for L_y and L_x is different. The results depicted above are obtained with the position of the coaxial probe set to $y_{feed} = 8mm$ and $x_{feed} = 0mm$ (in the next paragraph the position of the probe is considered too).

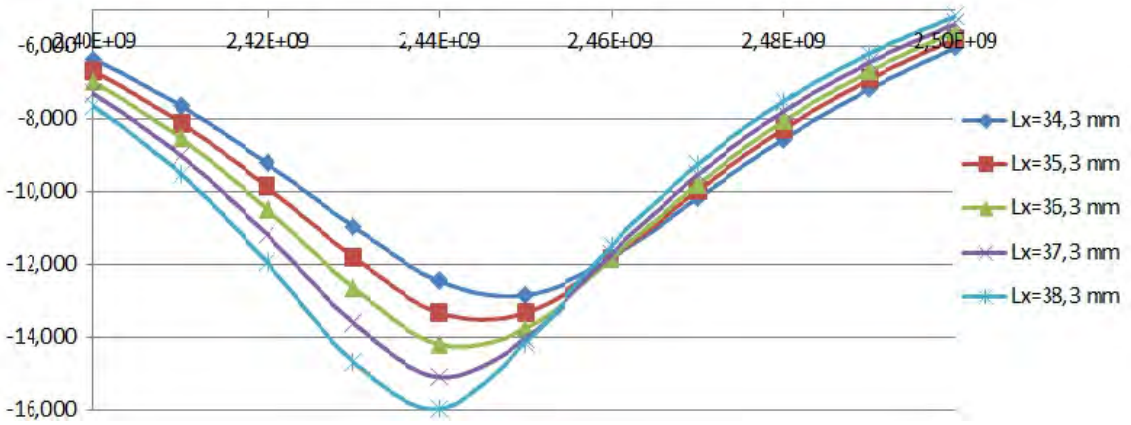

Figure 3.7: Variable parameter L_x with $L_y = 27.1mm$.

Based upon these observation we can derive an appropriate design procedure to obtain the definitive patch antenna:

- Preliminary dimensioning of the antenna using the formula from scientific literature.
- Variation of the L_y size through a parametric analysis (high sensitivity), centering the resonance frequency.
- Variation of the L_x size (low sensitivity), maximizing the amplitude of the resonance $\rightarrow L_x = 42.3mm$.
- Correction of the definitive value of $L_y \rightarrow L_y = 26.8mm$.
- Determination of the best position of the probe y_{feed} ,matching the device.

In the next paragraph the influence of the position of the probe is analyzed for different frequency, over the planar space of the patch. This represents the last step before to complete the design phase of the patch element.

3.3.2 Probe Position and Matching

Another important factor in the design of the antenna is the position of the coaxial cable. It is interesting to evaluate the effect of x_{feed} and y_{feed} on the radiation efficiency. A 3x3 matrix of positions (equally spaced) has been studied at 11 frequencies which belong to the range [2.4 GHz; 2.5 GHz]. Figure 3.8 shows the numbering of the different positions on the patch that

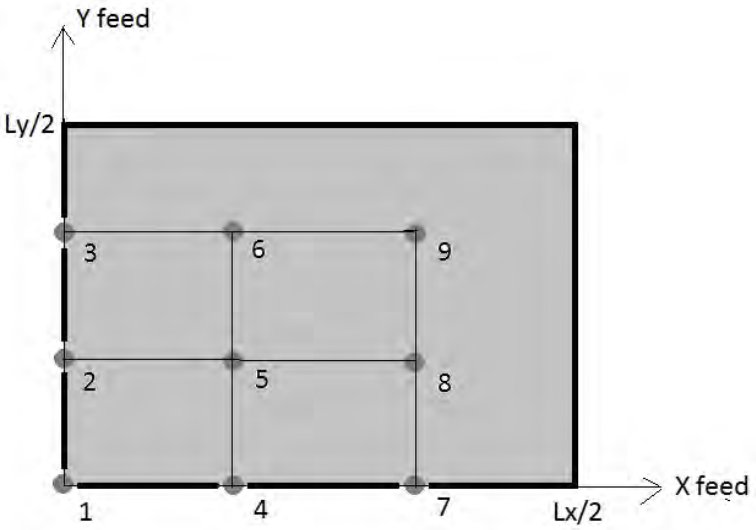

Figure 3.8: Position pattern of the coaxial cable.

are evaluated. The results of the analysis are plotted by 9 curves over the frequency domain in Figure 3.9. We can observe that the variation of the probe position along the X-axis is less effective than the variation along the Y-axis. This behavior is actually independent from the frequency, therefore the curves corresponding to position (1,4,7) are fairly close to each other. The same effect can be observed for positions (2,5,8) and (3,6,9). The next

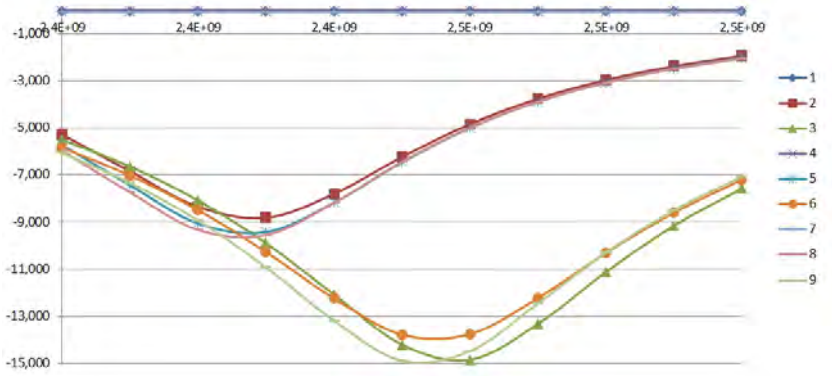

Figure 3.9: S_{11} parameterized by positions defined in Figure 3.8.

step would be to find the optimal position applying a parametric analysis but with more resolution on the space dimensions. Therefore, let's evaluate 10 positions along the Y axis (the area out from the main axes is not considered) at the same frequencies as before. This time, the curves are parameterized

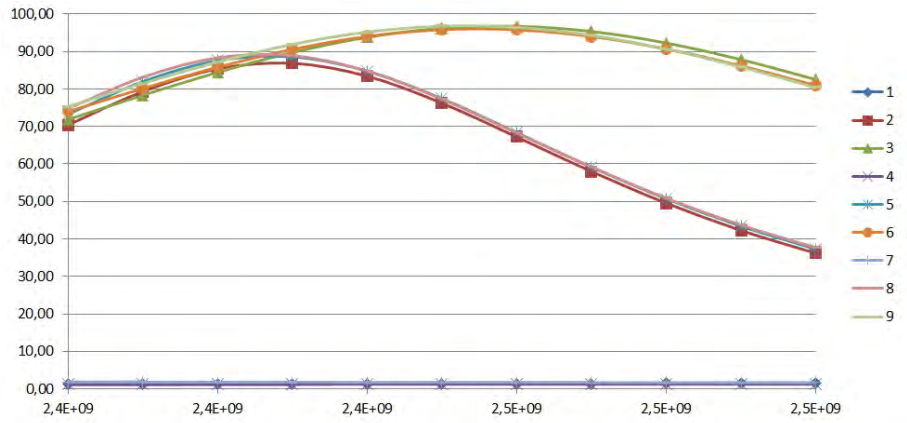

Figure 3.10: η parameterized by positions defined in Figure 3.8.

by the frequency and they are evaluated over the y_{feed} coordinate in Figure 3.11.

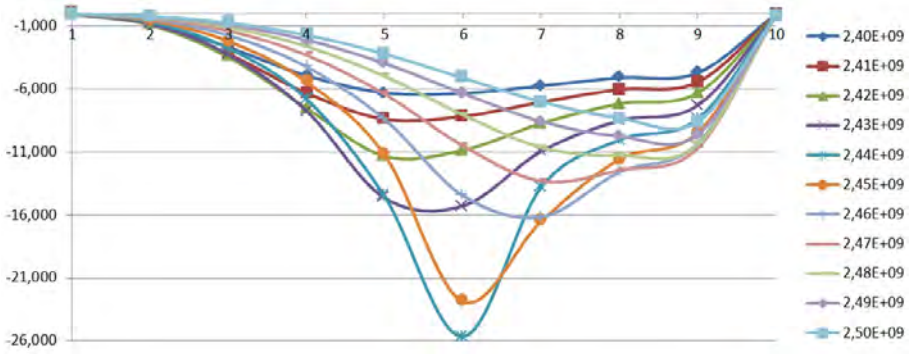

Figure 3.11: S_{11} over y_{feed}. $L_y = 26.8mm$ $L_x = 42.3mm$.

We should be able to observe that if we consider the curve in Figure (3.3.2), corresponding to the 2.45 GHz frequency, we have a resonance peak at the sixth position of y_{feed}. Therefore, we can deduce that an optimal solution could be obtained with $y_{feed} = (6/10)L_y/2 \approx 6mm$. Now we can repeat the same analysis but considering the X axis instead of the Y axis. From results we observe that all the curves are extremely close to each other, so the response of the probe position on the X-axis is actually independent from the frequency. An other important observation that has to be done is that the maximum value of efficiency is about 2.5% and that it is obtained close to the border of the patch. So, the improvement of radiation is actually negligible; also, it is not obtained by a suitable option in the construction

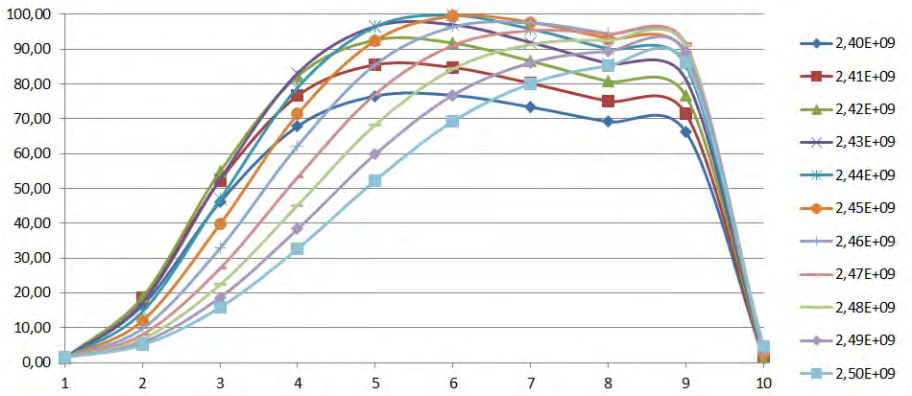

Figure 3.12: Radiation efficiency parametrized by frequency over y_{feed}, $x_{feed} = 0mm$.

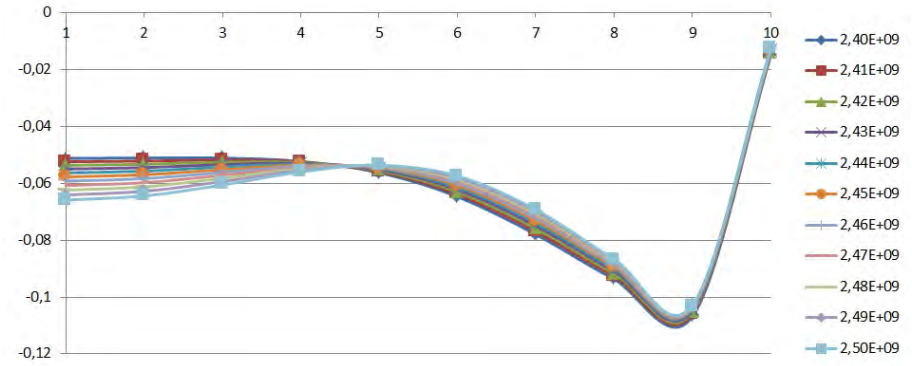

Figure 3.13: S_{11} parameterized by frequency over x_{feed}, $y_{feed} = 0mm$.

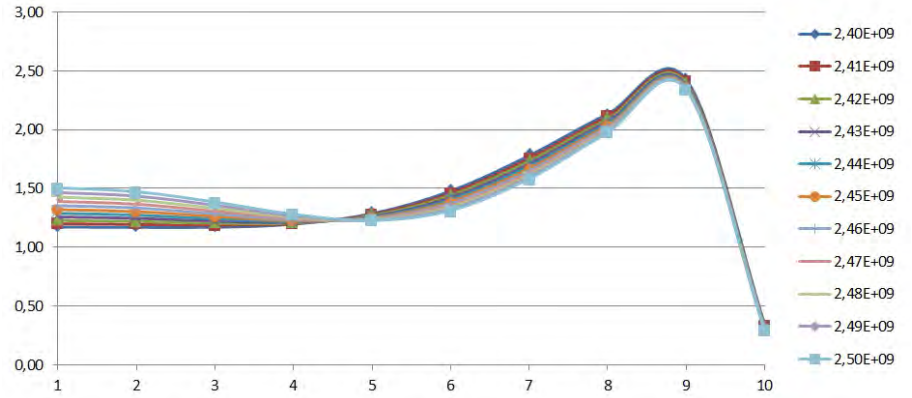

Figure 3.14: Radiation efficiency parameterized by frequency over x_{feed}, $y_{feed} = 0mm$.

phase. Since the central frequency of the band is 2.45 GHz, it is interesting to assess the same analysis with an high resolution along the entire area available on the patch. The analysis is done by a 10x10 matrix pattern of positions. The results have been exported to Matlab to apply a third order interpolation of the data to have a better view of the values obtained. Each value is characterized by a specific color as defined in the Figure 3.15.

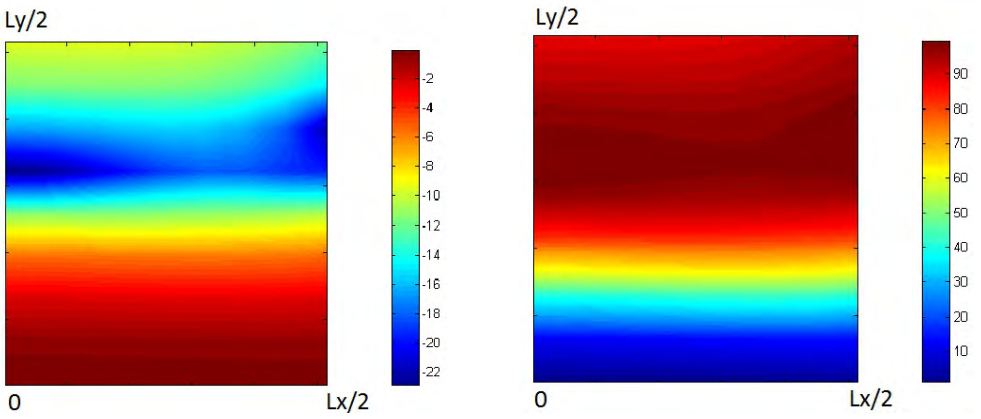

Figure 3.15: S_{11} and η for different probe positions over the patch area.

Now we can summarize the main results for an optimal probe positioning, that are found through all these parametric simulations:

- At the resonance condition the maximum peak along the Y axis is circa 98% instead the $2,5\%$ obtained along the X axis.
- The effect of changing x_{feed} is actually negligible with respect to the variation of $y_{feed} \rightarrow x_{feed} = 0$..
- The maximum value of radiation efficiency is found at about $y_{feed} = (6/10)L/2 \approx 6mm$ at the frequency 2.45 GHz.
- Along the borders of the patch and the X axis the efficiency is near zero.

When the radiation efficiency is almost 100%, the device is matched. Therefore, the probe position is defined in such a way that the characteristic impedance of the device at the electromagnetic port matches the characteristic impedance of the coaxial feeder.

$$Z_0 = 50\Omega \rightarrow S_{11} = \rho = 0 \rightarrow P_{reflected} = P_{input}|\rho|^2 = 0 \tag{3.9}$$

3.4 Mathematical Model of the Array

The array is composed of two elements which are positioned in a linear pattern. Now we desire to achieve a preliminary model of the array. Therefore we can study a simplified system that will be optimized by an optimization algorithm (OA). First, we define the main dimensions of the device and the current phases, then we'll apply the OA to obtain the actual phases of the feeders and to achieve the best radiation pattern. Only for a first simplified analysis we assume that the elements are equally spaced and equally phase shifted along each dimension (uniform array). Also, we consider the medium homogeneous and we assess the field in the far-field region that is defined by the Frahunhofer distance.

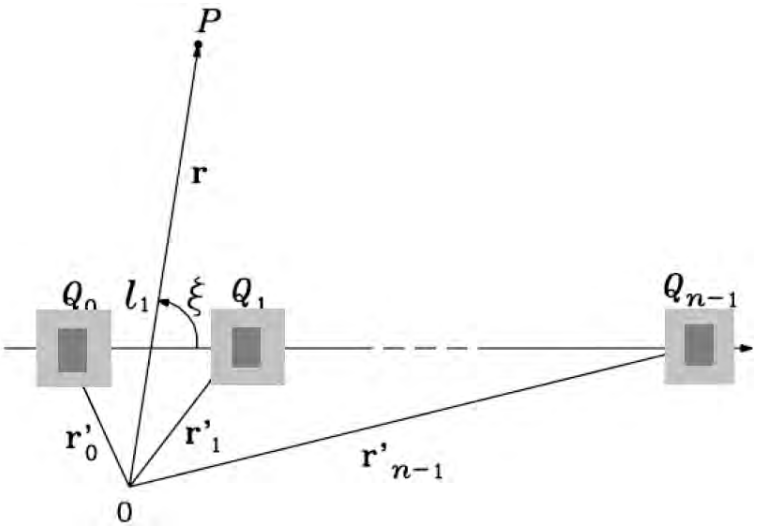

Figure 3.16: Representation of the patch antenna.

Let's introduce the following geometric and electric quantities to characterize the system:

- The current density at the h-element $\bar{J}(Q_h) = \bar{J}(Q_0)a_h$ where $a_h = a_0 e^{-jh\delta}$ with $h = 0, 1, ..., N-1$ and δ is the phase shift between two adjacent elements.

- The vector distance of the h-element $\vec{l_h} = h\vec{l}$ where $\vec{l}$ is the distance between two adjacent elements.

- The radius vector position of the h-element $\vec{r_h'}$ (the origin can be chosen arbitrary)

We can determine the equivalent moment of the array [2]

$$\bar{M} = \sum_{h=0}^{N-1} \int_{V_n} \bar{J}_0(Q_h) e^{jkr_h'\cdot r'} dV_n = \left(\sum_{h=0}^{N-1} a_h e^{jkl_h\cdot \hat{r}} \right) \int_{V_0} \bar{J}_0(Q_0) e^{jkr_0'\cdot r'} dV_0 \tag{3.10}$$

therefore we obtain $\bar{M} = \bar{F}\bar{M}_0$ where $\bar{M}_0$ is the moment of the single element (patch antenna). The term $\bar{F}$ is the *array factor*, and it can be semplified as follows

$$\begin{aligned} \bar{F} = \left(\sum_{h=0}^{N-1} a_h e^{jkl_h\cdot \hat{r}} \right) = \sum_{h=0}^{N-1} \left(e^{j\left(kl_h\cdot \hat{r}-\delta\right)^h} \right) = \sum_{h=0}^{N-1} q^h = \frac{1-q^n}{1-q} \\ = e^{j(N-1)v} \left(\frac{\sin(Nv)}{\sin(v)} \right) \end{aligned} \tag{3.11}$$

We have introduced the parameter v as follows

$$v = \frac{1}{2}\left(k\bar{l}\cdot \hat{r} - \delta\right) = \frac{\pi l}{\lambda}\cos\xi - \frac{\delta}{2} \tag{3.12}$$

Since we want only the total intensity of the field, we can neglect the complex array factor, and we consider only its magnitude. We obtain a symmetrical and periodical function with period π.

$$|F| = \left| \frac{\sin(Nv)}{\sin(v)} \right| \tag{3.13}$$

3.4.1 Project Requirements and Equivalent Conditions

The linear array is defined when we have set the following parameters: the distance l and the phase-shift δ between two adjacent elements, and also the number of elements N. We can determine them only when we have found some relations that allow us to satisfy the project requirements. Let's assume that we want the direction of the biggest factor ($|F|_{max} = N$) when $\xi_{max} = \xi_*$, the width of the main lobe $\Delta\xi = \Delta\xi_*$, and we don't want other main lobes. Let's evaluate the condition for the direction of the main lobe

$$|F|_{max} = \left| \frac{\sin(Nv)}{\sin(v)} \right|_{max} \rightarrow v = 0 \tag{3.14}$$

we can derive a condition for the phases

$$0 = \frac{\pi l}{\lambda}\cos\xi - \frac{\delta}{2} \tag{3.15}$$

$$\delta = \frac{2\pi l}{\lambda}\cos\xi \tag{3.16}$$

If we want to reduce the width of the main lobe, let's consider the angular positions where the field is reduced to zero

$$|F| = \left|\frac{\sin(Nv)}{\sin(v)}\right| = 0 \rightarrow v = \pm\frac{\pi}{N} \tag{3.17}$$

the left-limit is defined as follows

$$\frac{\pi l}{\lambda}\cos(\xi_-) - \frac{\delta_*}{2} = \frac{\pi}{N} \tag{3.18}$$

$$\xi_- = \cos^{-1}\left[\left(\frac{\pi}{N} + \frac{\delta_*}{2}\right)\frac{\lambda}{\pi l}\right] \tag{3.19}$$

in the same way for the right-limit

$$\frac{\pi l}{\lambda}\cos(\xi_+) - \frac{\delta_*}{2} = -\frac{\pi}{N} \tag{3.20}$$

$$\xi_+ = \cos^{-1}\left[\left(\frac{\pi}{N} - \frac{\delta_*}{2}\right)\frac{\lambda}{\pi l}\right] \tag{3.21}$$

we obtain the expression of the width

$$\Delta\xi = \xi_+ - \xi_- = \cos^{-1}\left[\left(\frac{\pi}{N} - \frac{\delta_*}{2}\right)\frac{\lambda}{\pi l}\right] - \cos^{-1}\left[\left(\frac{\pi}{N} + \frac{\delta_*}{2}\right)\frac{\lambda}{\pi l}\right] \tag{3.22}$$

The condition to have only one main lobe can be expressed if we impose that the relation $v = \pm\pi$ is obtained out of the range $0 \leq \xi \leq \pi$

$$\begin{cases} -\frac{\pi l}{\lambda} - \frac{\delta}{2} > -\pi \\ \frac{\pi l}{\lambda} - \frac{\delta}{2} < \pi \end{cases} \tag{3.23}$$

therefore we obtain

$$\frac{2\pi l}{\lambda} < 2\pi - |\delta| \tag{3.24}$$

$$l < \frac{\lambda}{|\cos(\xi)| + 1} \tag{3.25}$$

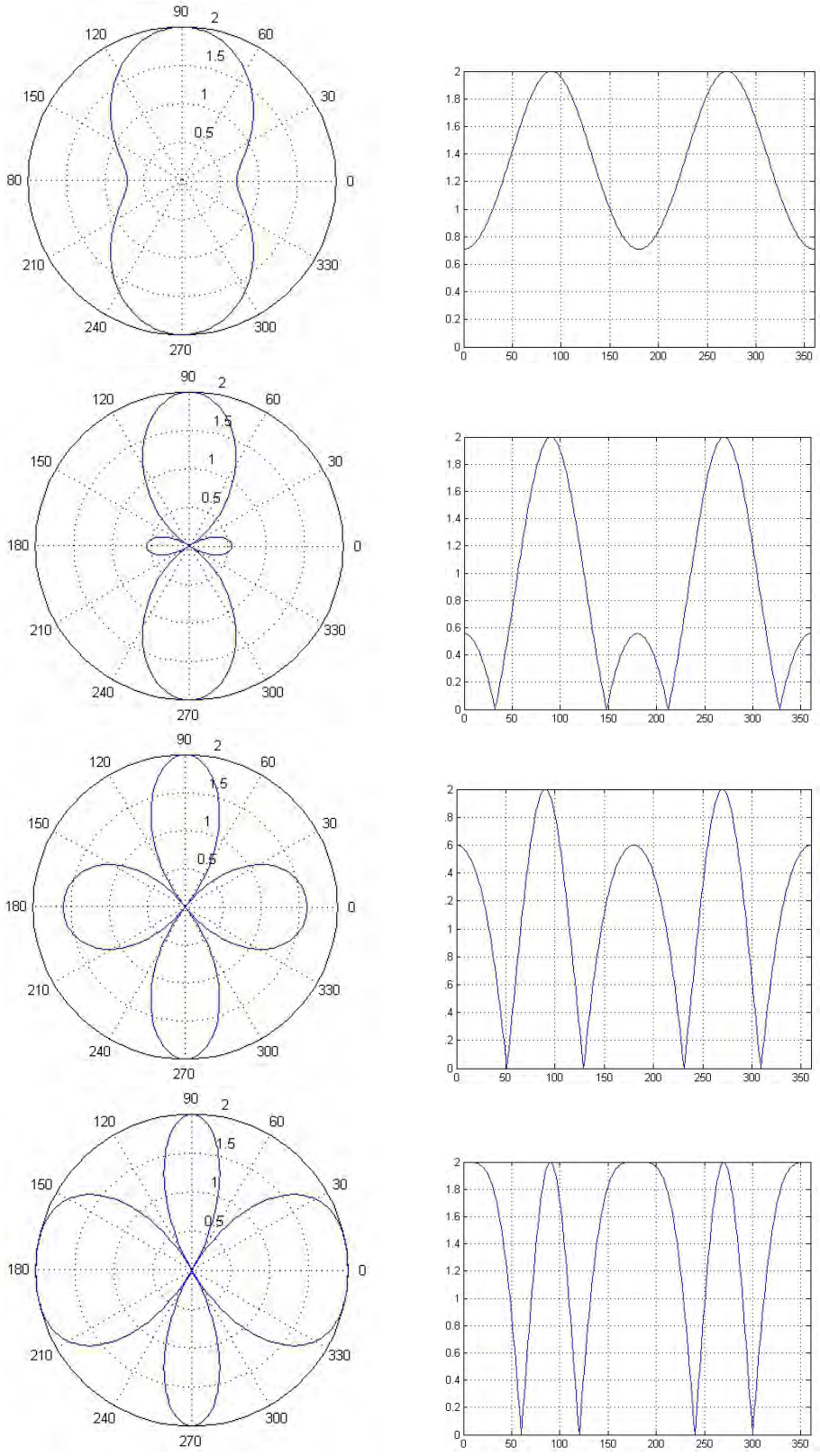

Figure 3.17: Radiation pattern varying the quantity d/λ.

The last equation represents the upper limit of the distance between two adjacent elements, when the condition of absence of other main lobes is required. So, using equations (3.16), (3.22), (3.25) we define the preliminary dimensioning of the array and the shift phase of the feeding currents. Implementing these equations in MATLAB, it's possible to evaluate the composition factor of the array in different cases. In Figure 3.17 there are four plots that represent the radiation patterns for a two element array. The operating frequency is 2.45 GHz and the distance between antennas varies from $d = L + 12h = 47,1mm$ to $L = L_{max}$ (value obtained by equation (3.25)). The direction of the main lobe is $\xi = 90°$ The purpose is to show the effect due to a variation of the distance between two adjacent elements. Also the following plots in Figure 3.18 indicate the appropriate number of elements N if the width of the main lobe is decided, and in the studied case we have set $\Delta\xi = 30°$.

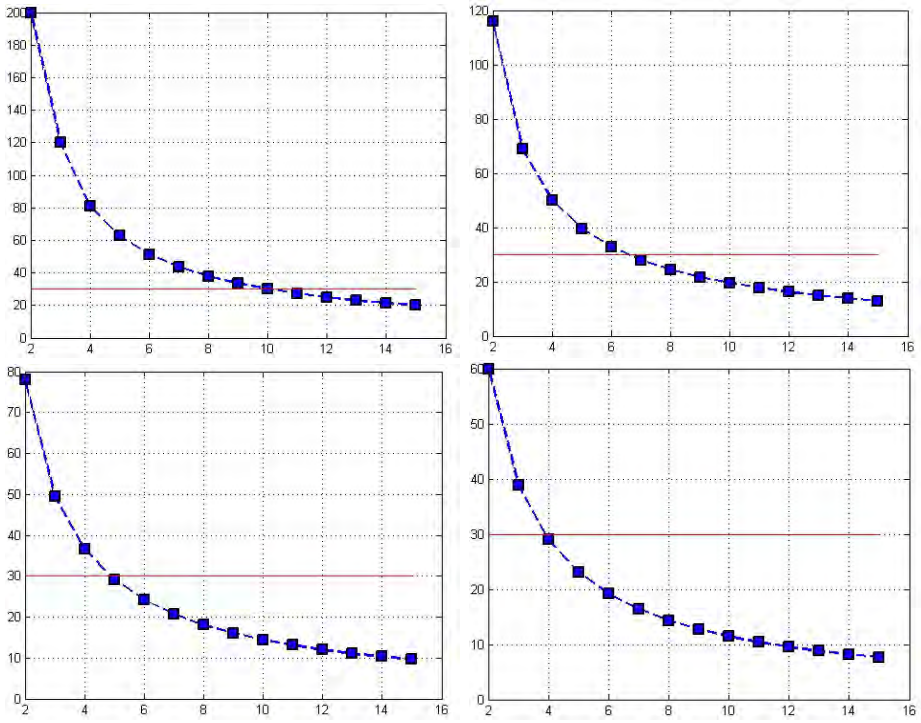

Figure 3.18: Number of elements of the array for a specified width of the main lobe with different d/λ.

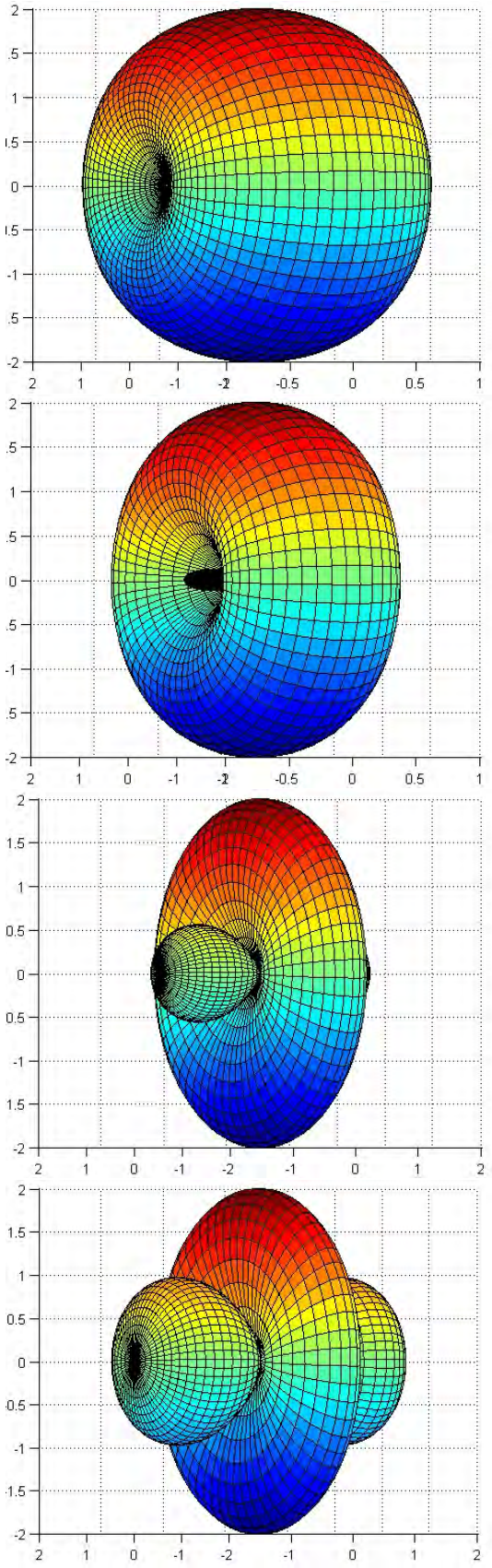

Figure 3.19: 3D composition factor of the array with different d/λ.

Chapter 4

Thermal Analysis: FD 1D Organic Model Response

4.1 High Frequency Heating

Microwave Heating is strictly dependent on the properties of dielectric materials and on the frequency of the applied electric field. In the next sections the physical phenomena that occur during the treatment will be considered.

4.1.1 Dielectric Polarization

The heating technique, based upon dielectric losses, derives from the ability of the field to polarize the charges in the material. The polarization cannot follow the alternating electric field rapidly, therefore its lag ensures a current density component in phase with the applied electric field. Also, the electrical conductivity can increase the power losses at lower frequency, so the combined effect can be estimated by the effective imaginary permittivity

$$\epsilon''_{eff} = \epsilon'' + \frac{\sigma}{\omega\epsilon} \tag{4.1}$$

If we consider the electromagnetic spectrum [100 KHz - 100 GHz] there are different physical phenomena that influence ϵ''_{eff}, and they can be classified as follows:

- *Electronic Polarization*: Electric deformation of electronic orbits due to the electric field. The atom actually behaves as an oriented dipole. Typical range $[10^{14}Hz - 10^{6}Hz]$.
- *Ionic Polarization*: The electric field induces a charge imbalance even in symmetrical molecules, therefore similarly to the electrical polarization, the atom behaves as a dipole. Typical range up to $10^{11}Hz$.

- *Dipolar Polarization*: All the substances that, in absence of external field, have a dipolar structure, when an electric field is applied, are oriented in the direction of the field lines. The rotation is opposed by mechanical friction.
- *Volume Polarization*: If inhomogeneous materials that contain watery inclusions are immersed in an electric field, then they withstand the displacement of electric charges. The inclusion becomes a polarized dipole due to the free charge separation in conductive medium (water).

Each of these polarization mechanisms has its bigger influence at specific frequencies of the alternating electric field. This dependence can be synthesized qualitatively in Figure 4.1.

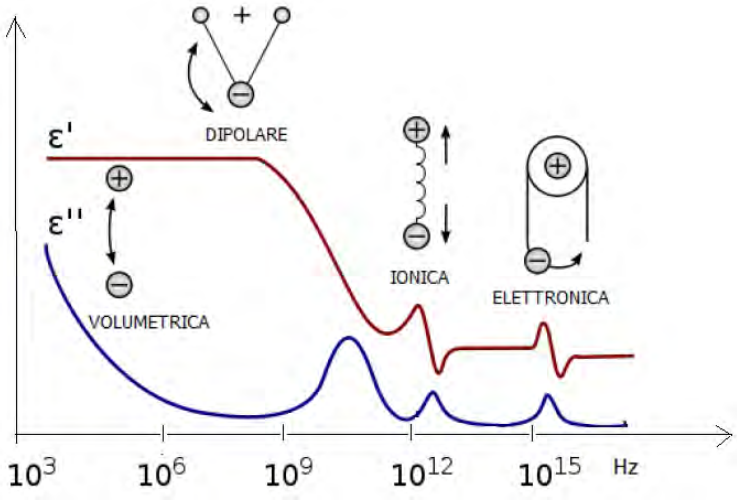

Figure 4.1: Real and imaginary dielectric permittivity over frequency.

4.1.2 Power Conversion and Heat Generation

Let's consider a material that is subjected to an alternating e.m. field, so we can express that average power by definition with the following equation :

$$P_{average} = \frac{1}{2}\int_{\Omega} Re\{\mathbf{E} \times \mathbf{H}^*\} \cdot \mathbf{n} d\Omega \tag{4.2}$$

So, in sinusoidal steady state, if we apply a few algebraic operations [12] we can arrive at:

$$P_{average} = \frac{1}{2}\omega\epsilon_0\epsilon''_{eff}\int_{\Omega} \mathbf{E} \cdot \mathbf{E}^* d\Omega = \omega\epsilon_0\epsilon''_{eff}E^2_{rms}V_{\Omega} \tag{4.3}$$

where E^2_{rms} is the medium root square value of the electric field (with the assumption of uniform field in the volume) and V_Ω is the volume of the considered material. It has to be noted that the converted heat is linearly proportional to ϵ''_{eff}, ω (so with the frequency), and V. On the other hand, $P_{average}$ is proportional to E_{rms} squared. Actually the dependence on E appears with the term $\epsilon''(E)$, even if here it is not explicit.

4.1.3 Penetration Depth

In our considerations in Chapter 1 the propagation of e.m. waves, we have described $E(z)$ and $H(z)$ as the sum of two forward and backward waves. Now we can re-elaborate the term α (attenuation constant) considering the polarization effect ϵ''_{eff} for a highly lossy medium ($\epsilon''_{eff} \gg \epsilon'$) [12]

$$\alpha_d = \omega\sqrt{\mu}\sqrt{\frac{\epsilon_0\epsilon''}{2}} \tag{4.4}$$

The preceding relationship shows that a lossy material behaves actually as a good conductor if we consider the attenuation constant, so we can define the equivalent penetration depth for dielectrics. The skin depth for a good conductor is defined as follows:

$$\delta_c = \sqrt{\frac{2}{\sigma\omega\mu}} \tag{4.5}$$

and if we substitute $\sigma = \omega\epsilon_0\epsilon''_{eff}$ the result is

$$\delta_c = \sqrt{\frac{2}{\epsilon_0\epsilon''_{eff}\sigma\omega^2\mu}} = \frac{1}{\alpha_d} \tag{4.6}$$

This parameter is extremely important when we have to select the operative frequency to heat the tumor. The higher the frequency is, the shallower the hyperthermia treatment. 2.45 GHz is suitable only for superficial tumors, therefore an other appropriate frequency has to be chosen if we want to treat deeper tumors. For instance, 915 MHz could be selected since it belongs to the available electromagnetic spectrum of the ISM band.

Another important phenomenon that has to be considered for the electromagnetic radiation, is the effect of the thermal load onto the radiating device. By changing the dielectric permittivity of the treated material (tissue), the wavelength and the frequency response of the system can be modified. In

Figure 4.2 there is the plot of S_{11} and η parametrized by different ϵ'. The values of the permittivity have been taken by the list of material properties used in Table 2.1, Chapter 2. The higher the permittivity is the higher the

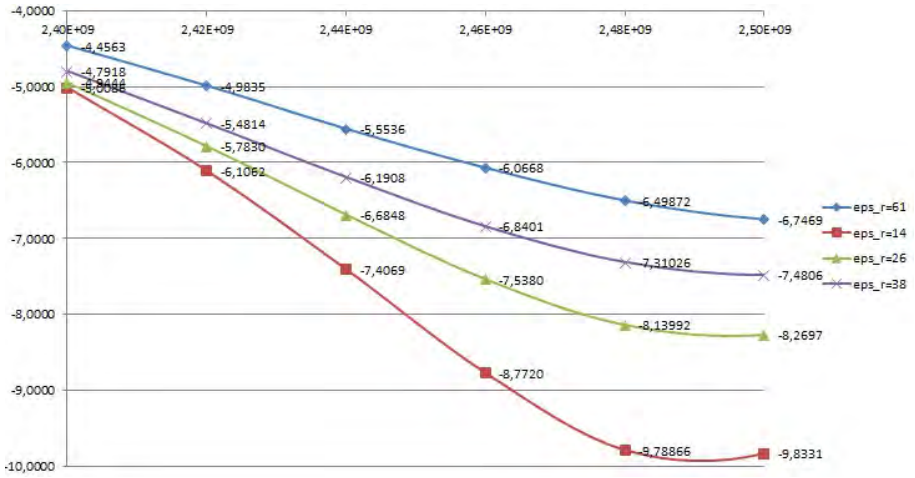

Figure 4.2: S_{11} of the device with different treated dielectric materials

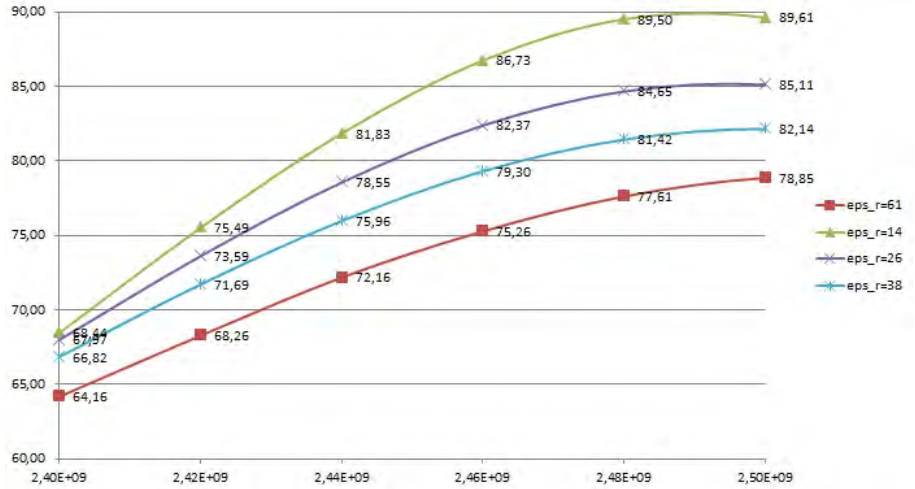

Figure 4.3: η of the device with different treated dielectric materials.

resonance frequency, and the lower the permittivity the higher the resonance amplitude (the resonance is close to the nominal design frequency at 2.45 GHz). This behavior can be observed by the numerical results in figure 4.2 and 4.3.

4.2 Finite Difference Model

In this section a transient mono-dimensional model has been implemented through the solution of parabolic second order differential equation. The mathematical aspects are considered in detail to obtain the algorithmic schema for Matlab implementation.

4.2.1 Resolution of Linear Second Order PDEs

Let's consider the following parabolic and linear partial differential equation with the unknown function $u(x,t)$:

$$\frac{\partial u(x,t)}{\partial t} = P(x,t)\frac{\partial^2 u(x,t)}{\partial x^2} + Q(x,t)\frac{\partial u(x,t)}{\partial x} + R(x,t)u(x,t) + S(x,t) \tag{4.7}$$

where $P(x,t), Q(x,t), R(x,t), S(x,t)$ are generic functions that depend on x (space variable) and t (time variable). The function $u(x,t)$ is defined in the interval $0 \leq x \leq L$ and it is subjected to the following boundary and initial conditions:

$$\begin{cases} u(x,0) = f(x) & 0 \leq x \leq L \\ \frac{\partial u(0,t)}{\partial x} = g_1(u) & t \geq 0 \\ u(L,t) = g_2(t) & t \geq 0 \end{cases} \tag{4.8}$$

The first equation represents the initial condition, and the second equation corresponds to the Neumann boundary condition, and the third equation is the Dirichlet boundary condition. The existence and uniqueness of the solution is guaranteed by the relations:

$$P(x,t) \geq 0 \tag{4.9}$$

$$R(x,t) \leq 0 \tag{4.10}$$

We can divide the x-domain in m nodes (m-1 elements) and the t-domain in z nodes (z-1 elements), and then we can consider the derivative as the incremental ratio between finite differences. For a generic t_n and x_i node we can use the different order derivatives as follows:

$$\frac{\partial u(x_i,t_n)}{\partial t} \approx \frac{u_{i,n+1} - u_{i,n}}{\Delta t} \tag{4.11}$$

$$\frac{\partial u(x_i,t_n)}{\partial x} \approx \frac{u_{i+1,n} - u_{i,n}}{\Delta x} \tag{4.12}$$

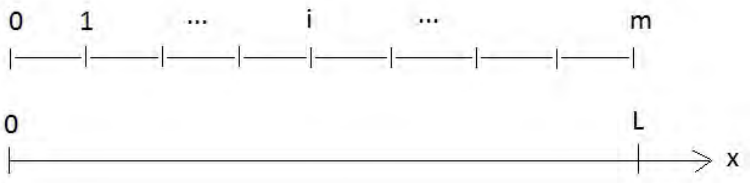

Figure 4.4: Discretization of the x-domain in m nodes (the same is applied for the t-domain).

$$\frac{\partial^2 u(x_i,t_n)}{\partial x^2} \approx \frac{u_{i+1,n} - 2u_{i,n} + u_{i-1,n}}{\Delta x^2} \tag{4.13}$$

If we substitute all the relations above into the equation (4.7) we obtain the following expression [13]:

$$\begin{aligned}\frac{u_{i,n+1}}{\Delta t} = P(x_i,t_n)\frac{u_{i+1,n} - 2u_{i,n} + u_{i-1,n}}{\Delta x^2} + Q(x_i,t_n)\frac{u_{i+1,n} - u_{i-1,n}}{2\Delta x} \\ + R(x_n,t_n)u_{i,n} + \Delta t S(x_i,t_n)\end{aligned} \tag{4.14}$$

Using equation (4.14) it's possible to compute all the values $u(x_i,t_n)$ starting from equations (4.8). In this way we have obtained a numerical formulation that can be implemented by a numerical code to derive the exact solution throughout the domain $(x \times t)$.

4.2.2 Formulation of Heat Transmission

The model presented in the last section, from a mathematical standpoint, is actually identical to the heat transfer model described by the Pennes equation. The convection heat exchange towards the environment at the first node has been considered, as well as fixed temperature at the last node (central position of bone). The power density source can be a generic function and it could depend on an electromagnetic model that can be coupled. Let us consider the equation (1.56)

$$\rho_t c_t \frac{\partial T}{\partial t} = \nabla \cdot (k \nabla T) + q_m + \omega \rho_b c_b (T_a - T) \tag{4.15}$$

If we consider an approximation as represented in the Figure 4.5, we can use a mono-dimensional space-domain. In the mono-dimensional case we derive

$$\rho_t c_t \frac{\partial T}{\partial t} = k_t \frac{\partial^2 T}{\partial x^2} + q_m + \omega \rho_b c_b (T_a - T) \tag{4.16}$$

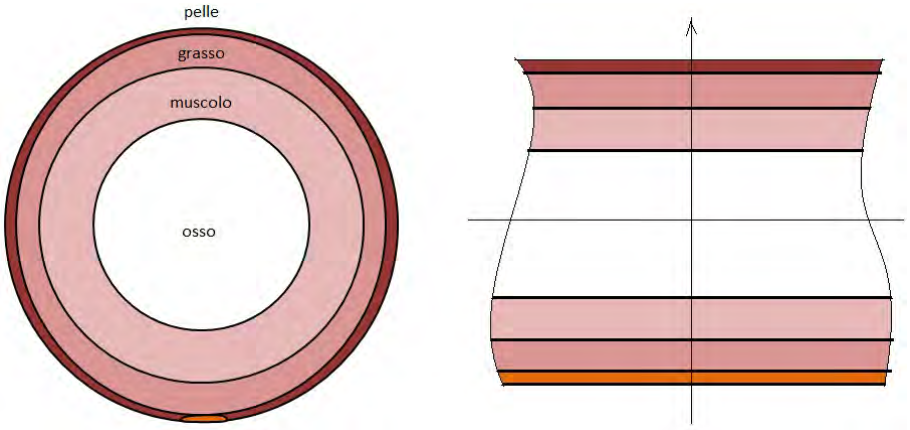

Figure 4.5: Approximation of the geometry into a mono-dimensional model.

and dividing by ρ_t, c_t

$$\frac{\partial T}{\partial t} = \left(\frac{k_t}{\rho_t c_t}\right)\frac{\partial^2 T}{\partial x^2} + \left(-\frac{\omega_t \rho_b c_b}{\rho_t c_t}\right)T + \left(\frac{q_m + \omega_t \rho_b c_b T_a}{\rho_t c_t}\right) \tag{4.17}$$

So, if we compare (4.14) with (4.17) we have the following correspondence

$$P(x) = \frac{k_t}{\rho_t c_t} \tag{4.18}$$

$$Q = 0 \tag{4.19}$$

$$R(x) = -\frac{\omega_t \rho_b c_b}{\rho_t c_t} \tag{4.20}$$

$$S(x,t) = \frac{q_m + \omega_t \rho_b c_b T_a}{\rho_t c_t} \tag{4.21}$$

and we can write as follows [1]:

$$\begin{aligned} T_{i,n+1} = T_{i,n} + P(x)\frac{\Delta t}{\Delta x^2}(T_{i+1,n} - 2Ti, n + T_{i-1,n}) \\ + R(x)\Delta t T_{i,n} + S(x_i, t_n)\Delta t \end{aligned} \tag{4.22}$$

[1] in a higher order model we should set $\omega = f(x,t)$ but in this way the PDE becomes non-linear and we should apply an iterative method to get a solution

The boundary condition that has been set on the first node is Newton's convection law, and at the last node a fixed temperature has been set:

$$h(T(0) - T_\infty) = k\frac{\partial T(0)}{\partial x} \tag{4.23}$$

$$T_m = T^* \tag{4.24}$$

The last two equations can be rewritten with the finite difference formulation

$$h(T_{1,n} - T_\infty) = \frac{k(T_{2,n+1} - T_{1,n+1})}{\Delta x} \tag{4.25}$$

and we can take out the term of the temperature at the time n+1

$$T_{1,n+1} = T_{2,n+1} + \frac{\Delta x h}{k}(T_\infty - T_{1,n}) \tag{4.26}$$

As the result of this schema we can implement the heat transfer model in

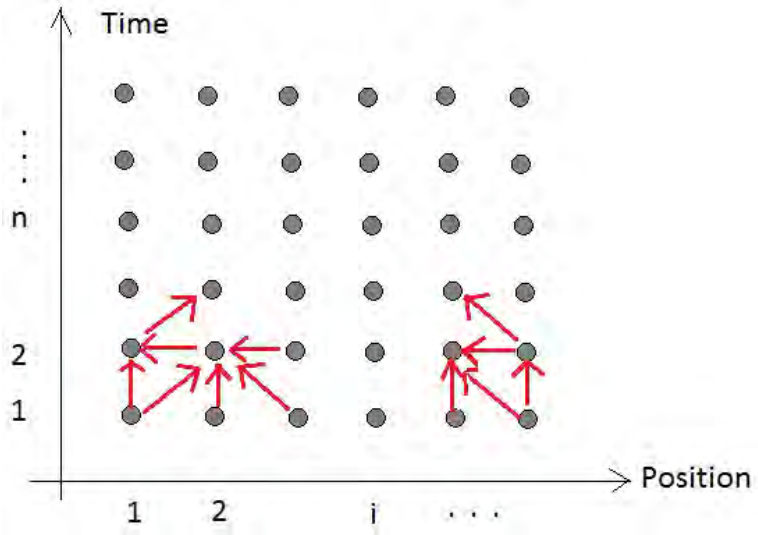

Figure 4.6: Schema of computation of the finite difference model.

Matlab with a time dependent power source in the tissues. The fixed values are $T^* = 33°$ (skin temperature in ordinary conditions), $h = 5[W/(mk)]$. The biological tissues have the properties listed in chapter 2, figure (2.2b). The distribution of thermal sources is plotted in the Figure 4.7, and in the Figure 4.8, 4.9, the temperature distributions have been presented:

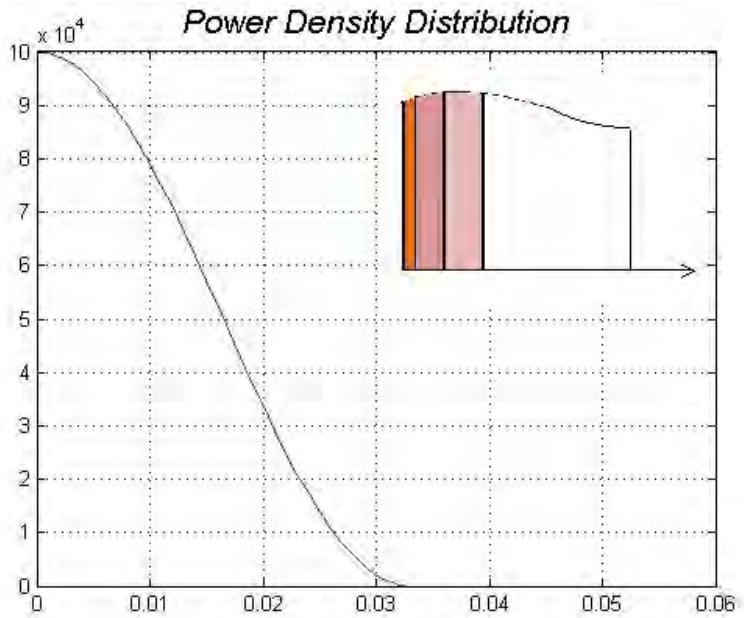

Figure 4.7: a) Temperature evolution with sinusoidal power density distribution.

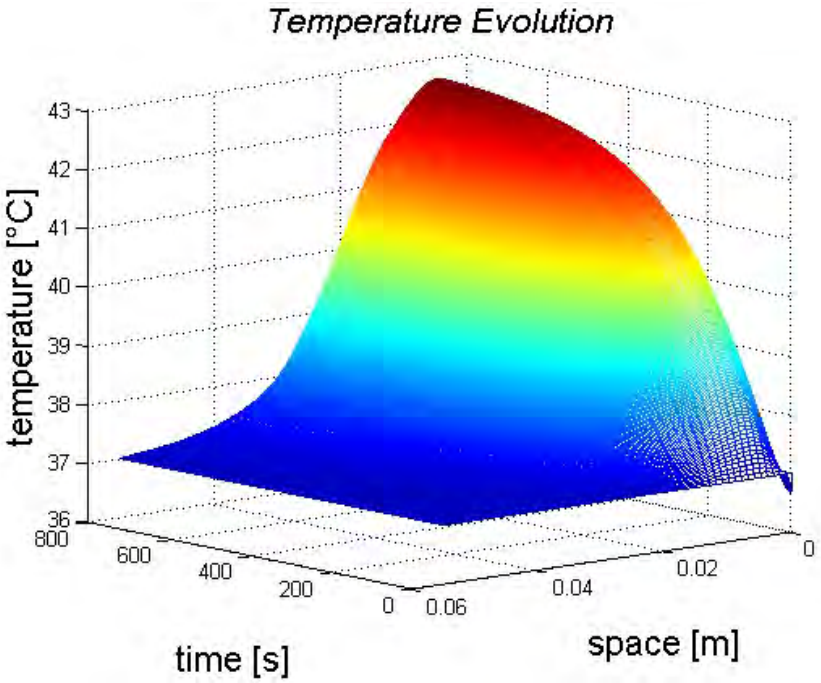

Figure 4.8: b) Temperature evolution with sinusoidal power density distribution.

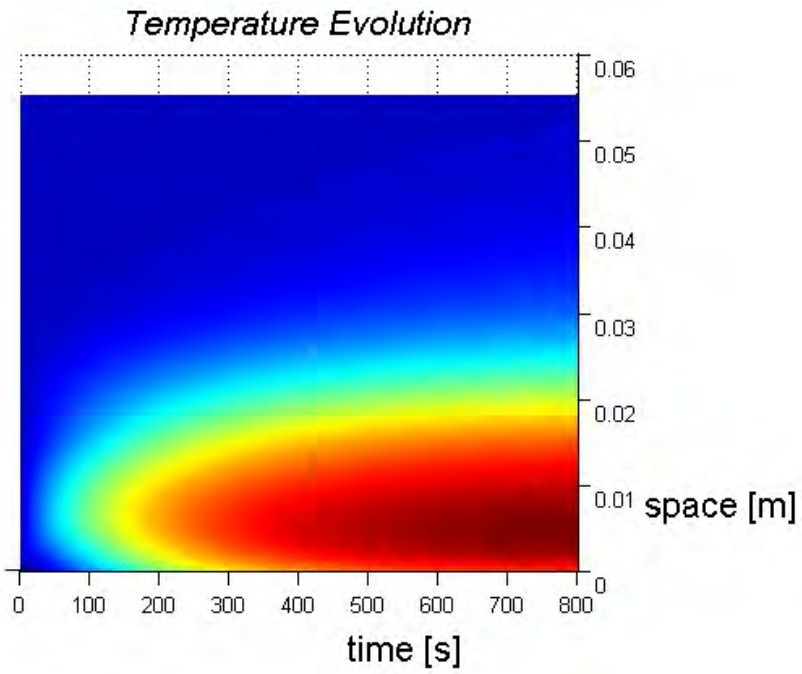

Figure 4.9: c) Temperature evolution with sinusoidal power density distribution.

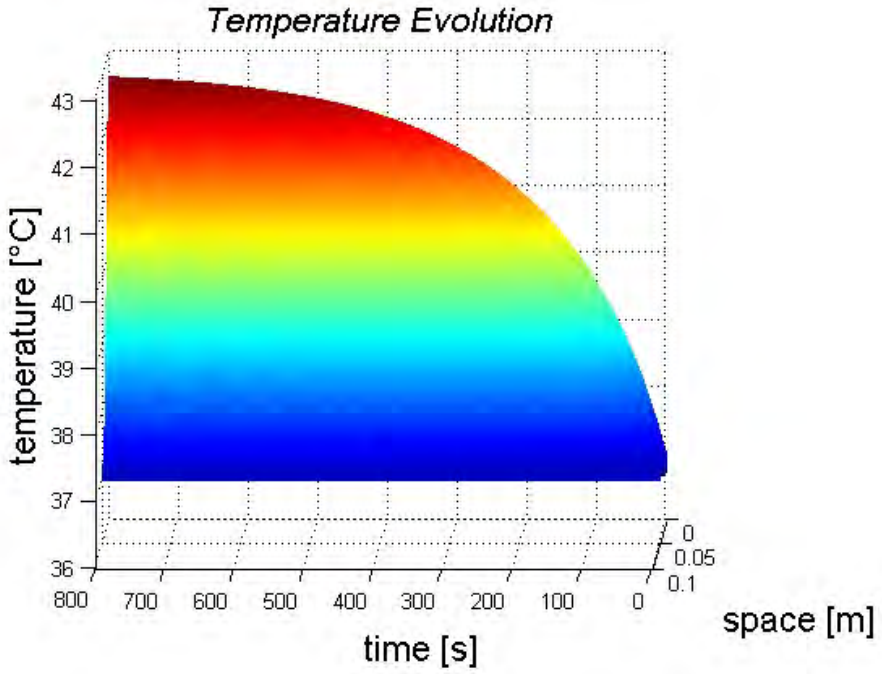

Figure 4.10: d) Temperature evolution with sinusoidal power density distribution.

4.2.3 Assessment of the Transient Evolution

The model that has been derived can be used to analyze the transient evolution of the temperature inside the different tissues. The distribution of the power density is very important to asses correctly the results, therefore we should know this function from an electromagnetic 3D model. In this way we can make into account the inhomogeneity of the materials and the actual heat sources generated by the device. Since we have already developed a FEM model[2], we can use the same distribution pattern of power that is obtained from the finite element analysis. Now let's consider a study case where the power input is constant over time. The aim of this analysis is to assess the required period to achieve the condition of steady state regime. Let us assume the power distribution pattern in Figure 4.11: The evolution

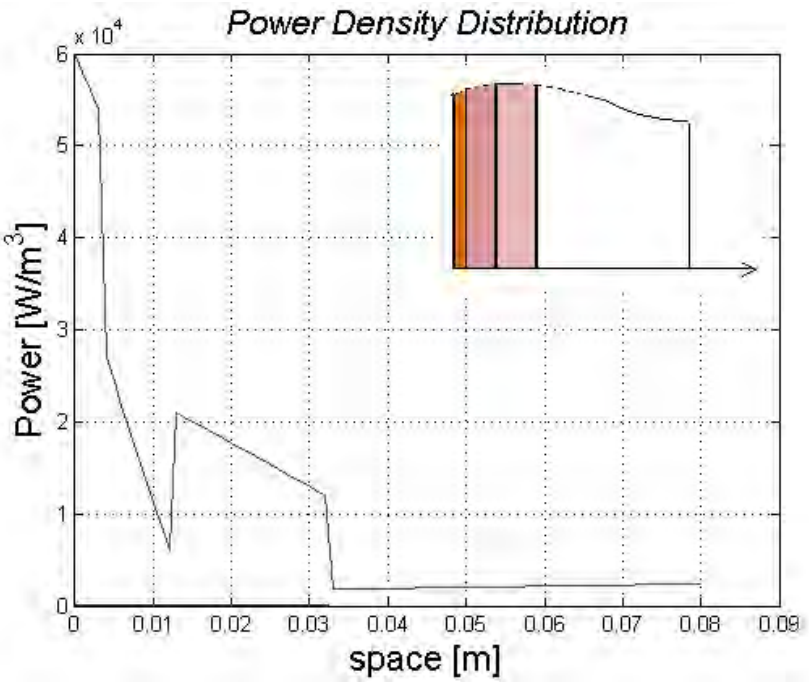

Figure 4.11: Inhomogeneous power density distribution.

of the system has been considered completely independent from any external control. The input power has its maximum at the skin/tumor level and it corresponds about to 60000$[W/m^3]$. At the tumor/fat interface there is a power discontinuity (step-down) and another one at the interface between fat and muscle. Also, there is the bone region with a low level of power density that is about 4000$[W/m^3]$. We can observe from Figure 4.12 that

[2]A detailed discussion of the results from the FEM model is made in the next sections.

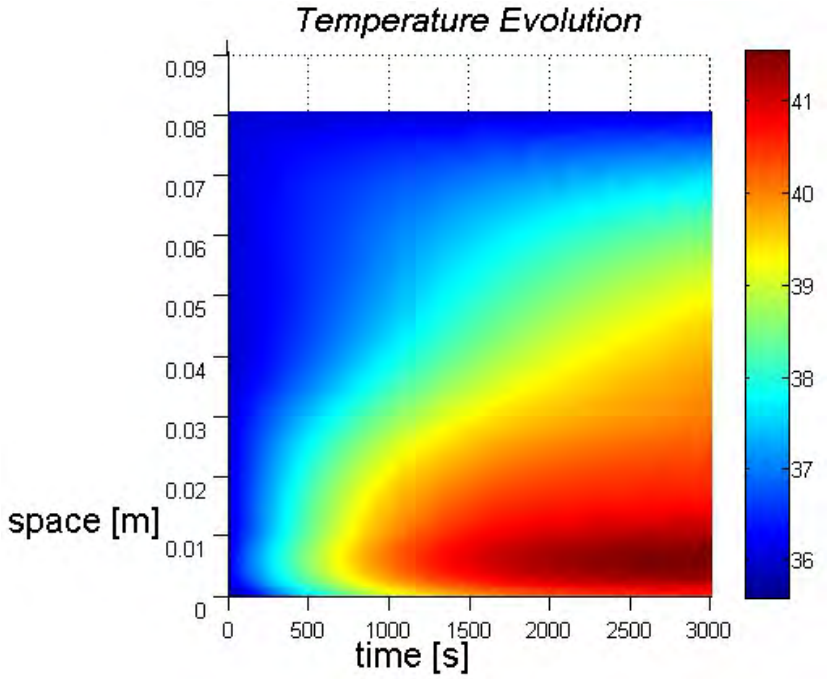

Figure 4.12: Temperature evolution with inhomogeneous distribution power.

the required period to achieve the steady state is about 3000 seconds (50 minutes). There is a transient evolution of temperatures that is not satisfactory for the clinical treatment because the therapy usually is not applied more than 20-30 minutes at the regime condition. To avoid this problem is necessary to boost the power density in the first 40 seconds, in such a way to reduce the transient period not over 2-3 minutes. We should note that the skin-air interface has a lower temperature than the central region of the tumor, and this is caused by the heat exchange toward the environment. The heat exchange is also increased by the treatment because the therapy is superficial. If we compare the Figure 4.9 and 4.12 we can observe how the temperature distribution over space is smoothed by the thermal conduction. Also, during the transient period there is an influence of the specific heat value at each tissue. Let's consider the distribution of the temperature over space in the Figure 4.13 that has been evaluated at different times. The peak amplitude is about 42°C. In Figure 4.14 we have described the growth of the average temperatures at each layer. It is important to note that the fat layer has the maximum temperature, so it is hotter than the tumor spot. This higher temperature is obtained even if the skin has a bigger amount of power sources, and this fact implies that we cannot control this undesired hot-spot only by controlling the focus of the electromagnetic field.

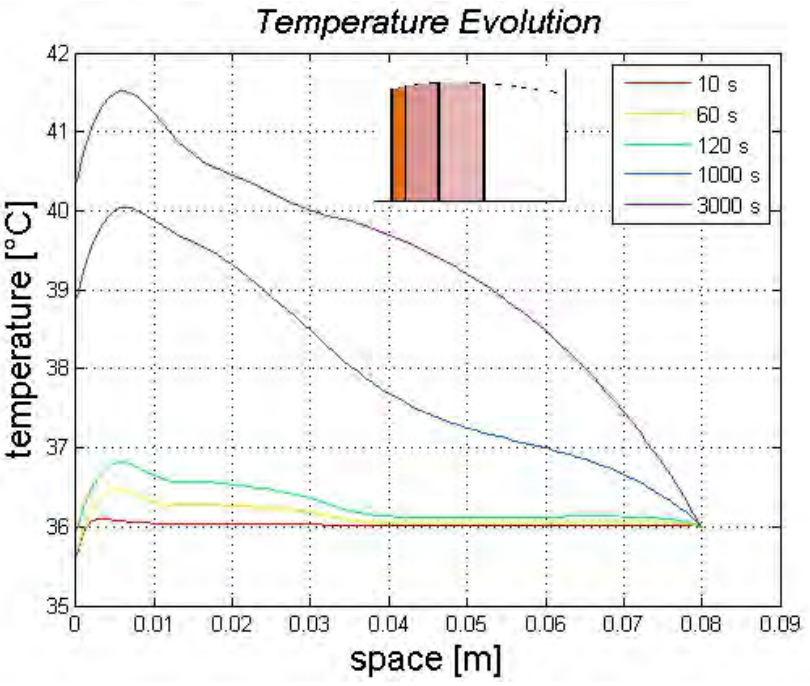

Figure 4.13: Temperature distribution with inhomogeneous power density distribution.

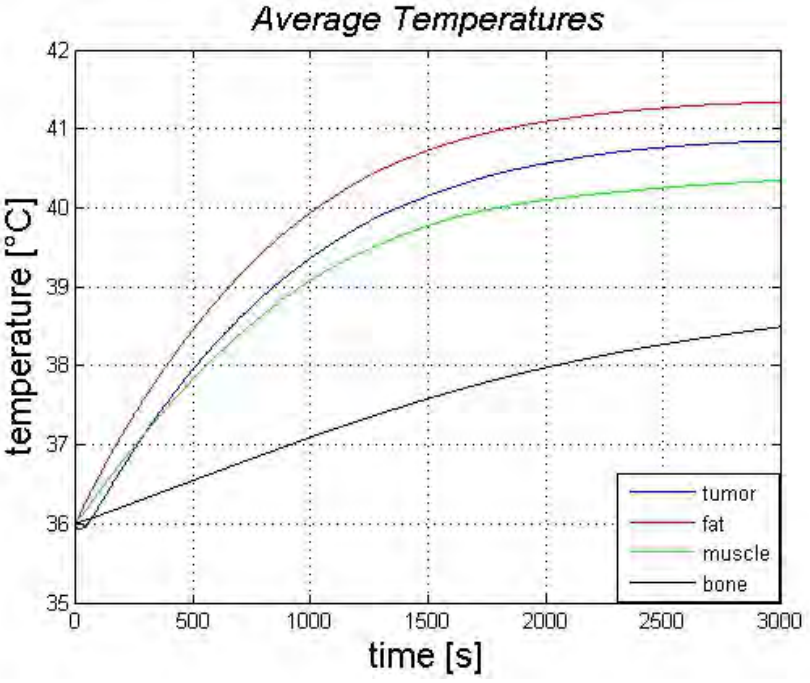

Figure 4.14: Average temperature in different tissues with inhomogeneous power density distribution.

As we have stated before, we have to boost for the first 40 seconds the power density, so we have defined a two-step power levels. The first level has a pattern density that is 8 times greater than the pattern in Figure 4.11, and the second level corresponds to six-tenth of the same pattern in Figure 4.11. In the following plots we consider only the first 120 seconds of evolution. The initial response of the system is actually linear because it is far from

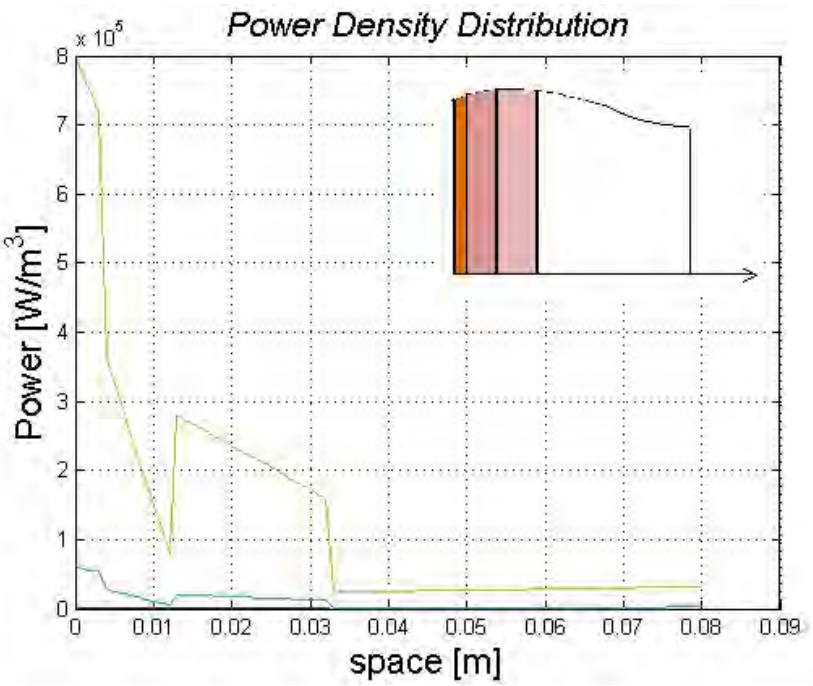

Figure 4.15: Inhomogeneous power density distribution with the initial boost.

the steady state condition. The Figures 4.16 and 4.17 show that the tumor achieves about the temperature 40°C after 40 seconds, and then it continues to increase slightly. Similarly to the preview case, the fat layer increases its temperature more than the tumor layer, and after 40 seconds it is over 42°C. In the current model the transient phase is much more acceptable for a clinical implementation, in fact after 3 minutes the steady state is already obtained. The shape of the curves presented in the Figure 4.16 is better than that one obtained in the Figure 4.13 because the bone has actually a normal temperature (between 36°C and 37°C). The results obtained so far induce us to implement in clinic at least a double power level set up. For the appropriate value of the power we need the temperature feedback from measurements.

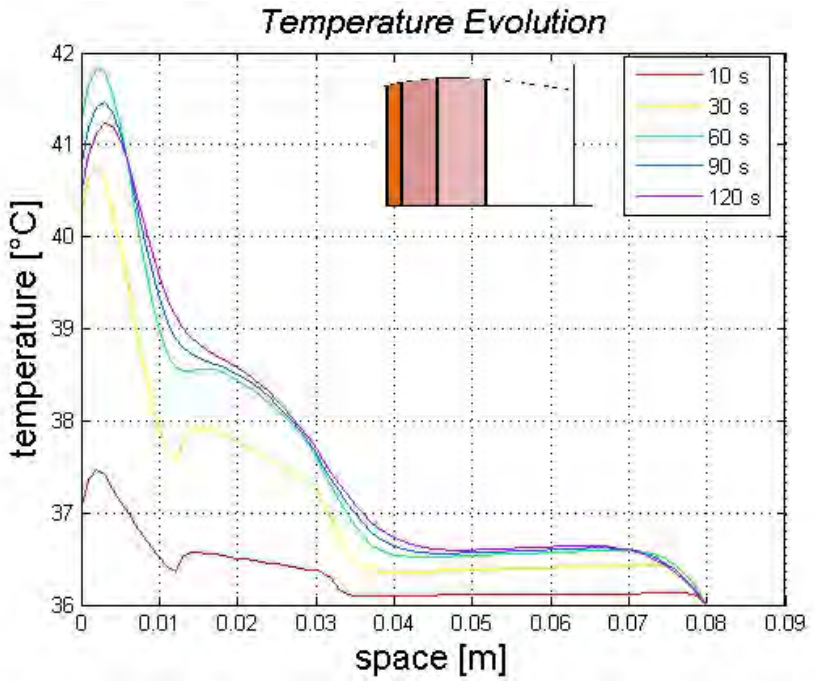

Figure 4.16: Temperature distribution with initial boosted power.

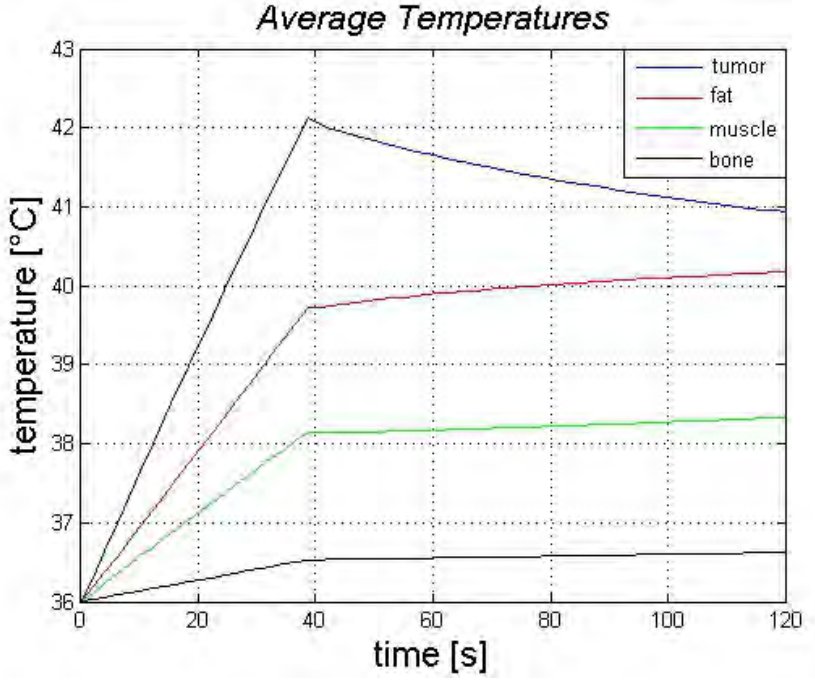

Figure 4.17: Average temperature in different tissues with initial boosted power.

The initial power level has to be defined considering both the reduction of transient state and the amplitude of initial hot spots. To evaluate this phenomenon, we can apply a parametric analysis for the initial power level. Five cases have been studied, so we have set the initial distribution pattern 6 x, 7 x, 8 x, 9 x, and 10 x the pattern in Figure 4.11. The numerical evaluation has been done referring to the average temperature in the tumor. The results are plotted in Figure 4.18. We can observe that for every case,

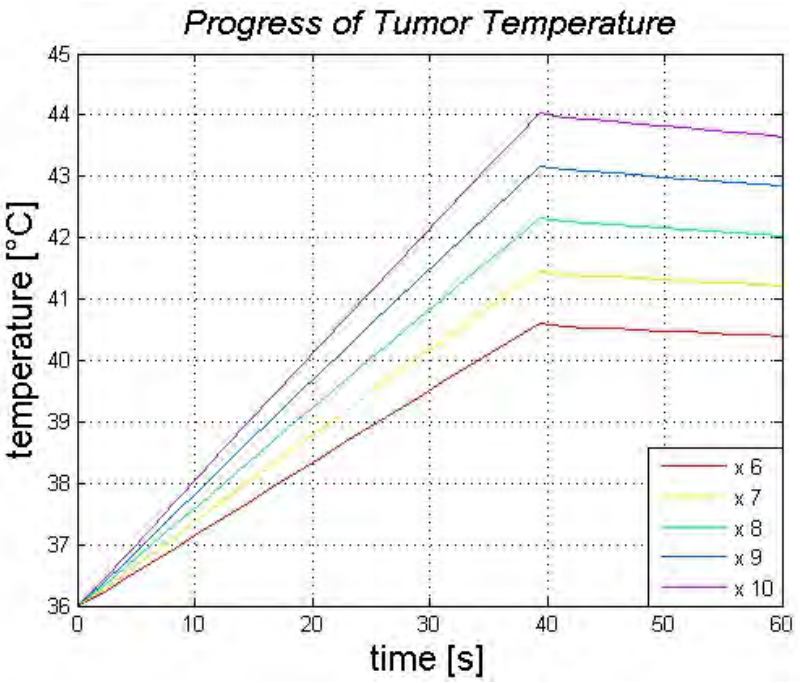

Figure 4.18: Transient temperatures with different initial boosted powers.

during the first 40 seconds, the growth is linear because we are far from the thermal equilibrium. The evolution with power 10 x with respect to the case in Figure 4.11 is not suitable for the treatment, since the tumor temperature overcomes the target value 43°.

Another interesting evaluation can be done if we consider a pulsed power treatment. For the first 40 seconds we can boost the power injected into system, then we feed the device with a pulsed power, in order to maintain the tumor temperature below 43°C and over 40°C [3].

[3]This kind of treatment can be obtained through an automatic control

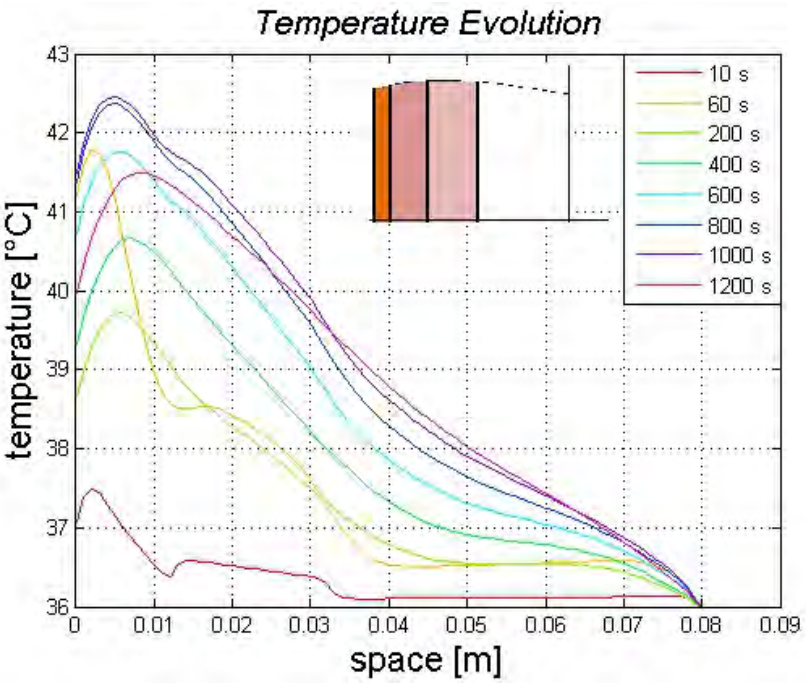

Figure 4.19: Temperature distribution with pulsed power control.

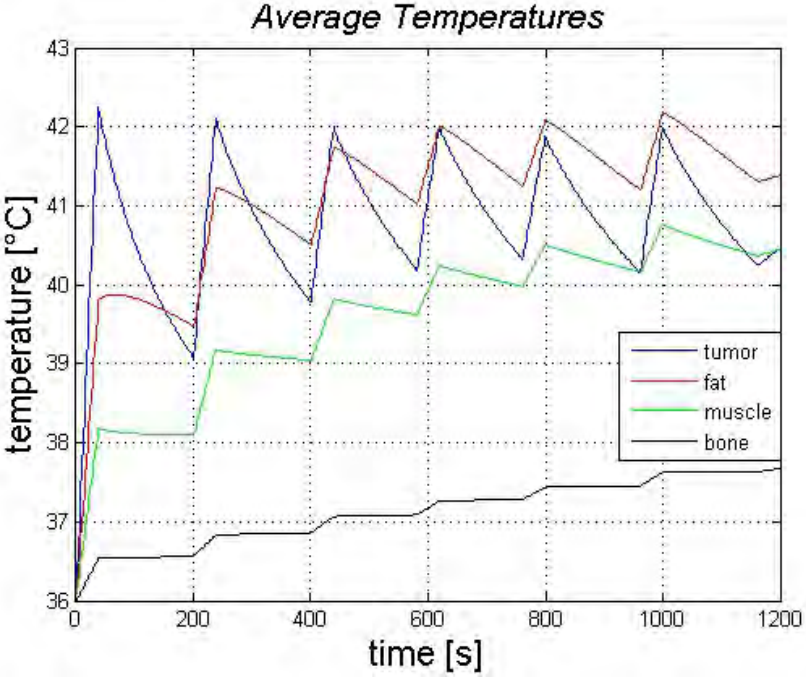

Figure 4.20: Average temperature in different tissues with pulsed power.

We observe in Figure 4.19 that the temperature distribution tends to spread across the layers adjacent to the tumor. Also, from Figure 4.20 we should note that the pulsed power allows the tissues to decrease their temperature, but unfortunately the tumor has a smaller time constant than the constants of remaining tissues. This phenomenon is due to the strong effect of the convective heat exchange toward the environment for the skin-tumor. The main consequence is that the focused heating can be obtained only for a transient period, but the longer the treatment and the more uniform is the temperature. The evolution of the system temperature is represented in Figure 4.21.

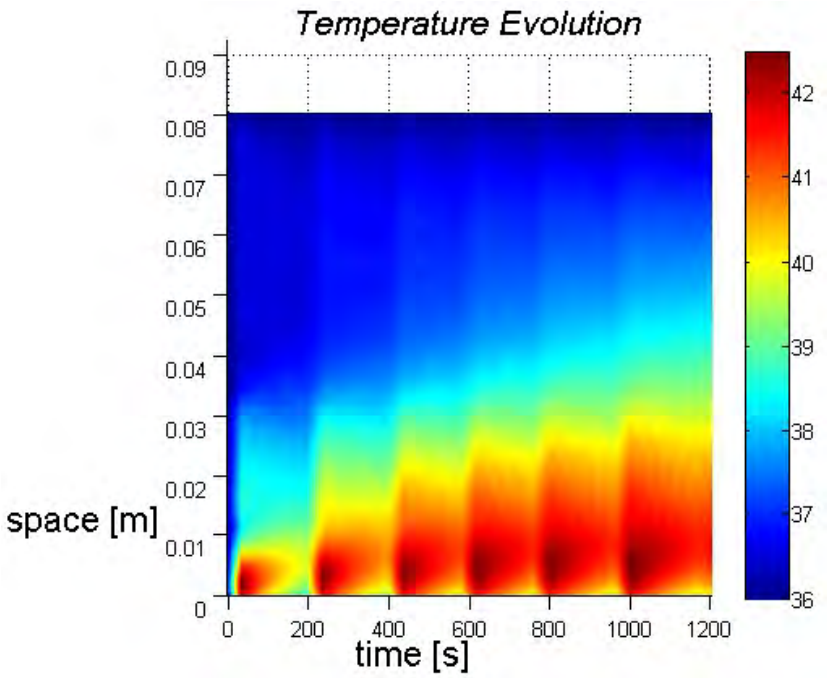

Figure 4.21: Temperature evolution with pulsed power control.

Chapter 5

Thermal Analysis: FEM 3D Organic Model Response

In the previous chapter, the development of a finite difference model was described in detail. In this section we will consider the results from a numerical FEM analysis. The great difference between the two analytical approaches is due to the considerable disparity of the computational hardware requirements. The complexity and accuracy that can be obtained using FEM CADs is unattainable applying the model considered and developed in chapter 4 [1]. The higher the precision of the results, the longer the required computational period. Since we are dealing with the interaction between an electromagnetic radiating device and a human body, it is necessary to obtain the maximum precision for the achievement of the best treatment quality.

5.1 Parametric Analyses

During the treatment there are certain parameters that can be controlled. The most important of them are: the distance between the patient and the device d, the distance between the two patch antennas p (considering the barycenters), the phase-shift between the feeding currents $\Delta\phi$ and the power per antenna P. The purpose of the following sections is to describe the thermal response of the human body when these settings are changed. The best way to study the impact of each parameter is performing a parametric analysis. The initial set-up of each simulation is described in Table 5.1.

The results are evaluated by the maximum temperature in the entire organic volume subjected to hyperthermia, by the the specific absorbed rate

[1] An interesting study could be made comparing 3D FD and FEM Multi physics CADs, studying a benchmark model (But this subject is out of the purpose of the current study).

Variable Parameter	d $[mm]$	$\Delta\phi$ $[deg]$	p $[mm]$	P $[W]$
d	[5-40]	0	46	4
$\Delta\phi$	30	[0-360]	46	4
p	30	0	[49-96]	4
P	30	0	46	[2-6]

Table 5.1: Electromagnetic and thermal properties of the materials used in the model.

in the tumor, and by the above average specific absorbed rate in all the tissues. The ratio between the last two parameters can be considered as the ability to confine the heating in selected regions without damaging healthy tissues. The representation of the cross section temperature and local SAR for the most significant cases will be presented, in order to have a better understanding of the physical phenomena that are involved. All the results that have been derived in this section are computed with the assumption of the achievement of thermal equilibrium. So, we are considering only the thermal steady state condition. In sections 5.3 and 5.4 the time-dependent analysis will be performed.

5.1.1 Distance between the Patient and the Array

Before assessing the FEM numerical results, let's consider a simplified model of propagation. The simplest antenna model is the oscillating Hertzian dipole. Due to the simplicity of this model we can derive an approximated analytical dependence between the electric field amplitude and the distance between source and the observation point. The dipole has an infinitesimal length dl, current I, angular frequency ω, and wave constant k. The radiated electric field has the following components (solution derivable from the maxwell equation) [14]

$$\begin{cases} E_r = \frac{Idl}{2\pi\omega\epsilon}\cos\theta\left(\frac{k}{d^2}-\frac{j}{d^2}\right)e^{-jkd} \\ E_\theta = \frac{Idl}{4\pi\omega\epsilon}\sin\theta\left(\frac{jk^2}{d}+\frac{k}{d^2}+\frac{j}{d^3}\right)e^{-jkd} \\ E_\phi = 0 \end{cases} \tag{5.1}$$

let's consider the magnetic field components:

$$\begin{cases} H_r = 0 \\ H_\theta = 0 \\ H_\phi = \frac{Idl}{4\pi}\sin\theta\left(\frac{jk}{d}+\frac{1}{d^2}\right)e^{-jkd} \end{cases} \tag{5.2}$$

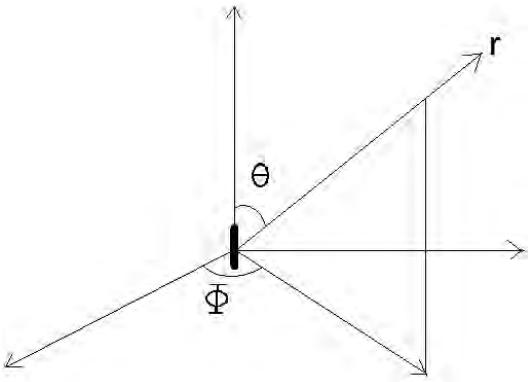

Figure 5.1: Representation of the Hertzian dipole.

Using these equations we obtain:

$$P_{active} = \frac{1}{2} Re\left[\mathbf{E} \times \mathbf{H}^*\right] = f\left(\frac{1}{d^2}\right) \tag{5.3}$$

The electromagnetic transmitted power decreases proportionally to $1/d^2$. So, if we consider small variations of the distance we have big variations of the transferred power. We should remember the limits of the analytical model that are due to the assumption that the source is an elementary dipole, the omission of the higher order infinitesimal terms. Also, the hypothesis of an absence of the load changes the characteristics of the propagation. The numerical results are presented in Table 5.2 and the temperature distributions in Figure 5.1.

d $[mm]$	T_{max} $[degC]$	SAR_{tumor} $[W/kg]$	SAR_{total} $[W/kg]$
5.0	47.0	88.52	2.49
10.8	45.1	78.39	2.51
16.7	44.0	64.80	2.32
22.5	42.6	52.03	2.12
28.3	41.5	42.20	1.91
34.2	40.6	35.21	1.72
40.0	40.1	30.56	1.53

Table 5.2: Results of the FEM model depending on d.

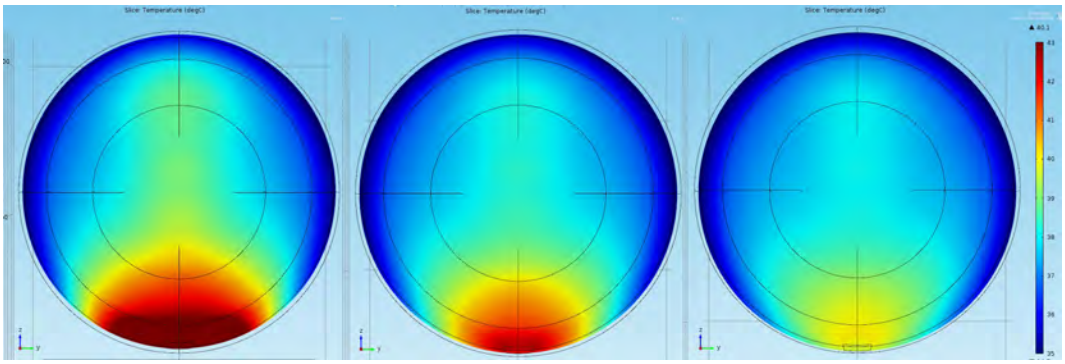

Figure 5.2: Cross-section temperature distributions with d=5 mm, d=22.5 mm, d=40 mm.

5.1.2 Phase-shift of the Feeding Currents

The phase-shift $\Delta\phi$ is one of the most controllable parameters during the hyperthermia treatment. Many experimental studies have shown the possibility to focus the heating in deep regions based on an adaptive phase controller algorithm [15]. When we change $\Delta\phi$, we are actually modifying the superposition of the radiated fields. In fact, if $\Delta\phi = 0$, on the middle plane Q perpendicular to the alignment axis, all the field components are summed in phase. Instead, when we set $\Delta\phi = \pi$ we obtain the opposite condition and the field magnitudes are subtracted. In the case of two patch antennas uniform array, without any numerical computation, we know that in the first case the magnitude of the electric field is doubled; however, in the second case the magnitude of the field is zero [2] . Also, if the phase shift is zero, in the middle plane Q the components, polarized perpendicularly with respect to the same Q, cancel each other out. This behavior is actually identical to the one induced by a perfect magnetic wall placed on Q. In this case there is implicitly the condition of the Dirichlet boundary for the magnetic vector potential. On the other hand, when we set $\Delta\phi = \pi$ the field components polarized on Q cancel each other out, and so this physical behavior is the same as that which occurs in the case of a perfect electric conductor. We could replace Q with a metallic sheet. If we consider the far-field region we can easily control the main lobe direction by changing $\Delta\phi$. Telecommunication systems use this technique to direct the electromagnetic field in a certain direction where receiving antennas are placed. Furthermore, when $\Delta\phi = 0$ we obtain a broadside antenna, so the main lobe is perpendicular to the align-

[2]These considerations are valid since the propagation of the electromagnetic field is symmetrical with respect to a plane that divides the antenna along X_f, Y_f axes.

ment axis. In contrast, $\Delta\phi = \pi$ allows us to obtain an on-fire antenna which is able to radiate the main lobe along the alignment axis. In addition, we must consider that the width of the main lobe changes, varying $\Delta\phi$. After all these considerations, since we are dealing with the near-field region, only the FEM model can actually show if there are other side-effects by changing $\Delta\phi$. Observing Figure 5.3 we note that the direction of the main lobe is actually rotating, and similarly way that would occur in the case of far-field propagation. All the results are presented in Table 5.3 and the temperature distributions in Figure 5.3.

$\Delta\phi$ $[deg]$	T_{max} $[degC]$	SAR_{tumor} $[W/kg]$	SAR_{total} $[W/kg]$
0	41.2	39.94	2.49
60	40.7	31.01	2.23
120	39.1	11.19	1.74
180	38.3	0.31	1.51
240	39.2	9.24	1.77
300	40.6	29.06	2.26
360	41.2	39.94	2.49

Table 5.3: Results of the FEM model depending on $\Delta\phi$.

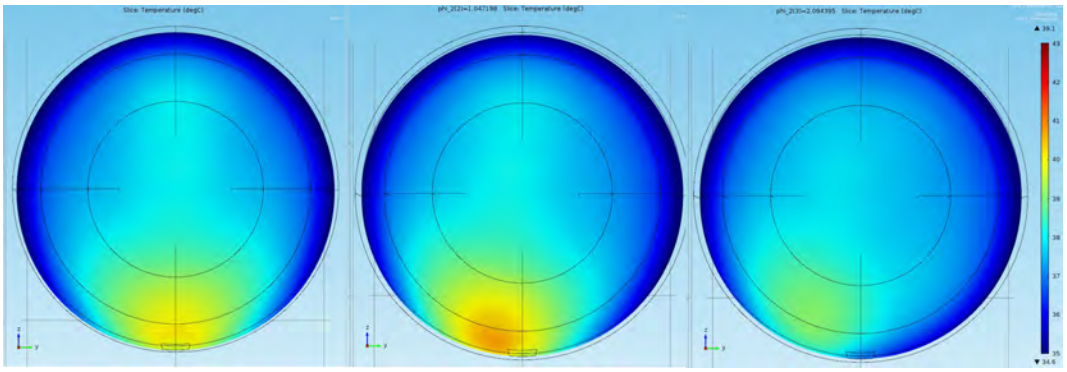

Figure 5.3: Cross-section temperature distributions with $\Delta\phi = 0°$, $\Delta\phi = 60°$, $\Delta\phi = 120°$

5.1.3 Distance between the Patch Antennas

If we change the distance p, we are actually modifying the superposition of the electric and magnetic components of the fields. In this case, because of

the symmetry of the model[3], we know that at the middle-plane Q, in case of $\Delta\phi = 0$ the field components are summed (see previous section). In the first attempt, The ratio p/λ is the electrical dimension of the array. As we have already discussed in chapter 3, the behavior of the array is directly dependent on this parameter, since the width of the main lobe (therefore the ability to increase the directivity) is determined by p/λ. In the far-field region, the smaller the ratio p/λ the larger the main lobe; however there is a reduction of the lateral radiation. In this case we are dealing with a near-field propagation, so the numerical result can be significantly different from the analytical study. The far-field effect of p/λ can be observed in Figure 3.17. If we look at the numerical results obtained and we compare them with the analytical study, there are different behaviors of the systems. The numerical FEM model shows by increasing the distance p we induce a spread of the high-magnitude region of the electric field. Another interesting observation is that the depth of energy deposition is changed. The focus is not still at the skin layer but is deeper internally. This effect can be applied when we want to treat tumors that are superficial, but not necessarily on the skin. It is important to remember that in this way there is less capability of focusing the heating, so an increase of the elements of the array may be necessary. Since we are limited by regulation to operate in the ISM band, and by the physical constraints of the electromagnetic resonance, we can exploit this parameter p/λ to add a degree of freedom to the system. The numerical results are presented in Table 5.4 and the temperature distributions in Figure 5.4.

p $[mm]$	T_{max} $[degC]$	SAR_{tumor} $[W/kg]$	SAR_{total} $[W/kg]$
46.0	41.2	39.94	2.49
54.4	40.6	32.96	2.51
62.7	40.0	27.40	2.32
71.0	39.6	22.60	2.12
79.3	39.0	18.55	1.91
87.7	38.8	15.02	1.72
96.0	38.6	12.01	1.53

Table 5.4: Results of the FEM model depending on p.

[3]Actually the model is not perfectly symmetric from a geometrical standpoint because the feeding position of the probe is shifted along the Y-axis. From an electromagnetic standpoint, the assumption of symmetry is acceptable.

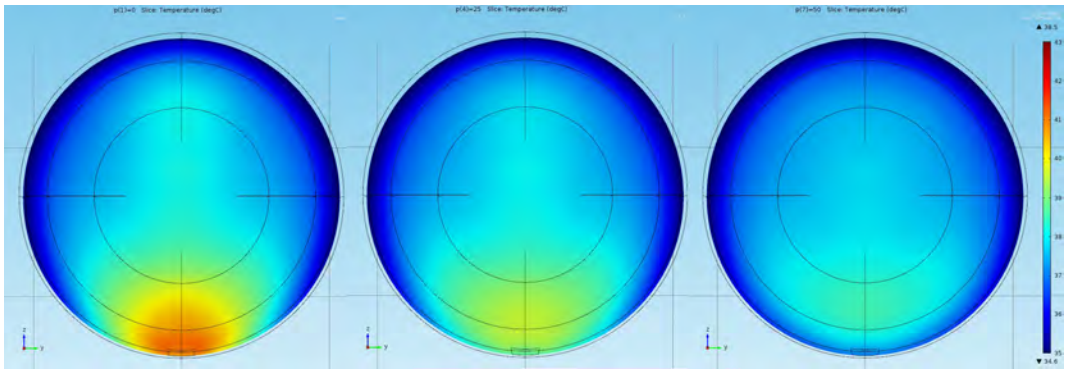

Figure 5.4: Cross-section temperature distributions with p=46 mm, p=71 mm, p=96 mm.

5.1.4 Feeding Power per Antenna

The electromagnetic feeding power P is actually one of the most important characteristics of the device, since the deposition energy rates in the tissues depend on P. The higher the power per antenna, the higher the maximum temperature in organic tissues. When we increase P, it is important to consider the greatest hot-spot[4], and also we must consider the period Δt that is required to obtain the thermal equilibrium. The parameter P cannot be actually assessed alone because we have to consider at the same time the distance patient-array d. In fact, we don't have a unique way to get a certain maximum temperature, but we can evaluate all the combinations (P, d) to achieve T_{max} with a certain distribution pattern of temperature. In the current study, we have performed a parametric analysis to assess the impact of each parameter, but for the clinical implementation, an optimization algorithm is suitable to offer the best configuration (multi-objective evaluation of Pareto front). In future studies, this aspect could be considered in order to prepare the experimental set-up. Let us remember that the human body has to achieve thermal equilibrium during the treatment, so from a thermodynamic standpoint, the amount of power that is flowing inward has to be equal to the amount of power that is flowing toward the environment. Since the variation of temperature is limited to $7 - 8°C$, the required power has to be very small, only a few watts. We should note that the parameter that can be controlled is the global power per antenna P, but the actual source of heating in the tissues is the power density. In fact, with the same feeding P, but with a different distribution of heat sources, we can obtain a higher as

[4]In general the hot-spots are localized at the material interfaces like air-skin, skin-tumor, tumor-fat, fat-muscle.

well as a lower T_{avg} in the tumor or in other specific regions. The numerical results of the FEM model are presented in Table 5.5 and the temperature distributions in Figure 5.5.

P $[W]$	T_{max} $[degC]$	SAR_{tumor} $[W/kg]$	SAR_{total} $[W/kg]$
2	38.9	19.97	1.25
2.7	39.4	26.58	1.66
3.3	40.4	33.26	2.08
4.0	41.2	39.94	2.49
4.7	42.0	46.55	2.91
5.3	42.7	53.23	3.32
6.0	43.4	59.84	3.74

Table 5.5: Results of the FEM model depending on P.

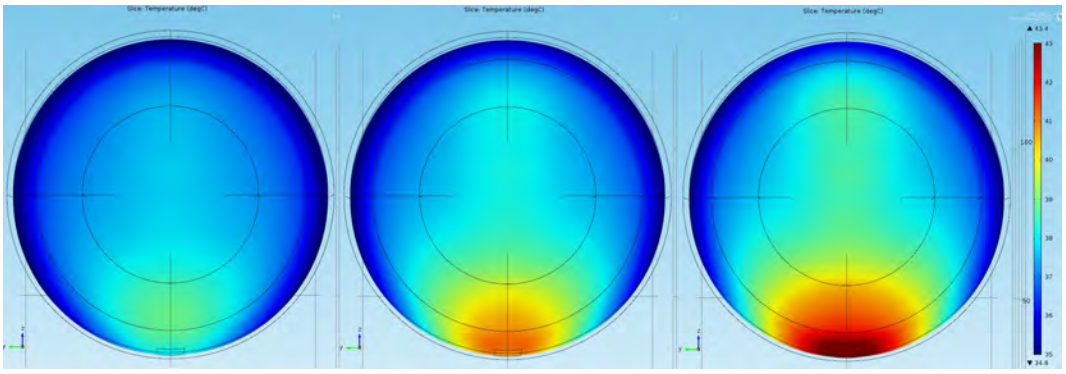

Figure 5.5: Cross-section temperature distributions with P=2 W, P=4 W, P=6 W.

5.2 Definitive Layout

Based upon considferations of the previous sections, we can select an appropriate set of values $d, \Delta\phi, p, P$. Therefore, the definitive values are: $d = 30$mm considering that the bigger d the lower the risk of burns; the optimal phase-shift is $\Delta\phi = 0$ to obtain the direction of the main lobe at 90° with respect to the alignment axis; the distance antenna-antenna $p = 46$mm (barycenters as close as possible); the power per antenna $P = 6$W. The maximum temperature achieved is 43.4°C, and the specific absorbed rate in the tumor is 59.84 W/kg, the total specific absorbed rate is 3.74 W/kg. The most important

physical system properties of clinical interest are the cross-section temperature, the distribution temperature at the skin, the electric field magnitude, and local SAR. We can observe that the heating is effectively confined in the skin and fat layers. The limited increase of internal temperature is due to the heat transmission by thermal conduction. The electric field is actually present in the tumor region and bordering volumes, but also in the bone there are peaks of electric field magnitude (about 350 V/m) due to the phenomenon of electromagnetic standing waves. The definitive temperature distribution, local SAR, and electric field magnitude are shown in Figure 5.6.

5.3 Preliminary Analytical Transient Study

An analytical study of the considered physical model can be helpful to assess the main phenomena involved during the treatment. The model can be analytically evaluated only by making some assumptions that allow us to focus on the specific physical principles that have occurred, more than the overall complexity of the system. Let us consider the Pennes equation for the stationary case:

$$\rho_t c_t \vec{u} \cdot \nabla T = \nabla \cdot (k \nabla T) + Q_{ext} + Q_{bio} \tag{5.4}$$

where $\vec{u}$ is the generic direction considered and

$$Q_{bio} = \rho_b c_b \omega_b (T_b - T) + Q_{met} \tag{5.5}$$

so, we obtain in the mono-dimensional case:

$$\rho_t c_t \frac{\partial T}{\partial x} = k \frac{\partial^2 T}{\partial x^2} + \rho_b c_b \omega_b (T_b - T) + Q_{ext} + Q_{met} \tag{5.6}$$

if we assume that the material is homogeneous we can derive the following relation:

$$Q_{ext} + Q_{met} = \rho_b c_b \omega_b (T - T_b) \tag{5.7}$$

This expression shows that the total internal thermal power, composed of the metabolism and the heat-source from external electric fields, has to be balanced by the exported heat due to the blood perfusion into the capillaries. This is the thermal equilibrium condition[5]. On the other hand, for the

[5]In this model we are not considering the convective heat exchange, so this relation could be changed if a boundary condition is applied. The heat convection is considered in the FEM model.

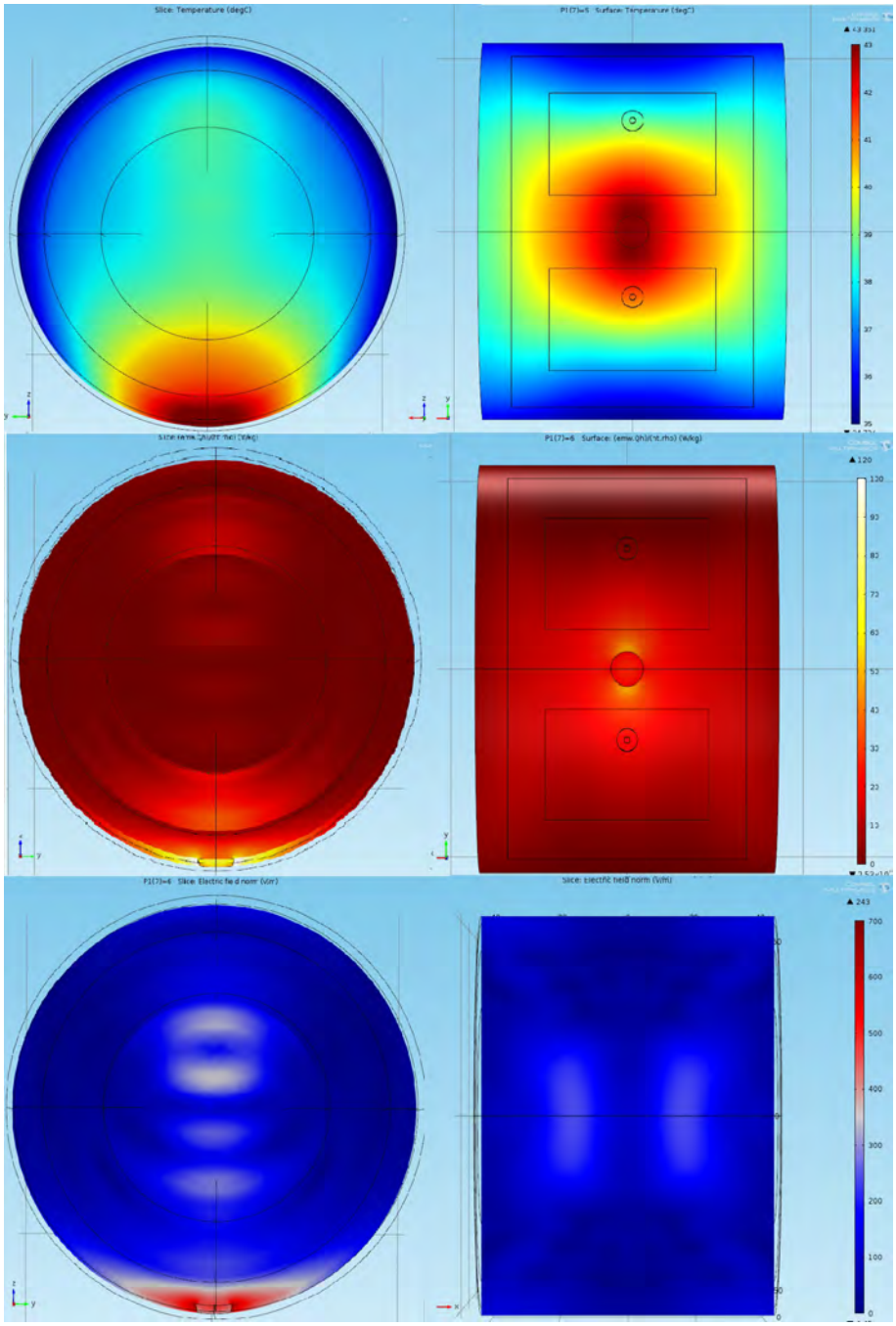

Figure 5.6: Temperature, local SAR and Electric field magnitude with the definitive layout.

transient case, the general form of the Pennes equation is defined as follows:

$$\rho_t c_t \frac{\partial T}{\partial t} + \rho_t c_t \vec{u} \cdot \nabla T = \nabla \cdot (k \nabla T) + Q_{ext} + Q_{bio} \tag{5.8}$$

and as we have done before, let us consider the mono-dimensional case:

$$\rho_t c_t \frac{\partial T}{\partial t} + \rho_t c_t \frac{\partial T}{\partial x} = k \frac{\partial^2 T}{\partial x^2} + \rho_b c_b \omega_b (T_b - T) + Q_{ext} + Q_{met} \tag{5.9}$$

and assuming the homogeneity of the material we can derive the transient thermal power balance :

$$Q_{met} + Q_{ext} = \rho_b c_b \omega_b (T - T_b) + \rho_t c_t \frac{\partial T}{\partial t} \tag{5.10}$$

Observing the equations (5.7) and (5.10) we can note that the difference between them is due to the term $\rho_t c_t \frac{\partial T}{\partial t}$. This term is responsible for the increase of the temperature during the evolution of the system. We can re-write the equation (5.10) as:

$$\rho_t c_t \frac{\partial T}{\partial t} + \rho_b c_b \omega_b T - \rho_b c_b \omega_b T_b = Q_{met} + Q_{ext} \tag{5.11}$$

$$\frac{\partial T}{\partial t} + \frac{\rho_b c_b \omega_b}{\rho_t c_t} T = \frac{\rho_b c_b \omega_b}{\rho_t c_t} T_b + \frac{Q_{met} + Q_{ext}}{\rho_t c_t} \tag{5.12}$$

The last relation is actually a first order differential partial equation (linear with constant coefficients) that can be represented as follows:

$$\frac{\partial y(t)}{\partial t} + a_0(t) y(t) = g(t) \tag{5.13}$$

where

$$\begin{cases} y(t) = T \\ a_0(t) = A_0 = \frac{\rho_b c_b \omega_b}{\rho_t c_t} \\ g(t) = G_0 = \frac{Q_{met} + Q_{ext} + \rho_b c_b \omega_b T_b}{\rho_t c_t} \end{cases} \tag{5.14}$$

so we can obtain the general integration as follows [16]

$$y(t) = e^{-A(t)} \left[C_1 + \int \left(g(t) e^{A(t)} \right) dt \right] \tag{5.15}$$

$$A(t) = \int a_0(t) dt = A_0 t \tag{5.16}$$

therefore, we derive the general solution that can be also expressed in terms of the model quantities,

$$y(t) = e^{-A_0 t}\left[C_1 + \frac{G_0}{A_0}e^{A_0 t}\right] \tag{5.17}$$

$$T(t) = e^{-\frac{\rho_b c_b \omega_b}{\rho_t c_t}t}\left[C_1 + \left(\frac{Q_{met} + Q_{ext} + \rho_b c_b \omega_b T_b}{\rho_b c_b \omega_b}\right)e^{-\frac{\rho_b c_b \omega_b}{\rho_t c_t}t}\right] \tag{5.18}$$

The constant C_1 can be calculated by the imposition of the initial conditions of the system. We can assume that at the beginning state the model is characterized by the temperature $T(0) = 36°C$

$$36 = e^{0}\left[C_1 + \left(\frac{Q_{met} + Q_{ext} + \rho_b c_b \omega_b T_b}{\rho_b c_b \omega_b}\right)e^{0}\right] \tag{5.19}$$

$$C_1 = 36 - \left(\frac{Q_{met} + Q_{ext} + \rho_b c_b \omega_b T_b}{\rho_b c_b \omega_b}\right) \tag{5.20}$$

We can implement in Matlab the evolution of the system described by the equation (5.18) to assess the response to an external power input. We can consider the following physical properties: $\rho_t = 1050kg/m^3$, $c_t = 3639J/(kgK)$, $Q_{met} = 3900W/m^3$, $Q_{ext} = 45000W/m^3$, $\rho_b = 1000kg/m^3$, $c_b = 3770J/(kgK)$, $\omega_b = 0.00189s^{-1}$. We obtain the temperature evolution as depicted in Figure 5.7. We can observe that the required period to obtain the thermal steady state condition is $\Delta t \approx 2000s$. More details about the lengthy period will be given in the next section with the analysis of the FEM results. Let us complete the preliminary study with the behavior of a system that is subjected to two power levels. We analyze the first transient period that is 60 seconds long, and we consider that there is a boosted power applied. Since at the beginning the external power is high, we can assume that $Q_{ext} \gg \rho_b \omega_b c_b (T_b - T) + Q_{met}$. Therefore, we derive the following simplified form of equation (5.12):

$$\frac{\partial T}{\partial t} = \frac{Q_{ext}}{\rho_t c_t} \tag{5.21}$$

and the last equation can be integrated as follows:

$$\int_{T(0)}^{T} dT = \int_{0}^{t_1} \frac{Q_{ext}}{\rho_t c_t} dt \tag{5.22}$$

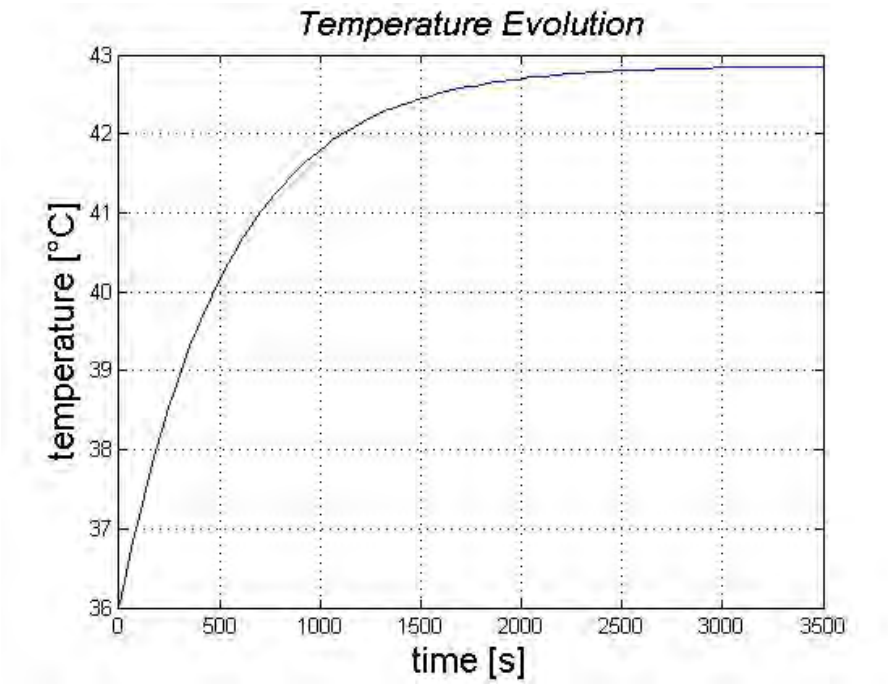

Figure 5.7: Temperature evolution of the system during the entire treatment assuming a steady feeding power.

$$T(t) = T(0) + \frac{Q_{ext}}{\rho_t c_t} t \tag{5.23}$$

The temperature evolves linearly until the hypothesis of high external power holds. Because of this assumption we are neglecting the metabolism as well as the blood perfusion. The equation (5.23) has been implemented in Matlab, and a parametric study has been performed in Figure 5.8. We have considered $Q_{ext1} = 350000 W/m^3$, $Q_{ext2} = 430000 W/m^3$, $Q_{ext3} = 510000 W/m^3$ and $Q_{ext4} = 590000 W/m^3$. Now we can consider the equation (5.15) for the treatment with two power levels. Since we cannot neglect any term, we should consider the following relations:

$$g(t) = G_1 = \frac{Q_{ext1}}{\rho_t c_t} \qquad 0 \leq t \leq t_1 \tag{5.24}$$

$$g(t) = G_2 = \frac{Q_{ext2} + Q_{met} + \rho_b c_b \omega_b T_b}{\rho_t c_t} \qquad t > t_1 \tag{5.25}$$

$$C_1 = 36 - \left(\frac{Q_{ext2} + Q_{met} + \rho_b c_b \omega_b T_b}{\rho_t c_t} \right) \tag{5.26}$$

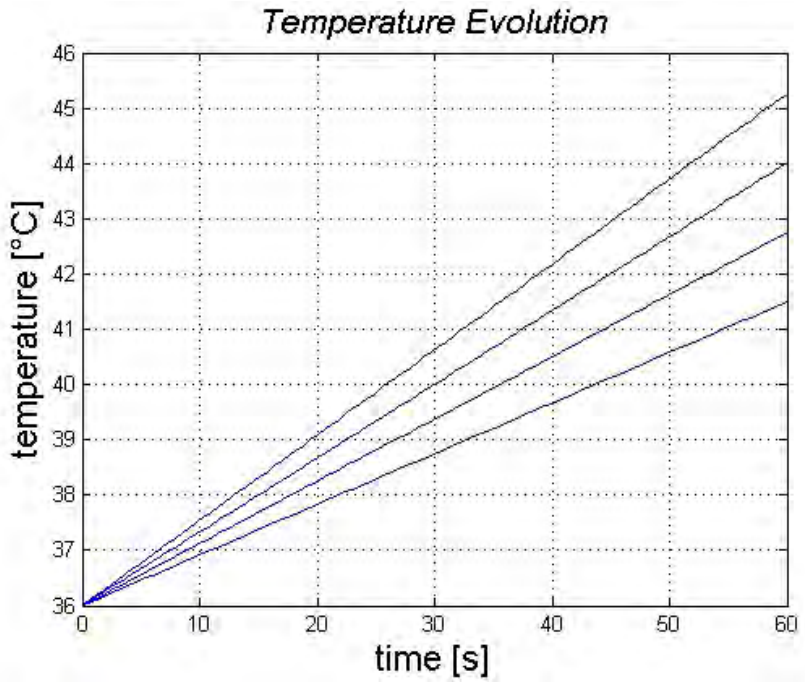

Figure 5.8: Temperature evolution of the system during the first 60 seconds assuming a boosted feeding power.

therefore we obtain a solution for the first period $0 \leq t \leq t_1$ and the remaining time $t > t_1$ as follows:

$$y(t) = e^{-A_0 t}\left[C_1 + \frac{G_1}{A_0}e^{A_0 t}\right] \qquad 0 \leq t \leq t_1 \tag{5.27}$$

$$y(t) = e^{-A_0 t}\left[C_1 + \frac{G_1}{A_0}e^{A_0 t} + \int_{t_1}^{t_2} G_2 e^{A_0 t} dt\right] \quad t > t_1 \tag{5.28}$$

and for the last equation we can compute the integration, and we obtain the relation as follows:

$$y(t) = e^{-A_0 t}\left[C_1 + \frac{G_1}{A_0}e^{A_0 t} + \frac{G_2}{A_0}\left(e^{A_0 t_2} - e^{A_0 t_1}\right)\right] \quad t > t_1 \tag{5.29}$$

Now, we can rewrite the equations (5.27) and (5.29) substituting the physical parameters of the model:

$$T(t) = e^{-\left(\frac{\rho_b c_b \omega_b}{\rho_t c_t} t\right) t}\left[36 + \left(\frac{Q_{met} + Q_{ext1} + \rho_b c_b \omega_b T_b}{\rho_b c_b \omega_b}\right)\left(e^{\left(\frac{\rho_b c_b \omega_b}{\rho_t c_t}\right) t} - 1\right)\right] \tag{5.30}$$

$$0 \leq t \leq t_1$$

$$T(t) = e^{-\left(\frac{\rho_b c_b \omega_b}{\rho_t c_t} t\right) t} \left[36 + \left(\frac{Q_{met} + Q_{ext1} + \rho_b c_b \omega_b T_b}{\rho_b c_b \omega_b} \right) \left(e^{\left(\frac{\rho_b c_b \omega_b}{\rho_t c_t}\right) t} - 1 \right) + \right.$$
$$\left. + \left(\frac{Q_{met} + Q_{ext1} + \rho_b c_b \omega_b T_b}{\rho_b c_b \omega_b} \right) \left(e^{t_1} - e^{t_2} \right) \right]$$
$$t > t_1 \tag{5.31}$$

We can plot the behavior of the system implementing the expressions (5.30) and (5.31). In Figure 5.9 there is also the curve of the evolution at steady power, in order to compare the different Δt that is required to achieve the equilibrium. We have assumed $Q_{ext1} = 800000 W/m^3$, $Q_{ext2} = 45000 W/m^3$, and the periods $t_1 = 60s$, $t_2 = 3500$.

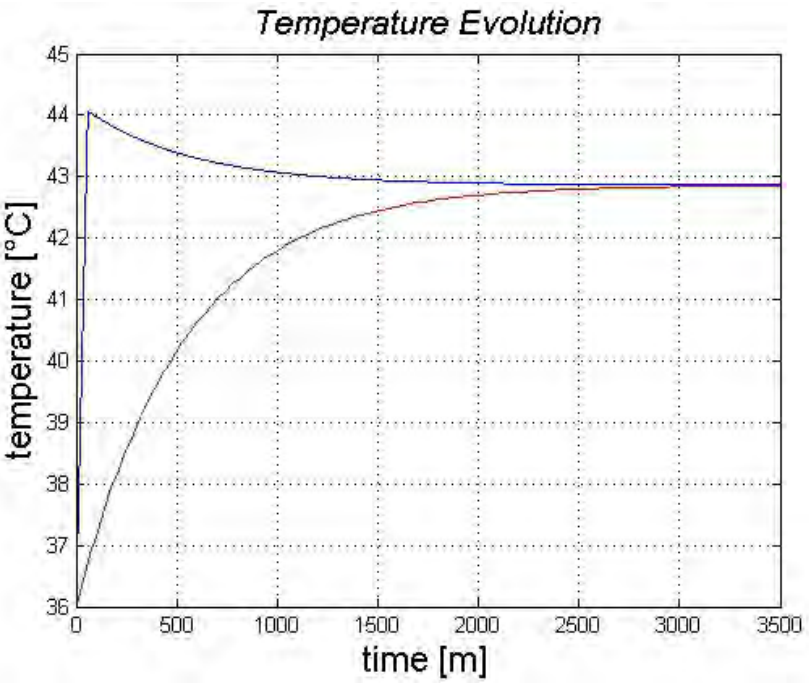

Figure 5.9: Temperature evolution of the system during the entire treatment: comparison of the case with steady feeding power and the case with initial boosted power.

5.4 Numerical FEM results

In this section we will consider the transient temperature during the treatment from a numerical standpoint. Also, we will compare the results with

the curves that we have derived analytically in the last section. Final considerations on the two power level control will be done.

5.4.1 Thermal Evolution with Steady Power

The definitive layout that we derived in section 5.2 has been obtained considering the thermal equilibrium. For the clinical implementation we need to know the required period to achieve the target temperature. So, we consider the FEM model presented in the section 5.2, but in this case applying a time-dependent analysis. Let us remember that the optimal power per antenna in steady state is $P = 6W$, so using this value, we can assess the average temperature of the tumor during the treatment. The beginning temperature distribution of the model is defined by the equilibrium between heat generated from the metabolism and heat exchanged with the environment. The average temperature of the skin at t=0s is $T = 34.5°C$. The defined time-step is $\Delta t_{step} = 60s$. The curve plotted in Figure 5.4.1 is consistent

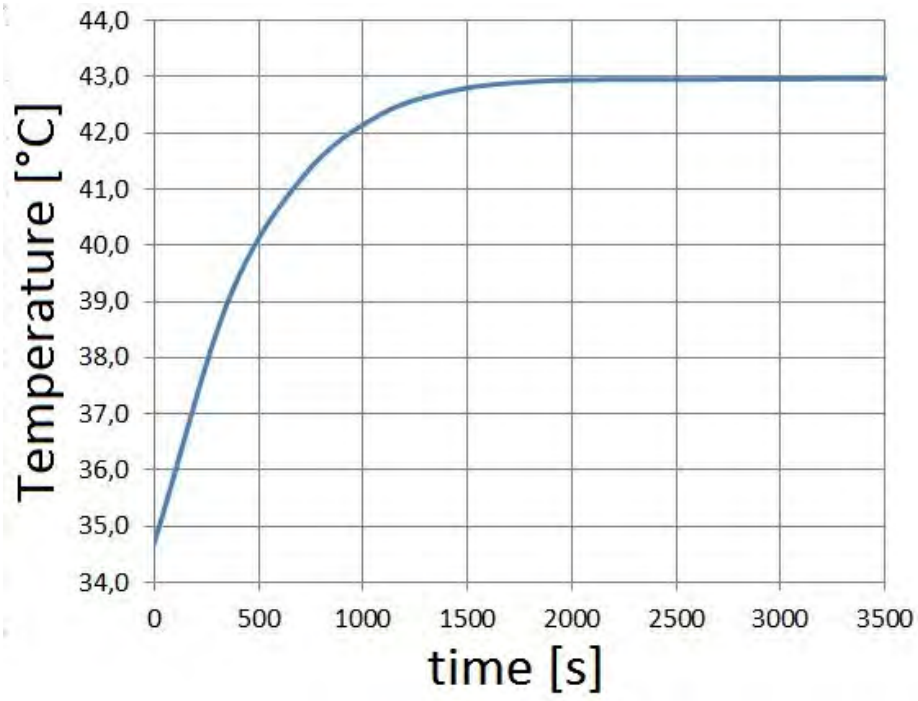

Figure 5.10: Tumor temperature evolution of the system from numerical simulation with steady power.

with curve obtained from the analytical model in the Figure 5.4.1, in spite of the necessary assumptions that we used in the previous study. The transient

period that is necessary to achieve $T = 43°C$ is about $\Delta t = 1600s$. This lengthy period is unacceptable for an effective clinical implementation. It is important to remember that a typical treatment can be performed for a time period of about 20-30 minutes.

5.4.2 Thermal Evolution with Boosted Power

As stated in the previous section, the required Δt to achieve the target temperature is too long. Therefore, we need to apply an initial boosted power in order to reduce Δt. So we have developed a numerical FEM parametric analysis for a period of 60 seconds long, with different initial feeding powers. The parameters considered are $P_1 = 20W$, $P_2 = 30W$, $P_3 = 40W$ and $P_4 = 50W$. The time step that has been used $\Delta t_{step} = 5s$. The results are plotted in the Figure 5.11. We can compare Figure 5.11 with 5.8 and

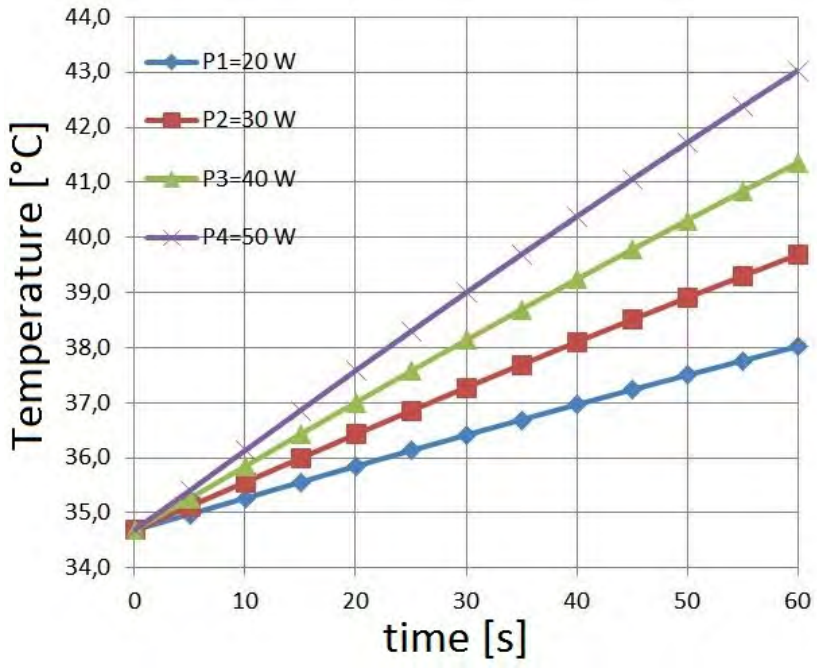

Figure 5.11: Tumor temperature evolution of the system from numerical simulation with different initial boosted powers.

we observe how the results of the analytical study match with the FEM results. Therefore, the effect of the perfusion is negligible with respect to the external power source Q_{ext} during the first period with the boosted power applied. The optimal boosted initial power is $P = 50W$ that allows us to obtain the average temperature in the tumor $T_{tum} = 43.0°C$ at t=60 s. The

maximum temperature in the entire body is $T_{max} = 45.2$ and it is localized in the fat region, and we can accept this value since it is limited by the thermal conduction in the following period of treatment when the boosted power switches to the low level power.

5.4.3 Complete Evolution with two Power Levels

Since we have found that, for period 60 seconds long, the optimal initial boosted power is $P = 40W$ and the optimal low level power is $P = 6W$. We can now assess the thermal behavior of the system during the entire treatment with the two levels power control. The results have been depicted in figure (5.17), and we have reported also the curve of the evolution with the steady state power only for comparison. We can note the match between the

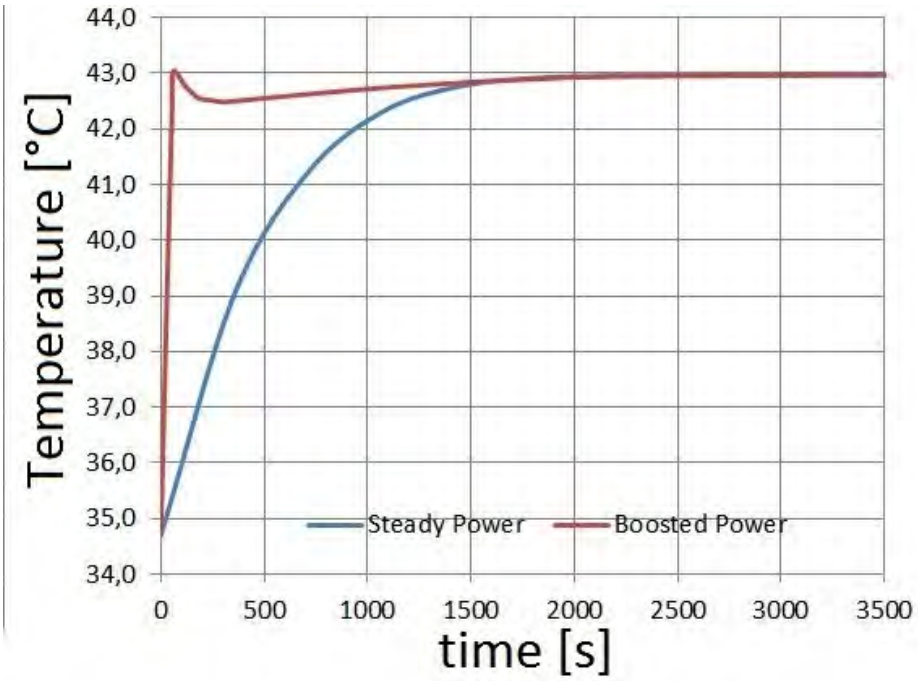

Figure 5.12: Tumor temperature evolution of the system from numerical simulation with steady power and initial boosted power.

analytical study and the numerical results comparing Figure 5.12 with Figure 5.9. The main difference between the curves appears in the period after the first 60 seconds. In fact in the FEM model, the effect of the thermal conduction and therefore the effect of redistribution of the heat between adjacent tissues is included. Also the convective heat exchange towards the environment occurs in the FEM model, and it is notable since the temperature in

the tumor decreases to $T_{tum} = 42.5°C$ after the achievement of the peak, in spite the equilibrium temperature is $T = 43°C$. This effect is not included in the analytical study. When the minimum is achieved, the temperature of the tumor rises slowly to the regime target value. Since the temperature of the tumor is always over $T = 42°C$ (apart from the reduced transient period), the hyperthermia treatment can be actually considered effective. The analysis of temperature distribution is an important aspect that we need to consider, so in Figure 5.13 there is the temperature distribution of the cross-section of the body during the most important moments of the treatment. We should note that the thermal conduction is the predominant phenomenon after the first 60 seconds and that for this reason there is a reduction of the ability to localize the heating. To avoid this effect we could consider in future studies the possibility of heating and refreshing in alternating sequence, in order to exploit the high focusing capability of fast processes.

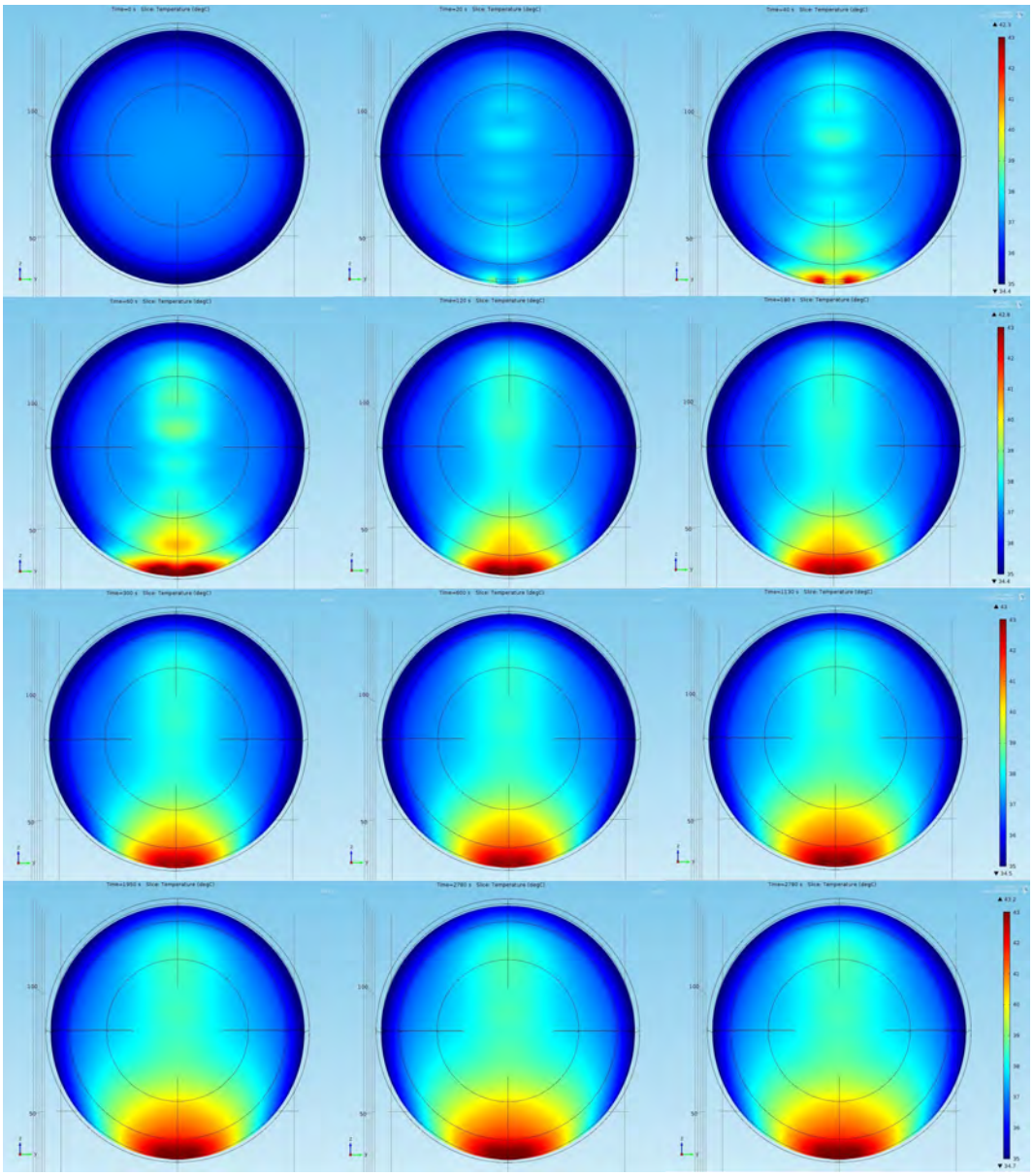

Figure 5.13: Temperature distribution of the system from numerical simulation. From lefto to right, and from top to botton: t=0 s, t=20 s, t=40 s, t=60 s, t=120 s, t=180 s, t=300 s, t=600 s, t=1130 s,t=1950 s, t=2780 s, t=3600 s.

Chapter 6

Conclusion

In this thesis the development of a numerical 3D FEM model of a part of human body, and a patch antenna array operating at the frequency of 2.45 GHz, have been described. Analytical and Finite Difference models have also been studied to compare the different computational approaches in multi-physics problems. The main purpose was the treatment of superficial tumors optimizing the layout of the device at the thermal equilibrium, and the reduction of the transient period required for the target temperature $T = 43°C$. Parametric analyses have been performed using COMSOL 4.3b. First, the single element patch antenna with coaxial feeders was developed. The patch element has been optimized to operate at 2.45 GHz at the point of resonance. Second, the array was defined taking into consideration the best pattern of the electric field and the temperature distribution at the thermal equilibrium, evaluating T_{max} and SAR. Four parametric analyses were performed to derive the optimal distance between the patient and the applicator (d=30 mm), the distance between the barycenters of the elements (p=46 mm), the phase-shift ($\Delta\phi = 0°$) and the power per antenna ($P = 6W$). The average tumor temperature obtained was $42.9°C$ (thermal equilibrium), while the maximum temperature during the entire treatment was $45.2°C$. The $SAR_{tumor} = 59.84W/kg$ and $SAR_{total} = 3.74W/kg$, so their ratio was equal to 16. The temperature evolution was assessed, and a boosted initial power ($P = 50W$) was found to be effective in order to reduce the transient period. Also, we observed that the temperature distribution at the time t=60 s was more focused than the temperature distribution at the equilibrium. This observation induced us to consider for future studies, an alternated pulsed power and pulsed refreshment, in order to achieve the optimum heat-focus. In this study we have verified that for superficial tumors, 2 patch antenna elements at 2.45 GHz are sufficient to treat shallow tumors. The muscle layer presented limited high temperatures, and the bone was not heated in spite

of the presence of standing electromagnetic waves and low perfusion rates. For clinical application, it is necessary to use a power controller with two levels connected to a thermometric sensor that operates as feedback during the transient phase. For deeper tumors, a different operating frequency and a spatial configuration of the array are required. The transient analysis in the current study shows that a good possibility for improving the temperature pattern can be obtained applying an pulsed power for a period smaller than 60s. This conclusion can be deduced by the fact that thermal conduction between tissues occurs more slowly than the deposition of energy from the external device. As we stated previously, this result was applied to reduce the transient evolution, but can actually be appropriately applied to improve the focus.

Appendix A

Matlab Scripts

A.1 Analytical 1D Thermal Steady State Model

```
%PARAMETRI FISICI DEL MODELLO
h=5;
k1=0.5;
k2=0.3;
R1=0.027;
R2=0.030;
T_tum=43;
T_a=37;
q_m1=3000;
q_m2=3000;
omega1=0.002;
omega2=0.005;
rho_b=1000;
c_b=3639;
T_inf=20;
m1=sqrt((omega1*rho_b*c_b)/(k1));
m2=sqrt((omega2*rho_b*c_b)/(k2));

j=1;
for h=5:5:100

%VETTORE DEI TERMINI NOTI
v(1)=T_tum-T_a-(q_m1/(omega1*rho_b*c_b));
v(2)=(q_m2/(omega2*rho_b*c_b))-(q_m1/(omega1*rho_b*c_b));
v(3)=0;
v(4)=h*(T_inf-T_a)-((h*q_m2)/(omega2*rho_b*c_b));


%MATRICE RISOLVENTE
```

```
m_11=1;
m_12=1;
m_13=0;
m_14=0;

m_21=exp(m1*R1);
m_22=exp(-m1*R1);
m_23=-exp(m2*R1);
m_24=-exp(-m2*R1);

m_31=m1*exp(m1*R1);
m_32=-m1*exp(-m1*R1);
m_33=-m2*exp(m2*R1);
m_34=m2*exp(-m2*R1);

m_41=0;
m_42=0;
m_43=(exp(m2*R2)*(h+m2*k2));
m_44=(exp(-m2*R2)*(h-k2*m2));

M=[m_11 m_12 m_13 m_14;...
   m_21 m_22 m_23 m_24;...
   m_31 m_32 m_33 m_34;...
   m_41 m_42 m_43 m_44];

ABCD=(M^-1)*v';
A=ABCD(1);
B=ABCD(2);
C=ABCD(3);
D=ABCD(4);

domain1=linspace(0,R1,101);
domain2=linspace(R1,R2,101);

theta1=A*exp(m1*domain1)+B*exp(-m1*domain1);
theta2=C*exp(m2*domain2)+D*exp(-m2*domain2);
T1(j,:)=theta1+(T_a+(q_m1/(omega1*rho_b*c_b)));
T2(j,:)=theta2+(T_a+(q_m2/(omega2*rho_b*c_b)));

colori=jet(numel(T1(:,1)));
figure(1);
plot(domain1,T1(j,:),'Color',colori(j,:))
title('INFLUENZA DI h')
grid on
hold on
plot(domain2,T2(j,:),'Color',colori(j,:))

j=j+1;
end
```

```
j=1;
for T_inf=25:-1:0

%VETTORE DEI TERMINI NOTI
v(1)=T_tum-T_a-(q_m1/(omega1*rho_b*c_b));
v(2)=(q_m2/(omega2*rho_b*c_b))-(q_m1/(omega1*rho_b*c_b));
v(3)=0;
v(4)=h*(T_inf-T_a)-((h*q_m2)/(omega2*rho_b*c_b));


%MATRICE RISOLVENTE
m_11=1;
m_12=1;
m_13=0;
m_14=0;

m_21=exp(m1*R1);
m_22=exp(-m1*R1);
m_23=-exp(m2*R1);
m_24=-exp(-m2*R1);

m_31=m1*exp(m1*R1);
m_32=-m1*exp(-m1*R1);
m_33=-m2*exp(m2*R1);
m_34=m2*exp(-m2*R1);

m_41=0;
m_42=0;
m_43=(exp(m2*R2)*(h+m2*k2));
m_44=(exp(-m2*R2)*(h-k2*m2));

M=[m_11 m_12 m_13 m_14;...
   m_21 m_22 m_23 m_24;...
   m_31 m_32 m_33 m_34;...
   m_41 m_42 m_43 m_44];

ABCD=(M^-1)*v';
A=ABCD(1);
B=ABCD(2);
C=ABCD(3);
D=ABCD(4);

domain1=linspace(0,R1,101);
domain2=linspace(R1,R2,101);

theta1=A*exp(m1*domain1)+B*exp(-m1*domain1);
theta2=C*exp(m2*domain2)+D*exp(-m2*domain2);
```

```
T1(j,:)=theta1+(T_a+(q_m1/(omega1*rho_b*c_b)));
T2(j,:)=theta2+(T_a+(q_m2/(omega2*rho_b*c_b)));

colori=jet(numel(T1(:,1)));
figure(2);
plot(domain1,T1(j,:),'Color',colori(j,:))
title('INFLUENZA DI T_inf')
grid on
hold on
plot(domain2,T2(j,:),'Color',colori(j,:))

j=j+1;
end

T_inf=25;

j=1;
for omega1=0.005:0.001:0.040

m1=sqrt((omega1*rho_b*c_b)/(k1));
m2=sqrt((omega2*rho_b*c_b)/(k2));

%VETTORE DEI TERMINI NOTI
v(1)=T_tum-T_a-(q_m1/(omega1*rho_b*c_b));
v(2)=(q_m2/(omega2*rho_b*c_b))-(q_m1/(omega1*rho_b*c_b));
v(3)=0;
v(4)=h*(T_inf-T_a)-((h*q_m2)/(omega2*rho_b*c_b));


%MATRICE RISOLVENTE
m_11=1;
m_12=1;
m_13=0;
m_14=0;

m_21=exp(m1*R1);
m_22=exp(-m1*R1);
m_23=-exp(m2*R1);
m_24=-exp(-m2*R1);

m_31=m1*exp(m1*R1);
m_32=-m1*exp(-m1*R1);
m_33=-m2*exp(m2*R1);
m_34=m2*exp(-m2*R1);

m_41=0;
m_42=0;
m_43=(exp(m2*R2)*(h+m2*k2));
m_44=(exp(-m2*R2)*(h-k2*m2));
```

```
M=[m_11 m_12 m_13 m_14;...
   m_21 m_22 m_23 m_24;...
   m_31 m_32 m_33 m_34;...
   m_41 m_42 m_43 m_44];

ABCD=(M^-1)*v';
A=ABCD(1);
B=ABCD(2);
C=ABCD(3);
D=ABCD(4);

domain1=linspace(0,R1,101);
domain2=linspace(R1,R2,101);

theta1=A*exp(m1*domain1)+B*exp(-m1*domain1);
theta2=C*exp(m2*domain2)+D*exp(-m2*domain2);
T1(j,:)=theta1+(T_a+(q_m1/(omega1*rho_b*c_b)));
T2(j,:)=theta2+(T_a+(q_m2/(omega2*rho_b*c_b)));

colori=jet(numel(T1(:,1)));
figure(3);
plot(domain1,T1(j,:),'Color',colori(j,:))
title('INFLUENZA DI omega1')
grid on
hold on
plot(domain2,T2(j,:),'Color',colori(j,:))

j=j+1;

end

omega1=0.0005;
j=1;
for omega2=0.005:0.002:0.040

m1=sqrt((omega1*rho_b*c_b)/(k1));
m2=sqrt((omega2*rho_b*c_b)/(k2));

%VETTORE DEI TERMINI NOTI
v(1)=T_tum-T_a-(q_m1/(omega1*rho_b*c_b));
v(2)=(q_m2/(omega2*rho_b*c_b))-(q_m1/(omega1*rho_b*c_b));
v(3)=0;
v(4)=h*(T_inf-T_a)-((h*q_m2)/(omega2*rho_b*c_b));


%MATRICE RISOLVENTE
m_11=1;
m_12=1;
```

```
m_13=0;
m_14=0;

m_21=exp(m1*R1);
m_22=exp(-m1*R1);
m_23=-exp(m2*R1);
m_24=-exp(-m2*R1);

m_31=m1*exp(m1*R1);
m_32=-m1*exp(-m1*R1);
m_33=-m2*exp(m2*R1);
m_34=m2*exp(-m2*R1);

m_41=0;
m_42=0;
m_43=(exp(m2*R2)*(h+m2*k2));
m_44=(exp(-m2*R2)*(h-k2*m2));

M=[m_11 m_12 m_13 m_14;...
   m_21 m_22 m_23 m_24;...
   m_31 m_32 m_33 m_34;...
   m_41 m_42 m_43 m_44];

ABCD=(M^-1)*v';
A=ABCD(1);
B=ABCD(2);
C=ABCD(3);
D=ABCD(4);

domain1=linspace(0,R1,101);
domain2=linspace(R1,R2,101);

theta1=A*exp(m1*domain1)+B*exp(-m1*domain1);
theta2=C*exp(m2*domain2)+D*exp(-m2*domain2);
T1(j,:)=theta1+(T_a+(q_m1/(omega1*rho_b*c_b)));
T2(j,:)=theta2+(T_a+(q_m2/(omega2*rho_b*c_b)));

colori=HSV(numel(T1(:,1)));
figure(4);
plot(domain1,T1(j,:),'Color',colori(j,:))
title('INFLUENZA DI omega2')
grid on
hold on
plot(domain2,T2(j,:),'Color',colori(j,:))

j=j+1;

end
```

A.2 Antenna Patch Design

```
%PARAMETRI PREDEFINITI
eps_r=4.7
h=0.16; %cm


i=1;
for f_r=2.4:0.01:2.5 %RANGE DI FREQUENZA GHz

    fr(i)=f_r    ;
    W(i)=(30/(2*f_r))*(2/(eps_r+1))^(1/2);
    eps_reff(i)=((eps_r+1)/2)+((eps_r-1)/2)*(1+12*(h/W(i)))^(-1/2);
    delta_L(i)=(h*0.412)*((eps_reff(i)+0.3)*((W(i)/h)+0.264))/...
    ((eps_reff(i)-0.258)*(W(i)/h+0.8));
    L(i)=30/(2*f_r*(eps_reff(i))^(1/2))-2*(delta_L(i));
    L_e(i)=L(i)+2*delta_L(i);
    Y_f(i)=W(i)/2;   %riferito ad un asse parallelo a W

i=i+1;
end

%MATRICE DEI RISULTATI
M=[fr; W; L]' % N.B: le distanze sono calcolate in centimetri

%GRAFICI
figure(1)%LARGHEZZA ALTEZZA
plot(fr,W,'k')
axis([2.4 2.5 2.6 3.8])

grid on
hold on
plot(fr,L,'r')

figure(2)%COSTANTE DIELETTRICA EFFETTIVA
plot(fr,eps_reff)
grid on
axis([2.4 2.5 4.34 4.355])
```

A.3 Electromagnetic Array Radiation Pattern

```
%PARAMETRI
c=3*10^8;
f=2.45*10^9;
lambda=c/f;
csi_max=90*(pi/180);
delta_csi_max=30*(pi/180);
N=2;
%W=0.28;
L=0.0282; %[m]
h=0.0016;  %[m]

grafici=4;

l_limite=lambda/(abs(cos(csi_max))+1);

i=1;
for l=(L+12*h):(l_limite-(L+12*h))/(grafici-1):l_limite

    ll(i)=l;
    D=sqrt(2)*N*l;
    R_frahunoffer(i)=(2*D^2)/lambda;
    R_fresnel(i)=0.62*sqrt(D^3/lambda);
    delta(i)=(2*pi*l/lambda)*cos(csi_max);
    delta_csi(i)=acos(((delta(i)/2)-(pi/N))*(lambda/(pi*l)))...
                -acos(((delta(i)/2)+(pi/N))*(lambda/(pi*l)));

    s=1;
    for NN=2:15

        lobe_ampl(i,s)=abs(acos(((delta(i)/2)-(pi/NN))*(lambda/(pi*l)))...
                      -acos(((delta(i)/2)+(pi/NN))*(lambda/(pi*l))));

    s=s+1;
    end

    t=1;
    for csi=0:2*pi/360:2*pi

        v(t)=(pi*l/lambda)*cos(csi)-delta(i)/2;
        F(i,t)=abs(sin(N*v(t))/sin(v(t)));

    t=t+1;
    end

i=i+1;
```

```
end

for m=1:numel(F(:,1))

     domain=linspace(0,2*pi,numel(F(1,:)));
     figure(m)
     polar(domain,F(m,:))
     figure(50+m)
     plot(linspace(0,360,numel(F(1,:))),F(m,:),'b')
     axis([0 360 0 N])
     grid on

end

for m=1:numel(lobe_ampl(:,1))

    domain2=linspace(2,s,numel(lobe_ampl(1,:)));
    figure(m+numel(F(1,:)))
    plot(domain2,(180/pi)*lobe_ampl(m,:),'--s','LineWidth',2,...
                'MarkerEdgeColor','k',...
                'MarkerFaceColor','b',...
                'MarkerSize',10)

    hold on
    plot(domain2,(180/pi)*delta_csi_max*ones(1,numel(lobe_ampl(m,:))),'r')
    grid on

end

for k=1:numel(F(:,1))

    [f,t] = meshgrid(linspace(0,2*pi,60),linspace(0,pi,60));
    raggio=(sin(N*((pi*ll(k)/lambda)*cos(t)-delta(k)/2))...
          ./sin((pi*ll(k)/lambda)*cos(t)-delta(k)/2));
    z = raggio.*sin(t).*cos(f);
    y = raggio.*sin(t).*sin(f);
    x = raggio.*cos(t);
    figure(numel(F(:,1))+k)
    surf(x,y,z)

end

l_limite_mm=l_limite*1000
R_frahunoffer_mm=R_frahunoffer*1000
R_fresnel_mm=R_fresnel*1000
delta_deg=delta*(180/pi)
delta_csi=delta_csi*(180/pi)
```

A.4 Finite Difference Thermal Model

```
%PROPRIETA' DEI MATERIALI
H_t=[0.003 0.013 0.033 0.080]; %cm
K_t=[0.50 0.25 0.50 0.40];
RHO_t=[1050 920 1041 1500];
C_t=[3639 2500 3500 1300];
% OMEGA_t=[1.8 3.864 2.7066 0.75]/1000;
omega_bone=0.75/100000;

rho_b=400;
c_b=3770;
T_a=36;
T_inf=20;
h=10;

time=3600;
t_intervals=time/2;
t=linspace(0,time,t_intervals);
dt=time/(t_intervals+1);


tt=[60 time];%intervalli temporali di diverse potenze
pp=[7 0.6];%picchi di potenza
survey=[10 60 400 800 1200 1600 time-1];%tempo di campionamento

%IMPOSIZIONE DELLE CONDIZIONI INIZIALI E FORZANTI (A TRATTI)

step=0.001;
x(1)=0;
index=1;
ref=1;

while max(x)<=max(H_t)

    if x(index)<=H_t(ref)

        k_t(index)=K_t(ref);
        rho_t(index)=RHO_t(ref);
        c_t(index)=C_t(ref);


    else
        disc(ref)=index-1;
        ref=ref+1;
        k_t(index)=K_t(ref);
        rho_t(index)=RHO_t(ref);
```

```
            c_t(index)=C_t(ref);


        end

    x(index+1)=x(index)+step;
    index=index+1;
    end

    Tmax=150;
    TT=linspace(1,Tmax,Tmax);
    omega_t=omega_bone*ones(numel(x),Tmax);

    for index=1:disc(1)


        omega_t(index,1:36)=0.8/1000;
        omega_t(index,37:42)=(0.8-((TT(37:42)-37).^4.8)/5400)/1000;
        omega_t(index,42:Tmax)=0.38/1000;

    end

    for index=disc(1)+1:disc(2)

        omega_t(index,:)=(0.36+0.36*exp(-((TT-45).^2)/12))/1000;

    end

    for index=disc(2)+1:disc(3)

        omega_t(index,:)=(0.5+3.5*exp(-((TT-45).^2)/12))/1000;

    end

    %DENSITA' DI POTENZA TERMICA

    ref=1;
    for i=1:numel(t)

        if i*dt<tt(ref)

            q_m(1:disc(1),i)=pp(ref)*(linspace(100000,90000,...
            numel(x(1:disc(1)))));
            q_m(disc(1)+1:disc(2),i)=pp(ref)*(linspace(45000,...
            10000,numel(x(disc(1)+1:disc(2)))));
            q_m(disc(2)+1:disc(3),i)=pp(ref)*(linspace(35000,...
            20000,numel(x(disc(2)+1:disc(3)))));
            q_m(disc(3)+1:numel(x),i)=pp(ref)*(linspace(3000,...
            4000,numel(x(disc(3)+1:numel(x)))));
```

```
    else

        if ref==numel(pp)

            break

        end

        ref=ref+1;
        q_m(1:disc(3),i)=(pp(ref)/2)*(cos(x(1:disc(3))...
        *pi/(H_t(3)))+1);
        q_m(disc(3)+1:numel(x),i)=0;

    end

end

k_t(numel(x))=K_t(numel(K_t));
rho_t(numel(x))=RHO_t(numel(K_t));
c_t(numel(x))=C_t(numel(K_t));

%CONDIZIONI DI DIRICHLET SUL BORDO DESTRO DEL DOMINIO
for n=1:numel(t)

    T(numel(x),n)=36;

end

%CONDIZIONI INIZIALI
for i=1:numel(x)-1

    T(i,1)=36;

end

%CALCOLO DEI VALORI DI TEMPERATURA NELL'INTERO DOMINIO
for n=2:numel(t)

    for i=numel(x)-1:-1:1

        if i~=1
             Pin=k_t(i)/(rho_t(i)*c_t(i));
             Rin=-(omega_t(i,round(T(i,n-1)))*rho_b*c_b)...
             /(rho_t(i)*c_t(i));
             SSin=(1/(rho_t(i)*c_t(i)))*(q_m(i,n)+...
             omega_t(i,round(T(i,n-1)))*rho_b*c_b*T_a);

             T(i,n)=T(i,n-1)+(Pin*dt/step^2)*(T(i+1,n-1)...
```

```
                -2*T(i,n-1)+T(i-1,n-1))+...
                       Rin*dt*T(i,n-1)+...
                       SSin*dt;

          else

                T(1,n)=(h*T_inf+(k_t(1)/step)*T(2,n))/...
                (h+k_t(1)/step);


          end

      end

  end

  for n=1:numel(t)

      Tavg_tum(n)=sum(T(1:disc(1),n))...
      /numel(T(1:disc(1),n));
      Tavg_fat(n)=sum(T(disc(1)+1:disc(2),n))...
      /numel(T(disc(1)+1:disc(2),n));
      Tavg_muscle(n)=sum(T(disc(2)+1:disc(3),n))...
      /numel(T(disc(2)+1:disc(3),n));
      Tavg_bone(n)=sum(T(disc(3)+1:numel(x),n))...
      /numel(T(disc(3)+1:numel(x),n));

  end

  figure(1)
  plot(x,q_m)
  grid on
  title('\it{Power Density Distribution}','FontSize',16)
  xlabel('space [m]','FontSize',16)
  ylabel('Power [W/m^3]','FontSize',16)

   figure(2)
   plot(t,Tavg_tum,'b')
   grid on
   hold on
   plot(t,Tavg_fat,'r')
   hold on
   plot(t,Tavg_muscle,'g')
   hold on
   plot(t,Tavg_bone,'k')
   title('\it{Average Temperatures}','FontSize',16)
   xlabel('time [s]','FontSize',16)
   ylabel('temperature [Â°C]','FontSize',16)
```

```
colori=HSV(numel(survey));
for i=1:numel(survey)
figure(3)
plot(x,T(:,round(survey(i)/dt)),'Color',colori(i,:))
colormap(jet)
grid on
xlabel('space [m]','FontSize',16)
ylabel('temperature [Â°C]','FontSize',16)
title('\it{Temperature Evolution}','FontSize',16)
hold on
end

figure(4)
mesh(t,x,T)
shading interp
colormap(jet)
xlabel('time [s]','FontSize',16)
ylabel('space [m]','FontSize',16)
zlabel('temperature [Â°C]','FontSize',16)
title('\it{Temperature Evolution}','FontSize',16)
```

A.5 Analytical Transient Thermal Model

```
%PARAMETRI FISICI
rho_b=1000;
c_b=3770;
omega_b=0.0018*1.05;
T_b=36;
rho_t=1050;
c_t=3639;
Q_met=3900;
Q_ext=45000;


%CALCOLO DEI COEFFICIENTI NUMERICI
A_0=(rho_b*c_b*omega_b)/(rho_t*c_t);
G_0=(Q_met+Q_ext+rho_b*c_b*omega_b*T_b)/(rho_t*c_t);
C1=36-(Q_met+Q_ext+rho_b*c_b*omega_b*T_b)/(rho_b*c_b*omega_b);
t=linspace(0,3500);
T=exp(-A_0*t).*(C1+(G_0/A_0).*exp(A_0*t));

figure(1)
plot(t,T)
grid on
xlabel('time [s]','FontSize',16)
```

```
ylabel('temperature [Â°C]','FontSize',16)
title('\it{Temperature Evolution}','FontSize',16)

%end


for Q_ext=350000:80000:600000

tt=linspace(0,60);
TT=36+Q_ext/(rho_t*c_t)*tt;

figure(2)
plot(tt,TT)
grid on
hold on
xlabel('time [s]','FontSize',16)
ylabel('temperature [Â°C]','FontSize',16)
title('\it{Temperature Evolution}','FontSize',16)

end

Q_ext1=800000;
Q_ext2=45000;
t1=60;
t2=3500;



tt1=linspace(0,t1,t1+1);
tt2=linspace(t1,t2,t2+1);
G_1=(Q_ext1)/(rho_t*c_t);
G_2=(Q_met+Q_ext2+rho_b*c_b*omega_b*T_b)/(rho_t*c_t);
C1=36-G_1/A_0;
TTT1=exp(-A_0*tt1).*(C1+(G_1/A_0)*(exp(A_0*tt1)));
TTT2=exp(-A_0*tt2).*(C1+(G_1/A_0)*(exp(A_0*t1))+(G_2/A_0)*...
(exp(A_0.*tt2)-exp(A_0*t1)))
T_tot=TTT1;
T_tot(numel(TTT1)+1:numel(TTT1)+numel(TTT2))=TTT2;
figure(3)
plot(linspace(0,t2,numel(T_tot)),T_tot)
grid on
xlabel('time [m]','FontSize',16)
ylabel('temperature [Â°C]','FontSize',16)
title('\it{Temperature Evolution}','FontSize',16)
hold on
plot(t,T,'r')
```

Bibliography

[1] David M. Pozar, Microwave Engineering 4th edition, John Wiley & Sons, 2011.

[2] Constantine Balanis, Antenna Theory 3rd edition, John Wiley & Sons, 2005.

[3] D Poljak, Advanced modeling in Computational Electromagnetic Compatibility, John Wiley & Sons, 2007.

[4] P. Di Barba, A. Savini, S.Wiak, Field Models in Electricity and Magnetism, Springer, 2008.

[5] Kumarads, Sherar, Edge-element based finite element analysis of microwave hyperthermia treatments for superficial tumours on the chest wall, International Journal of Hyperthermia, n. 19 Vol 4, 2002.

[6] K. Cheng, V. Stakhursky, O. Craciunescu, P. Stauffer, M. Dewhirst and S. K Das , Fast Temperature Optimization of Multi-Source Hyperthermia Applicators with reduced-order modelinh of virtual sources, Phys. Med. Biol. 53 1609-1635, 2008.

[7] F. Dughiero, V. D'Ambrosio, Numerical model for RF capacitive regional deep Hyperthermia in Pelvic Tumors, Med. Bio. Eng. Comput., Vol 45 issue 5, Springer, 2007.

[8] Esra Neufeld, High Resolution Hyperthermia Treatment Planning, PhD Thesis, ETH Zuerich, 2008.

[9] Alessio Cucini, Antenna design laboratory: Microstrip Antennas, Department of Information Engineering, University of Siena, 2006.

[10] A.B. Mutiara, R. Refianti, Rachmansyah, Design of Microstrip Antenna for Wireless Communication at 2.4 GHz, Journal of Theoretical and Applied Information Technology, Vol. 33 No.2, 2011.

[11] H.H. Pennes, Analysis of Tissue and Arterial Blood Temperatures in the resting Human Forearm, Journal of Applied Physiology, 1948

[12] A.C. Metaxas, R.J. Meredith, Industrial Microwave Heating. Cambridge: Institution of Engineering and Technology, 1983.

[13] T. Politi, Equazioni alle Derivate Parziali, Politecnico di Bari, 2006.

[14] M. Midrio, Campi Elettromagnetici, S.G.E., 2003.

[15] A.J. Fenn, C.J. Diederich, P.R Stauffer, An Adaptive-Focusing Algorithm for a Microwave Planar Phased Array Hyperthermia System, Lincoln Laboratory Journal 6(2):269-288, 1993.

[16] E. Giusti, Analisi Matematica, Bollati Boringhieri, 2003.